

Aykut Argönül

PH.D. THESIS

**Measurement and Calculation of
Multicomponent-Diffusion and
Reaction in Catalyst Particles,
Effect of the Catalyst Pore Structure**



Cuvillier Verlag Göttingen
Internationaler wissenschaftlicher Fachverlag

Measurement and Calculation of Multicomponent-Diffusion and Reaction in Catalyst Particles, Effect of the Catalyst Pore Structure

Vom Promotionsausschuss der
Technischen Universität Hamburg-Harburg (TUHH)
zur Erlangung des akademischen Grades
Doktor-Ingenieur (Dr.-Ing.)
genehmigte Dissertation

von

Aykut Argönül

aus

Ankara/Türkei

2009

1. Gutachter: Prof. Dr. Dr. h.c. Frerich J. Keil

2. Gutachter: Prof. Dr.-Ing. Rudolf Eggers

Vorsitzender: Prof. Dr.-Ing. Irina Smirnova

Tag der mündlichen Prüfung: 02.12.2009

Measurement and Calculation
of
Multicomponent-Diffusion and
Reaction in Catalyst Particles,
Effect of the Catalyst
Pore Structure

Bibliografische Information der Deutschen Nationalbibliothek

Die Deutsche Nationalbibliothek verzeichnet diese Publikation in der Deutschen Nationalbibliografie; detaillierte bibliografische Daten sind im Internet über <http://dnb.d-nb.de> abrufbar.

1. Aufl. - Göttingen: Cuvillier, 2009

Zugl.: (TU) Hamburg-Harburg, Univ., Diss., 2009

978-3-86955-215-6

© CUVILLIER VERLAG, Göttingen 2009

Nonnenstieg 8, 37075 Göttingen

Telefon: 0551-54724-0

Telefax: 0551-54724-21

www.cuvillier.de

Alle Rechte vorbehalten. Ohne ausdrückliche Genehmigung des Verlages ist es nicht gestattet, das Buch oder Teile daraus auf fotomechanischem Weg (Fotokopie, Mikrokopie) zu vervielfältigen.

1. Auflage, 2009

Gedruckt auf säurefreiem Papier

978-3-86955-215-6

Acknowledgements

First of all, I would like to thank to Prof. Frerich J. Keil, who has given me the opportunity to pursue this PhD work in his institute and absolute freedom during that period. I would like to thank him also for being positive all the time. It is in his institute where I have become mature as a scientist and as an individual. That is why the place of Prof. Keil and his institute in my life is very special.

Sincere thanks goes to Dr. Achim Bartch for educating me about working in the laboratory and for his advices in general. All the basics and tricks of laboratory work, I have learned from him. If I became a good experimenter, it is with his support. I also appreciate his attitude and help towards improving my German by speaking in German with me.

Christina Laarman, who was responsible for laboratories and technical assistance in our institute, also gets many many thanks from me. She has supported the experimental work by letting me borrow spare parts and small laboratory equipment from her laboratory and from the storehouse. Also, thanks to her that she remembered (reminded) everybody's birthday and acted like a catalyst for the breakfasts and celebrations we had at the department. Without her, we scientists would not have been able to become social animals.

Also from the institute, our computer administrator Klaus Mandel receives special thanks for his support about computers, cluster and software, and our secretary Hermine Oppelaar for her kindness and help in answering questions about filling out official forms and documents.

My appreciation for Cesar Lazo, Matthias Kolkowski and Andreas Heyden has to be also put to record. Sven Jakobtorweihen should receive extra appreciation for his friendship during the years we had shared the same room at the university. Additionally, he has also helped/motivated me to write this thesis in \LaTeX , so he deserves an extra "Thank You!". Also similar thanks goes to Nils Zimmermann, who has chosen to share the same room with me at the institute, for his endless friendship...

I would like to thank to all the students who have made their project work, bachelor thesis or master thesis under my supervision: Gergana Bannenkina, Bonaventure Okoro, Vanya Omaynikova, Manuel De La Torre Diaz, Sreekanth Chilamkurthi, Velichka Tsonova, Milica Lukic, Kerem Ali Günbulut, Nevena Gerginova Marinova, Cvetanka Bojkova and Zarko Jovanov.

Special thanks to colleagues and friends; Erkan Yıldız, Feray Sever, Harun Kulaç, Rıza Demir, Serhat Güneyli, Mehmet Çekiç, Gökhan Gani, Mehmet Eser Atay, Björn Pfankuchen, Ali Emre Çakır, Andreas Joos, Arda Özkaynak, Dicle Yıldız, Gamze Artuğ, İrfan Sonal, Taner Çakıcı and Tarık Çamurdeş. Also special thanks to colleagues and friends who have chosen similar paths (pursuing a PhD): Mert Şahin, Denis Chaykin, Erkan Aksoy, Hidayet Argun, Çiğdem Çakıcı, Burçak Özkök, Alp Ergünel, Ali Emre Çubukçu, E. Fırat Yağar, F. Altan Yıldırım and Cumhuriyet Cantürk.

Very special thanks to other precious friends and people, whose names I might have forgotten to write, but who have put up with me during this journey (and even now)...

Dear Nevin, my dearest thanks goes also to you for supporting and putting up with me even at times I was really hard to put up with. Thank you again for everything.

Last but not least, my beloved family; dear mother, dear father and the sweetest person in the world, dear sister; without your love and support, this world would not have been worth struggling. Thank you for being always there for me and loving me...

Looking back now, to the time I have spent and all of these people, it would have been no pleasure (if possible at all) for me to pursue such a work without you. For joining me in this journey (even for the smallest period of time), I would like to stress my gratitude loudly one more time :

Teşekkürler / Thank you / Danke schön

Aykut Argönül

Teşekkür

Öncelikle enstitüsünde böyle bir konu üzerinde doktora çalışması yapmama izin veren, ve bütün bu süre boyunca da tam anlamıyla özgür olarak çalışmama imkan sağlayan Prof. Keil'a teşekkürü bir borç bilirim. Ayrıca her zaman, her konuda pozitif olduğu için de kendisine teşekkür etmek istiyorum. Hem bilim adamı, hem de bir birey olarak olgunluğa bu enstitüdeki çalışmalarım sırasında ulaştım. Bu yüzden Prof. Keil'ın ve enstitüsünün hayatımda önemli bir yeri oldu.

Beni laboratuvar çalışması konusunda eğiten Dr. Achim Bartch'a da en içten teşekkürlerimi iletmeyi bir borç bilirim. Laboratuvarda çalışmak konusunda bütün temel bilgileri ve püf noktalarını ondan öğrendim. Başarılı bir deneyci olduysam, bu onun sayesinde. Ayrıca enstitüde benimle Almanca konuşarak Almancayı daha hızlı öğrenmeme de çok yardımcı olduğu için kendisine bir kere daha teşekkür ederim.

Enstitümüzün laboratuvar ve teknik konularından sorumlu olan Christina Laarman'a da teşekkürlerimi sunmak isterim. Laboratuvarından ve/veya depodan gerek çeşitli ekipmanları, gerekse yedek parçaları gerektiğinde ödünç vererek, deneysel çalışmaların sekteye uğramadan devam etmesi için desteğini esirgemedi. Ayrıca, bölümdeki herkesin doğum günlerini hatırlayıp (hatırlatıp), bir katalizör gibi davrandı; enstitüde yapılan kahvaltı ve kutlamaları organize etti. Eğer o olmasaydı, biz bilim adamları sosyal hayvanlar olamazdık.

Ayrıca enstitünün bilişim sorumlusu olan Kalus Mandel'e bilgisayarlar, yazılımlar ve bilgisayar kümesi ile alakalı desteklerinden dolayı ve sekreterimiz Hermine Oppelaar'a da resmi formların ve dökümanların doldurulması ve hazırlanması konusundaki yardımlarından dolayı teşekkür ederim.

Cesar Lazo, Matthias Kolkowski ve Andreas Heyden'e olan teşekkürlerimi de burada kayda geçirmek istiyorum. Sven Jakobtorweihen'a ise, aynı ofisi paylaştığımız yıllar boyunca, gösterdiği arkadaşlıktan dolayı teşekkür etmek istiyorum. Bunun yanında kendisi bu tezi L^AT_EX ile yazmam konusunda destek ve öncü olduğu için de kendisine bir kez daha içten "teşekkürlerimi" sunuyorum. Benzer bir teşekkürü de Nils Zimmerman'a borçluyum. Kendisi

de aynı büroda çalıştığımız süre boyunca o eşsiz arkadaşlığını esirgememiştir...

Gözetimim altında dönem çalışması, lisans tezi veya yüksek lisans tezi yapan bütün öğrencilerime de: Gergana Banenkina, Bonaventure Okoro, Vanya Omaynikova, Manuel De La Torre Diaz, Sreekanth Chilamkurthi, Velichka Tsonova, Milica Lukic, Kerem Ali Günbulut, Nevena Gerginova Marinova, Cvetanka Bojkova ve Zarko Jovanov, teşekkür etmek isterim.

Arkadaşlar: Erkan Yıldız, Feray Sever, Harun Kulaç, Rıza Demir, Serhat Güneyli, Mehmet Çekiç, Gökhan Gani, Mehmet Eser Atay, Björn Pfankuchen, Ali Emre Çakır, Andreas Joos, Arda Özkaynak, Dicle Yıldız, Gamze Artuğ, İrfan Sonal, Taner Çakıcı, Tarık Çamurdeş, ve benzer yoldan devam eden (doktora yapan): Mert Şahin, Denis Chaykin, Erkan Aksoy, Hidayet Argun, Çiğdem Çakıcı, Burçak Özkök, Alp Ergünel, Ali Emre Çubukçu, E. Fırat Yağar, F. Altan Yıldırım ve Cumhuriyet Cantürk sizleri unutucağımı düşünmediniz değil mi, sizlere de destekleriniz için çok teşekkürler.

Yukarıda adını yazmayı unutmuş olabileceğim, ve tabii ki bu doktora sırasında (ve hatta şu anda bile) bana hoşgörü gösteren ve destek veren diğer arkadaşlarıma da en içten teşekkürlerimi sunuyorum.

Sevgili Nevin, en zor ve dayanılmaz olduğum zamanlarımda bile gösterdiğin hoşgörü ve verdiğin destek için sana olan minnettarlığımı burada dile getirmek istiyorum. Her şey için çok teşekkürler.

Sevgili ve değerli ailem; annem, babam ve dünyanın en tatlı ve en temiz insanı, bir tanecik kardeşim, Pelincim; sizin sevginiz, bana olan güveniniz ve desteğiniz olmasaydı, hayat uğruna uğraşmaya değmezdi. Her zaman yanımda olduğunuz ve beni karşılıksız sevdiğiniz için çok teşekkürler...

Şimdi geriye dönüp bütün bu insanlarla geçen bu zamana bakınca görüyorum ki; sizlersiz böyle bir çalışma çok zevksiz hatta belki de imkansız olurdu. Bana bu yolculuk boyunca, kısacık bir süreliğine bile olsa, eşlik ettiğiniz için minnettarlığımı bir kere daha dile getirmek istiyorum:

Teşekkürler / Thank you / Danke schön

Aykut Argönül

In the preparation of this printed work and the scientific work in it open-source-software were used. This document has been prepared using L^AT_EX. Most of the work for this thesis was carried out on Linux systems (SuSe and Pardus). And Open Office was used for office applications.

Contents

List of Figures	ix
List of Tables	xiii
I Background Information	1
1 Introduction	3
1.1 Utilization of Catalysts and Their Importance	3
1.2 Motivation	4
1.3 Outline	4
II Basics	7
2 Theoretical Aspects	9
2.1 Catalyst Pellets	10
2.2 Characterization of Porous Media	10
2.3 Transport Processes in Porous Media	11
2.4 Ethylene Hydrogenation	17
2.5 Experimental Reactors	18
2.5.1 Kinetic Measurement Reactors	19
2.5.2 Single-Pellet Reactor	21

III	Core of Work	23
3	Work Done	25
3.1	Experimental Work	26
3.1.1	Re-design and Improvement of Single-Pellet Reactor . .	26
3.1.2	Re-design of Turbo-Reactor	28
3.1.3	Building-Up Experimental Set-up	31
3.1.4	Pore Structure Analysis	33
3.1.5	Experimental Results from Reactors	35
3.2	Modeling	48
3.2.1	Modeling of Many Pores	50
3.2.2	Comparison of Two Geometrical Models	52
3.2.3	Notes on Surface Diffusion	56
3.2.4	Review of Knudsen Diffusion	62
3.2.5	Surface Diffusion as a Function of Surface Coverage . .	104
3.2.6	Results for Other Pore Lengths and Pressures	108
3.2.7	More General Case: Multi-Component Diffusion and Reaction in a Pore	114
IV	Epilogue	123
4	Summary	125
5	Future Aspects	131
V	Supplementary Part	135
A	Appendix	137
A.1	Calculation procedure for \check{F}	137
A.2	Calculation procedure for \check{G}	140

A.3	Pores with closed-end and symmetric pressures modeled with projection approach	143
A.3.1	Pores with closed-end	143
A.3.2	Pores with symmetric pressures	144
A.4	Experimental Procedure	146
A.4.1	Single-pellet reactor	146
A.4.2	Turbo-reactor	148
A.4.3	Gas chromatography sample analysis	150
A.5	List of Suppliers	151
A.6	Mercury-Porosimetry plots for relevant catalyst pellets	152
A.7	Kinetic experiments data	155
	Nomenclature	161
	Index	165
	Bibliography	167

List of Figures

2.1	Sketch of various transport processes taking place in heterogeneous catalysis.	11
2.2	A simple representation of Horiuti-Polanyi mechanism.	18
2.3	Common types of reactors used in catalytic research.	19
2.4	Simple scheme of a single-pellet reactor with sample concentration profile inside.	21
3.1	Drawings and pictures of the single pellet reactors.	27
3.2	Drawings and pictures of the turbo reactors.	29
3.3	Flow-chart of the experimental set-up.	32
3.4	Plot of temperature vs reaction rate for experimental series SP1.	37
3.5	Plot of temperature vs reaction rate for experimental series SP2.	40
3.6	Ethylene content in the center chamber for SP2.	42
3.7	Ethane content in the center chamber for SP2.	42
3.8	Fitting of <i>model 4</i> to experimental data (<i>TR2</i>) with 95% confidence interval.	47
3.9	SEM (Scanning Electron Microscopy) images of a catalyst surface at different magnifications.	50
3.10	A 3-D pore network built and the belonging pore connectivity for it.	51
3.11	Hexagonal unit cell and graphical representations of the parallel pore models using it.	52

3.12	Differential control volumes in the pore and various mass flows related.	57
3.13	Schematic drawing of surface flow and gas phase flow with adsorption and desorption rates in a single pore having outer-surfaces at both ends.	59
3.14	Polar diagrams showing beaming effect at the entrance and exit of a cylindrical pore at various pore lengths.	66
3.15	Series conductance of two pores.	67
3.16	Traditional representation of cosine-law	69
3.17	A sketch of the Knudsen's experimental set-up used to check the validity of the cosine-law.	70
3.18	Alternative representation of the cosine-law.	71
3.19	Projection of pore cross-section onto a sphere.	72
3.20	The distribution of flow from a slice to the other slices and to the two ends of the pore.	73
3.21	The distribution of the flow from the (left) pore entrance between slices and pore exit.	73
3.22	The log-scale plot of the functions \check{F} and \check{G} against the normalized distance.	74
3.23	The flow diagram of the computer program for sole Knudsen case.	79
3.24	Effect of slice thickness on calculated transmission probability.	81
3.25	The relative impingement rate distribution inside a pore for various length to radius ratios.	84
3.26	An overview of the pore and the outer-surfaces with the transport processes involved.	85
3.27	The pictorial representation of the mass balance for a control volume at the surface of the pore.	86
3.28	A plain representation of the surface flow in the porous substance that is divided into n slices.	88

3.29	The flow diagram of the computer program for simultaneous surface and Knudsen flow case.	95
3.30	Comparison of impingement and scattering rates for the three models used for the case $P_{left} = 30kPa$	98
3.31	The adsorption desorption rate difference for <i>model III</i> for the case $P_{left} = 30kPa$	99
3.32	Surface coverage profiles for all the three models for the case $P_{left} = 30kPa$	100
3.33	Comparison of flow rates for all the three models for the case $P_{left} = 30kPa$	101
3.34	Various plots representing the behaviour of the case $P_{left} = 150kPa$	102
3.35	Back-calculated surface diffusion coefficient values.	103
3.36	Various plots for the surface coverage dependent diffusion coefficient system, with $P_{left} = 30kPa$	105
3.37	Back-calculated surface diffusion coefficient values along with the estimation errors for the non-constant surface diffusion coefficient case.	107
3.38	Various plots for the case $L/r_{pore} = 80$ with a constant surface diffusion coefficient.	111
3.39	Reaction rate profile inside the pore for the case Knudsen diffusion and multi-component surface diffusion accompanied with surface reaction.	118
3.40	H_2 surface coverage profile for the case Knudsen diffusion and multi-component surface diffusion accompanied with surface reaction.	119
3.41	C_2H_4 gas and total flow rate profile for the case Knudsen diffusion and multi-component surface diffusion accompanied with surface reaction.	120

3.42	ADRD profiles for C_2H_4 , C_2H_6 and H_2 from <i>model 1</i> for the case Knudsen diffusion and multi-component surface diffusion accompanied with surface reaction.	121
A.1	Auxiliary figures for the calculation of the projection area in \check{F} calculation.	138
A.2	Auxiliary figures for the calculation of the projection area in \check{G} calculation.	140
A.3	Pore size distribution plot of Y41573, based on mercury-porosimetry analysis.	152
A.4	Pore size distribution plot of Y41574, based on mercury-porosimetry analysis.	152
A.5	Pore size distribution plot of Y41575, based on mercury-porosimetry analysis.	153
A.6	Pore size distribution plot of Y42099, based on mercury-porosimetry analysis.	153
A.7	Pore size distribution plot of Y42100, based on mercury-porosimetry analysis.	154
A.8	Pore size distribution plot of Y42218, based on mercury-porosimetry analysis.	154

List of Tables

3.1	Characteristic values for the catalyst pellets used.	34
3.2	The experimental results for series SP1, the Single Pellet reactor series 1.	36
3.3	The experimental results for series SP2, the Single Pellet reactor series 2.	39
3.4	Various kinetic models fitted to the data from the turbo-reactor.	45
3.5	Model 4 fitted parameter values to <i>TR1</i> experiments.	46
3.6	Model 6 fitted parameter values to <i>TR1</i> experiments.	46
3.7	Model 4 fitted parameter values to <i>TR2</i> experiments.	48
3.8	Pore size distribution data for catalyst Y34315.	53
3.9	Parameter values for the kinetic expression in eq. 3.4	54
3.10	Mole percentages at the center of the pellet collected from different sources.	55
3.11	Comparison between transmission probability values calculated with different approaches.	65
3.12	The effect of slice thickness on the transmission probability for a pore of length of ten times the pore radius with sub-slice thickness of $2 \cdot 10^{-3} \cdot r_{pore}$	80
3.13	Comparison between calculated transmission probabilities, w , (for $\delta\bar{z} = 2 \cdot 10^{-3}$) with various approaches from literature. . .	82
3.14	Comparison between calculated transmission probabilities with the literature for very short pores.	82

3.15	Comparison of pore entrance impingement rate at the pore entrance between various methods	83
3.16	Physical constants for the sample system propylene (C_3H_6) in (Vycor-) glass.	94
3.17	Some other important parameters calculated and/or used for the sample system propylene (C_3H_6) in (Vycor-) glass.	96
3.18	Total flow rate and flow enhancement with respect to sole Knudsen flow case for various pressures ($L/r_{pore} = 20$).	97
3.19	Total flow rate and flow enhancement with respect to sole Knudsen flow for a coverage dependent surface diffusion coefficient ($D^{Surf} = \frac{D_0^{Surf}}{1-\theta}$) case for $L/r_{pore} = 20$	106
3.20	Total flow rate and flow enhancement with respect to sole Knudsen flow case for $L/r_{pore} = 50$ and $= 80$ (with $D^{Surf} = const.$).	109
3.21	Total flow rate and flow enhancement with respect to sole Knudsen flow case for $L/r_{pore} = 50$ and 80 (with $D^{Surf} = \frac{D_0^{Surf}}{1-\theta}$).	110
3.22	Total flow rate and flow enhancement with respect to sole Knudsen flow case for $L/r_{pore} = 20, 50, 80$ for $\Delta P = P_{left} - P_{right} = 10$ [kPa], with a constant D^{Surf}	112
3.23	Constants and parameters used for the simulation of the case multi-component diffusion and reaction.	115
A.1	List of suppliers for the gases and equipment used.	151
A.2	Data from kinetic experiments, <i>TR1</i>	156
A.3	Data from kinetic experiments, <i>TR2</i>	157

Part I

Background Information

“Aşağılarda inciler yoksa derinliklere dalmak anlamsız olurdu...”

“It would be foolish to dive into the depths, if there were no pearls down there...”

1

Introduction

1.1 Utilization of Catalysts and Their Importance

How important is catalysis? Catalysis is the backbone of the chemical industry and a fundamental feature of all life processes.¹ Without it our modern technological society would not have happened; four of the largest sectors of the world economy, i.e. the petroleum, power, chemicals, and food industries, which account more than 10 trillion dollars of gross world product, are largely dependent on catalytic processes.²

In the 19th and early 20th centuries most industrial reactions were run at high temperatures and pressures in order to achieve reasonable rates of production. This is called the *sledgehammer approach*. Unfortunately, these severe conditions are energy intensive, corrosive or otherwise damaging to equipment and materials, and non-selective. However, the development of

improved methods of contacting and the *feather approach*, i.e., the extensive use of catalysts, have enabled mankind to operate at lower pressures and temperatures with much higher efficiencies.²

The catalytic technologies are also important for providing a sustainable development; catalysis can help protecting the ozone layer, combating the greenhouse effects, creating environmentally safer transport, prevention of pollution, minimization of consumption of raw materials, increasing energy efficiency, processing renewable raw materials into valuable chemicals, etc.¹

It is these capabilities of the catalysts that make them an interesting subject for the industrial and academic bodies.

1.2 Motivation

Noticing the importance of catalysts for today's world and the future, brings out the necessity to fully grasp the phenomena accompanying their utilization. On the other hand, in spite of extensive efforts given, these phenomena are still only poorly understood. For example, models are known to yield inaccurate results when compared to the experimental data obtained by practical work³.

The motivation behind this study was thus to take another step in improving our understanding of catalysis. For that purpose, both experimental and theoretical work is to be conducted, the ultimate goal being the optimization and thus more effective utilization of these costly materials.

1.3 Outline

After this introductory part of the thesis, the basics of the general theory of catalysis and various processes occurring therein are given in *section 2*. Notes about the probe reaction and laboratory reactors can also be found in that section. The core of this work is the *section 3 Work Done*, and most emphasis is given to it. It starts on topics concerning the experimental work; such as the design and construction of the laboratory reactors, and the experimental set-up. Next, the results from the pore structure analysis

experiments of the pellets, the results from the single-pellet reactor and the turbo-reactor are presented and discussed. Later on, the focus is taken to the modeling. At first, a previous model and simple modeling are compared. Based on the conclusions achieved from that comparison, deeper reviews of surface and Knudsen diffusion are made, and some commonly used assumptions are critically analyzed. Then a novel way of modeling a pore under Knudsen and surface diffusion, and its solution way are introduced. Validity of this new approach is shown by reproducing results from the literature for the sole Knudsen diffusion case. For simultaneous surface and Knudsen diffusion, simulations for various pore lengths and pressures are done and the results are discussed. Additionally, back-calculation of the surface diffusion coefficient using commonly used assumptions is made and the found results are compared with the actually used values. A system with concentration dependent surface diffusion coefficient and a pore under simultaneous Knudsen and surface diffusion accompanied by surface reaction is also simulated for sample cases. The *sections 4* and *5* give the summary of the whole thesis and the probable future aspects of the work, respectively. Finally, as a supplement, some additional theoretical and experimental details are given in appendix.

Part II

Basics

“Sadece baharatlar ile yemek yapılamaz...”

“One cannot cook using only spices...”

2

Theoretical Aspects

This chapter gives general information about the fundamental subjects that form the theoretical basis of this work. Information about catalyst pellets, characterization of these pellets, different transport processes occurring in them and their basic modeling, a short review about the probe reaction (hydrogenation of ethylene), and information about laboratory reactors can all be found in this chapter. The information presented here is thought to serve as an introduction into the basics of these important topics.

2.1 Catalyst Pellets

The field, where a solid material catalyzes a reaction of molecules in gas or liquid phase, is called *heterogeneous catalysis*. The catalyzed reaction occurs on the surface of the solid and thus a large surface area is desirable. Since commonly these solid materials are non-porous, to make better use of these precious materials (e.g., platinum, palladium, silver, etc.) by achieving larger surface areas, they can be dispersed on other porous materials, on the so called *support*. The conditions in each step of catalyst manufacture have decisive influence on the final catalyst properties and thus should be precisely defined and carefully controlled⁴. Most industrial catalysts are made either by precipitation, when active phase and support are made together, or by the impregnation of an active phase on to a preformed support⁵. Then for the sake of easier handling, they are cast into *pellets* which can be in various shapes, such as; spheres, tablets, rings, etc. In the preparation, the catalyst can be distributed on the support depending on the conditions during the manufacturing process in different ways⁶: homogeneous, egg-shell, egg-yolk or egg-white. For different reaction conditions and objectives, e.g., selectivity, different distributions can be better choices over the others⁷. More detailed information about heterogeneous catalysis and pellet manufacture can be easily found in various text books and prints, such as: Wijngaarden *et al.*³, Hagen⁶, Chorkendorff and Niemantsverdriet⁸, White⁹, Farrauto and Bartholomew¹⁰, Stiles and Koch¹¹, Masel¹², Thomas and Thomas¹³.

2.2 Characterization of Porous Media

The characterization of catalysts is important in the manufacture of catalysts and for the optimization of industrial catalytic processes. The primary purpose of this characterization is to provide a basis for understanding the interrelationship between activity and selectivity of a catalyst, and its physical and chemical properties.¹⁴

The surface topography, metal particle size, mechanical strength, pore

volume, total surface area, pore size distribution, etc. are all properties that can be determined via various experimental techniques. Among these only a few are standardized. These include the determination of the total surface area by the Brunauer-Emmett-Teller (BET) method and also the determination of the pore-size distribution by nitrogen-sorption and mercury porosimetry¹⁴. Basically the mercury-porosimetry method is based on forcing mercury into the pores at different pressures and measuring the volume of mercury penetrating. On the other hand, nitrogen-sorption makes use of the pressure dependence of capillary condensation on the pore diameter. The amount of nitrogen sorption is measured and then used to extract information about the pore-size distribution and surface area of the sample. These methods, which are also used in this work for the characterization of catalyst pellets, are well-known and more information about the underlying principles can be found in various publications, see e.g., Lowell¹⁵, Do¹⁶, Rouquerol *et al.*¹⁷, Rouquerol and Sing¹⁸, Haber *et al.*¹⁹.

2.3 Transport Processes in Porous Media

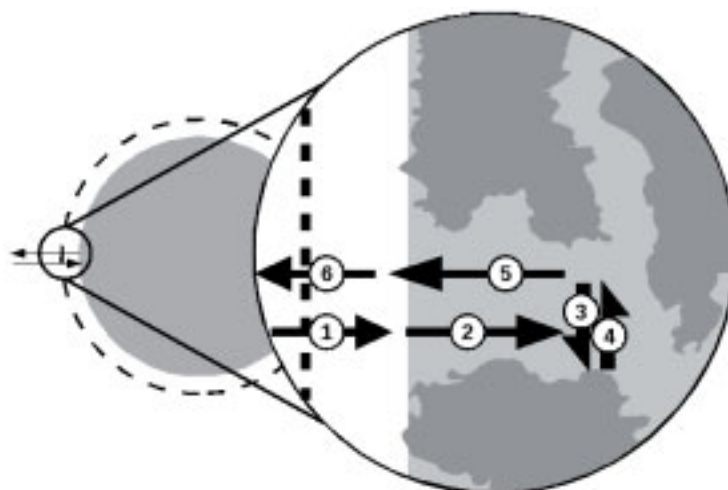


Figure 2.1: Sketch of various transport processes taking place in heterogeneous catalysis. 1) transport of reactants through the boundary layer, 2) diffusion of reactants inside the pores, 3) adsorption, 4) desorption, 5) diffusion of products inside the pores, 6) transport of reactants through the boundary layer back into the bulk.

In heterogeneous catalysis, besides the reaction, a sequence of transport processes takes place that starts with the reactants at the bulk phase and ends with the delivery of the products back to it. A simple representation of this sequence can be seen in fig.2.1. Initially, the reactants have to overcome the boundary layer resistance surrounding the catalyst particle and reach the external surface. After that they have to be transported inside the pores until they reach the site where the precious catalyst is located. The reactants then should be adsorbed on the surface, which is an essential step. Only after such an adsorption, one can talk about heterogeneous catalysis. After the completion of reaction taking place on the surface, the products start their journey back into the bulk. They are first desorbed into the pore space, they travel inside the pores and finally, they trespass the boundary layer and reach the bulk phase. Consequently, appropriate modeling of these processes is important due to correct identification of the rate-determining/slowest step, and challenging due to the variety and complexity of the processes involved.

Very briefly, one can define these various transport processes as follows:

Viscous Flow

Viscous, or convective, flow is the case where one takes the gas as a continuum and the driving force as the pressure difference. Inside pores there are different ways to characterize the viscous flow. For a gas normally the compressibility effects should be considered too. However, for a system with a very low pressure variation and constant temperature, it is possible to neglect the compressibility effects and use a model of incompressible gas. In such a case, Hagen-Poiseuille equation (eq.2.1) is the commonly used equation representing the incompressible laminar flow inside a tube.

$$J^v = -c \frac{r_p^2}{8\eta} \frac{dP}{dz} \quad (2.1)$$

where η is the dynamic viscosity.

The use of this formula for very small conduits, such as fine catalyst pores, is known to be not so accurate, nevertheless, it is still used very commonly

in modeling similar type of systems for the sake of simplicity²⁰.

Diffusion

Diffusion is the process where the molecules move due to concentration differences. Single molecules travel in one direction until they finally collide with other molecules and change direction. If this process takes place in the bulk where the molecules are virtually only in contact with other gas molecules, it is called ordinary or molecular diffusion; if it takes place in a small pore where the molecules get mostly in contact with the wall molecules, it is called Knudsen diffusion; if molecule-molecule and molecule-wall interactions are both comparable, it is called to be in transition region; if the molecules are adsorbed and are moving on the surface, it is called surface diffusion. There are various models that can be used to describe different types of diffusion. Some frequently used models are the Fick's Law, the Maxwell-Stefan model and the dusty-gas model.

Fick's Law

Fick's first law is probably the most well-known model for diffusion. For a constant total concentration system it has the following form:

$$J = -D \cdot C \cdot \frac{dx_i}{dz} \quad (2.2)$$

where D is the diffusion coefficient, C is the total concentration, x_i is the mole fraction of the species i and z indicates the coordinate.

Fick's law in its simple form does not take into account the interaction between different species and thus care should be taken when applying it to multi-component systems, that is, systems having more than two components. A generalized form of Fick's law has to be taken for that case.

$$J_i = -c_{tot} \cdot \sum_{k=1}^{n-1} D_{i,k} \nabla x_k \quad (2.3)$$

The diffusion coefficient for Fick's Law, e.g., for Knudsen diffusion case, can be estimated with the following formula:

$$D_i^{Kn} = \frac{2}{3} \cdot r_p \cdot \sqrt{\frac{8RT}{\pi M_{wi}}} \quad (2.4)$$

or for the ordinary diffusion case, for example, with the Chapman-Enskog formula:

$$D_{ij} = 1.8583 \cdot 10^{-3} \cdot \frac{T^{2/3}}{P_{atm} \cdot \sigma_{ij}^2 \cdot \Omega_{ij}} \cdot \sqrt{\frac{M_{wi} + M_{wj}}{M_{wi} \cdot M_{wj}}} \quad (2.5)$$

where

M_w [g/mol] molecular weight

P_{atm} [atm] total pressure

r_p [m] pore radius

T [K] temperature

σ_{ij} [Å] Lennard-Jones collision diameter, $\sigma_{ij} = (\sigma_i + \sigma_j)/2$

Ω_{ij} - collision integral according to Neufield

$$\Omega_{ij} = \frac{1.06036}{(T^*)^{0.1561}} + \frac{0.19300}{\exp(0.47635 \cdot T^*)} + \frac{1.03587}{\exp(1.52996 \cdot T^*)} + \frac{1.76474}{\exp(3.89411 \cdot T^*)}$$

where $T^* = \frac{T}{(\epsilon_{ij}/k_B)}$, k_B being the Boltzmann constant

ϵ_{ij} [J] combined Lennard-Jones constant, $\epsilon_{ij} = \sqrt{\epsilon_i \cdot \epsilon_j}$

Stefan-Maxwell Model

One of the models that take into account the interaction between different species is the Stefan-Maxwell model. Stefan and Maxwell have, independent of each other, formulated this relationship where the flux is dependent on the fluxes and transport resistances of all components:

$$\frac{dc_i}{dz} = \sum_{\substack{j=1 \\ j \neq i}}^n \frac{J_j \cdot x_i - J_i \cdot x_j}{D_{ij}} \quad (2.6)$$

Not the Fick's first law but only such a model can represent the phenomena that can be observed for multi-component systems: *osmotic diffusion*,

where the flux of a component appears without a concentration gradient; *diffusion barrier*, where no flux appears for a component although a concentration gradient is present; and *reverse diffusion*, where the flux of a component is against its concentration gradient.

Various text books and publications cover the Stefan-Maxwell model, see for example: Do¹⁶, Wesselingh and Krishna²¹, Krishna and Wesselingh²², Cussler²³.

Dusty-Gas Model

The so called *dusty-gas model* is actually an extension of the Stefan-Maxwell equations and is usually covered along with it. In this approach, the porous structure, where the diffusion is taking place, is also taken into the equation as an additional species. The pores are assumed to be made up of very large, stationary particles; therefore these can be assumed to be *dust* particles compared to the gaseous species. Shortly, the interaction of the gas molecules with these dust particles are then taken into account by the addition of a Knudsen diffusion term. This is because the interaction of gas molecules and the dust is actually representing the molecules colliding with the pores. Consequently, the final equation looks like:

$$\frac{dc_i}{dz} = \sum_{\substack{j=1 \\ j \neq i}}^n \frac{J_j \cdot x_i - J_i \cdot x_j}{D_{ij}} - \frac{J_i}{D_i^{Kn}} \quad (2.7)$$

Basically, the left-hand side of the equation stands for the driving force and the right-hand side for the transport resistances.

Adsorption/Desorption

The basic requirement for heterogeneously catalyzed reactions is the adsorption of at least one of the reactants. The most frequently used model for adsorption in heterogeneous catalysis is the Langmuir adsorption model. For a system under adsorption/desorption equilibrium, the model equation reads as follows:

$$\theta_i = \frac{K_{eq}P_i}{1 + \sum_i K_{eq,i}P_i} \quad (2.8)$$

where θ_i is the surface coverage of the species i , the K_{eq} is the equilibrium constant and P_i is the partial pressure.

The basic assumptions of the Langmuir adsorption model are that there are no interactions between adsorbed species, the sites are identical and that the heat of adsorption is independent of coverage. In reality, none of these conditions are satisfied. Nevertheless, the equation is taken to be a good estimation and commonly used.

Surface Diffusion

Surface diffusion, as the name implies, is the diffusion of an adsorbed species on the surface. In general not only the species' parameters but also the surface properties and the interaction between the surface and the species become important for this type of diffusion. For example, a very strong adsorption, i.e., chemical adsorption, may not favor surface diffusion by keeping the adsorbed species immobile, but on the other hand physical adsorption offers a weaker bond between the surface and the species, and thus may lead to easier transport of molecules on the surface. Or the topology of the surface may have an effect on the diffusion process. Depending on the conditions, the surface diffusion may or may not be significant for the total transport of species. For example, some species, such as argon, helium, nitrogen, are assumed to have no surface flow in general, due to their tendency of not being adsorbed appreciably.

In addition to these, *configurational diffusion*, where the molecule-wall interactions strongly influence the diffusion process, *single-file diffusion*, where molecules cannot take over each other due to very small pores, and *capillary condensation/flow*, where gas molecules condense and thus are transported in liquid phase, can be counted among the transport mechanisms that can occur inside the pores of catalysts.

2.4 Ethylene Hydrogenation

Hydrogenation is certainly the most studied reaction in organic chemical catalysis²⁴ and it has found numerous applications in organic synthesis in research and industrial processes. Almost all catalytic hydrogenations have been accomplished using heterogeneous catalysts since the earliest stages²⁵. The probe reaction chosen for this study is also a hydrogenation, namely, the hydrogenation of ethylene. It is chosen based on the fact that it involves simple molecules, proceeds at ambient temperature and produces only ethane. Thus, the over-all reaction is a simple single-reaction, where $A + B \rightarrow C$. It is one of the most studied reactions²⁶, since it incorporates the hydrogenation of the simplest possible unsaturated hydrocarbon. Thus, in general, it is expected to be of a simpler nature, and it has been studied extensively with the hope that a full understanding of its chemistry would provide information about the hydrogenation, exchange, dehydrogenation and isomerization of more complicated alkenes²⁷. Additionally, since ethylene is of particular importance due to its widespread use as a cheap raw material, and the production of polymer-grade ethylene requires the selective hydrogenation of acetylene, knowledge about ethylene hydrogenation turns out to be important for the minimization of this unselective route²⁸.

There are various studies on heterogeneous hydrogenation of ethylene, such as: on Pt^{27,29-39}, on Pd^{26,28,40-44} and others⁴⁵⁻⁵². Generally, the mechanism proposed by Horiuti and Polanyi⁵³ in the 1930's is accepted as a reasonable mechanism⁵⁴. In this mechanism, ethylene is adsorbed on the surface by using one of the carbon-carbon double bonds, this is followed by stepwise hydrogenation with atomic hydrogen (formed from dissociatively adsorbed molecular hydrogen) through an ethyl intermediate to form ethane, which is desorbed into the gas phase²⁷ (see fig.2.2):

Actually, this is only one of the many mechanisms proposed for this reaction. For instance, Farkas and Farkas³⁸ proposes another mechanism where ethylene is first dehydrogenated before hydrogenation occurs. A third mechanism, proposed by Zaera and Somorjai³⁴, involves the intermolecular hydro-

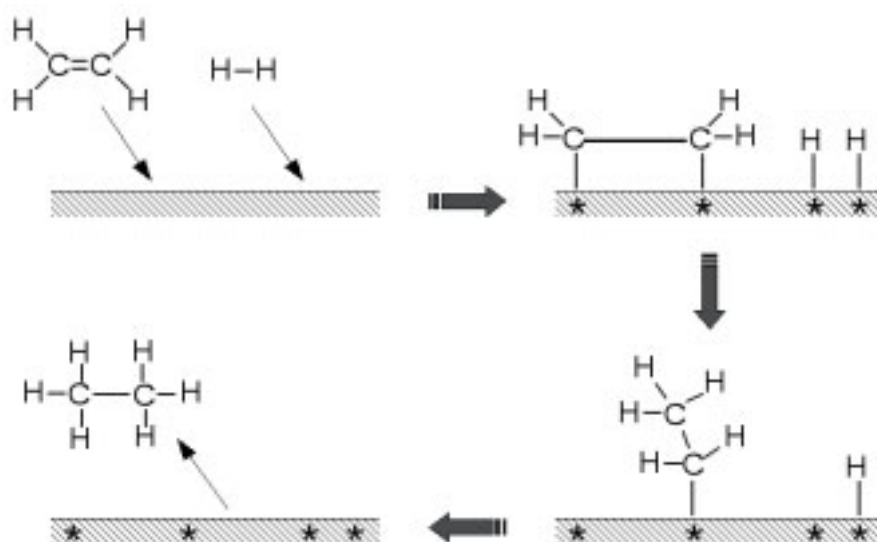


Figure 2.2: A simple representation of Horiuti-Polanyi mechanism.

gen transfer from surface ethylidyne to co-adsorbed ethylene intermediates.

In fact, being one of the fastest heterogeneous catalytic reactions, the hydrogenation of ethylene is a deceptively simple reaction; it possesses an extremely rich and complicated chemistry²⁷. For example, Cortright *et al.*³⁹ reports about the dependence of reaction orders on temperature and partial pressures, and proposed that a combination of different reaction pathways might describe the behaviour; Heese³⁷ gives experimental evidence about the oscillatory behaviour of the reaction and focuses on the possible complex surface phenomena that may be behind it. Consequently, it can be said that despite its simple structure, ethylene hydrogenation is a challenging reaction system.

2.5 Experimental Reactors

Collection of different kind of information is aimed in the study of catalysts and reactions. The most common goals can be listed as the comparison of different catalysts for a given reaction, the evaluation of reaction kinetics, the evaluation of the sensitivity of catalyst to possible poisons, the testing of catalyst durability and regenerability^{55,56}. Particularly speaking, two types of laboratory reactors for two different aims were utilized in this work: a

turbo-reactor for kinetic measurements and a single-pellet reactor for the study of the effect of the pore structure for the given probe reaction.

2.5.1 Kinetic Measurement Reactors

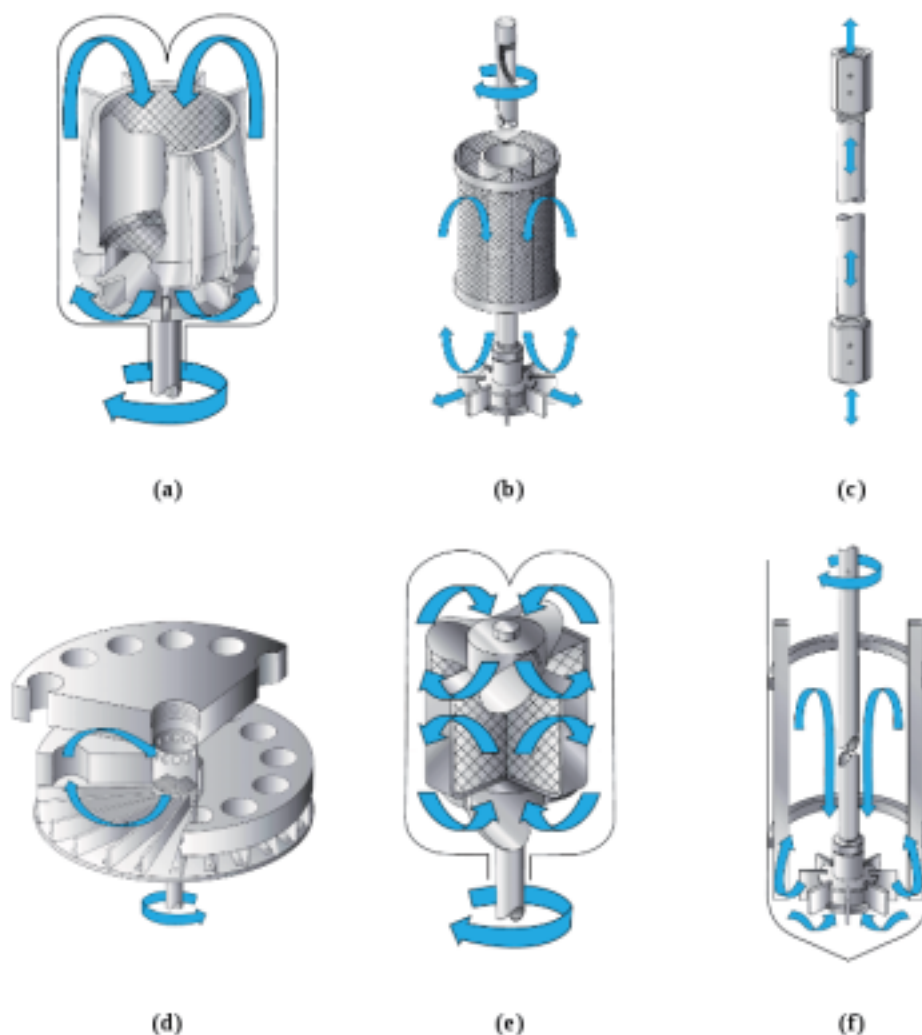


Figure 2.3: Common types of reactors used in catalytic research⁵⁷. a) Berty reactor, b) Harshaw falling basket reactor, c) fixed bed (tubular) reactor, d) Caldwell reactor, e) Carberry spinning basket reactor, f) stirred (batch) reactor.

There are various types of reactors that can be used in catalytic research. In fig.2.3, some common types of these reactors can be seen. In general, it can be said that the reactors for kinetic studies are designed to perform like ideal-batch reactor, or ideal-flow reactors, PFR (plug flow reactor) or CSTR (continuous stirred tank reactor), due to the ease of analysis. Also other

categorizations may be made based on the prevailing concentration profile inside the reactors, *differential reactors* that lead to only small conversion, and *integral reactors* that show large conversions alongside them; or based on the mixing/recycling of gas, *internal* or *external recycling*.

An ideal-batch reactor is preferred for rather slow reactions, it is assumed to be perfectly mixed, i.e., it has no concentration or temperature gradients. It gives data with respect to time, i.e., it is under unsteady-state operation. The definition of $t = 0$ for such reactors can be said to be hard in general.

An ideal plug-flow reactor can be operated at steady-state, but the concentrations change along the reactor length and the data is usually taken at the exit. The assumptions for such a reactor are: no concentration gradient in radial direction, no diffusive flow parallel to flow direction and that there exists a plug flow inside. If it is used as an integral reactor, where the conversions are large, concentrations of the intermediates at the exit may be too low for detection. In such a case, spatial probing can be a solution.

An ideal CSTR configuration is also used often and is very valuable for kinetic studies in heterogeneous catalysis. The assumption behind this type of reactor is also the concentration (and temperature) homogeneity inside it. Basically, it can be viewed as an ideal-batch reactor connected to continuous inlet and outlet flows, and thus can achieve steady-state operation. At steady-state, it can be described by the simplest mathematical model since concentrations and temperature depend neither on coordinate, nor on time.

General information and more details about laboratory reactors can be found, for example, in Forni⁵⁸ and from AutoclaveEngineers⁵⁷.

In this work, the kinetic measurements are performed using a patented⁵⁹ turbo-jet reactor. It is an internal-recycle reactor which is constructed to give good mixing even at low gas densities, and operates practically under ideal CSTR-behaviour⁶⁰.

2.5.2 Single-Pellet Reactor

The so called *single-pellet reactor* is the type of reactor with which the center concentration of a catalyst pellet can be measured. It consists of two chambers that are separated from each other by a porous catalyst block. The name “single-pellet”, literally, could give the impression that the whole block is made up of porous catalyst or that there should exist only a (large) single pellet embedded into a pellet-holder plate separating the two sides. But actually, the reactor could also function with a plate containing many (parallel) (smaller) pellets of the same kind. Thus, the name should be taken to represent the idea of the set-up, not the number of pellets used in it.

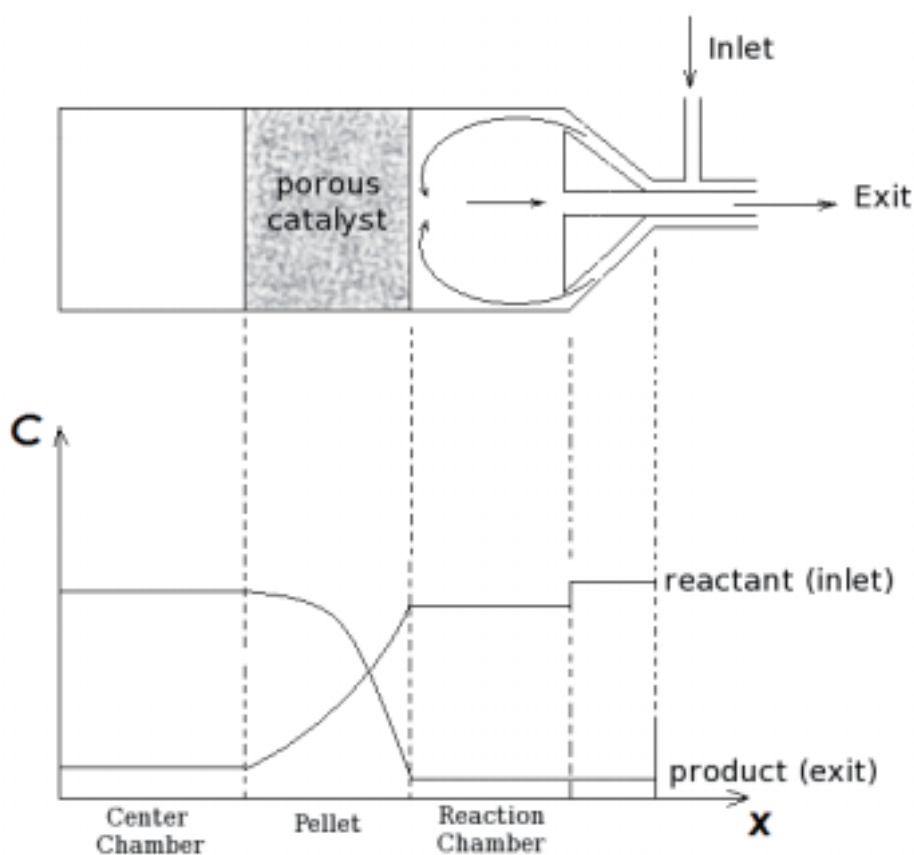


Figure 2.4: Simple scheme of a single-pellet reactor with sample concentration profile inside.

The construction of the reactor is such that one of the two chambers has both inlet and outlet flows connected to it, and the other one has no flow, i.e., a closed-chamber. Since the connection between these two chambers are through the catalyst (pores) only, a concentration profile builds up inside the

catalyst and the two chambers accordingly. At steady-state, the concentration in the closed-chamber corresponds to the concentration at the center of a two times longer catalyst pellet. That is why the concentration measured at the closed-chamber is named as the *center concentration*. A pictorial representation of a single-pellet reactor and the concentration profile inside are given in fig.2.4.

Maybe the first studies with such a reactor configuration, one that enables center concentration determination, is done by Roiter *et al.*⁶¹ at 1950's. A closed chamber version is but used later in 1960's by Balder and Petersen⁶². Moreover, a single-pellet reactor utilizing a small infra-red cell is designed by Hegedus and Petersen⁶³, and the determination of the center chamber concentration without sample taking had become possible. A summary of the theory and applications of the single-pellet (diffusion) reactor can be found in the work of Hegedus and Petersen⁶⁴. More recent studies also present the various applications of this reactor in scientific research, see e.g., Dogu *et al.*⁶⁵, Au *et al.*⁶⁶, Cabbar *et al.*⁶⁷, Dogu *et al.*⁶⁸, Nett-Carrington and Herz⁶⁹.

A single-pellet reactor is also utilized in this work. It is successfully used to determine the reaction rate and the center concentrations for catalyst pellets with different pore structures under the same operating conditions.

Part III

Core of Work

“Bilgini ve tecrübelerini kendine saklamak bencilliklerin en büyüğüdür...”

“Keeping your knowledge and experiences just for yourself would be the biggest selfishness...”

3

Work Done

This chapter concentrates on the work done during this study. Both the experimental and theoretical parts of the work are given emphasis in this chapter. The corresponding summaries of these two main sections can be found at the beginning of each section.

3.1 Experimental Work

This section concentrates on the work for and about the experimental part of the thesis. It starts with the re-design considerations about both of the reactors and the experimental set-up. Some improvements and changes made to the reactors are noted, and the flow-scheme of the experimental set-up is given. Various pellets used and their characteristics are tabulated. Then emphasis is given to the results from the individual reactors. The most relevant results from the single-pellet reactor are discussed: the behaviour of the reaction rate and the center mole percentages with respect to pore structure and temperature are shown. Later on, the kinetic models used to fit the turbo reactor data are listed. A discussion about the best fit and the parameters are also given.

3.1.1 Re-design and Improvement of Single-Pellet Reactor

One of the preliminary preparations for the experimental work was the re-design and construction of a single-pellet reactor (SPR) that was going to be inserted into an oven for temperature control. An SPR was already available at the institute, which was used as a part of another thesis (Rieckmann⁷⁰). Due to some practical handicaps of this previous design, certain improvements were possible. Representative drawings of the old and new versions of the SPR can be seen in fig.3.1.

The basic handicap was the graphite-gaskets that were used. They were hard to get gas-tight because of the tilting of the two separate halves as a result of the uneven tightening of the four large nuts. Although even-adjustment of tightening was possible using appropriate tools, the force required to tighten/loosen the large nuts was hard to achieve due to the relatively small space inside the oven. Also due to the design of the reactor and the surrounding pipes inside the oven, one of the nuts, the one located close to the back-side of the oven, was very hard to reach. Therefore, replacing the pellet-holder and getting the reactor gas-tight afterwards was hard, moreover time consuming.

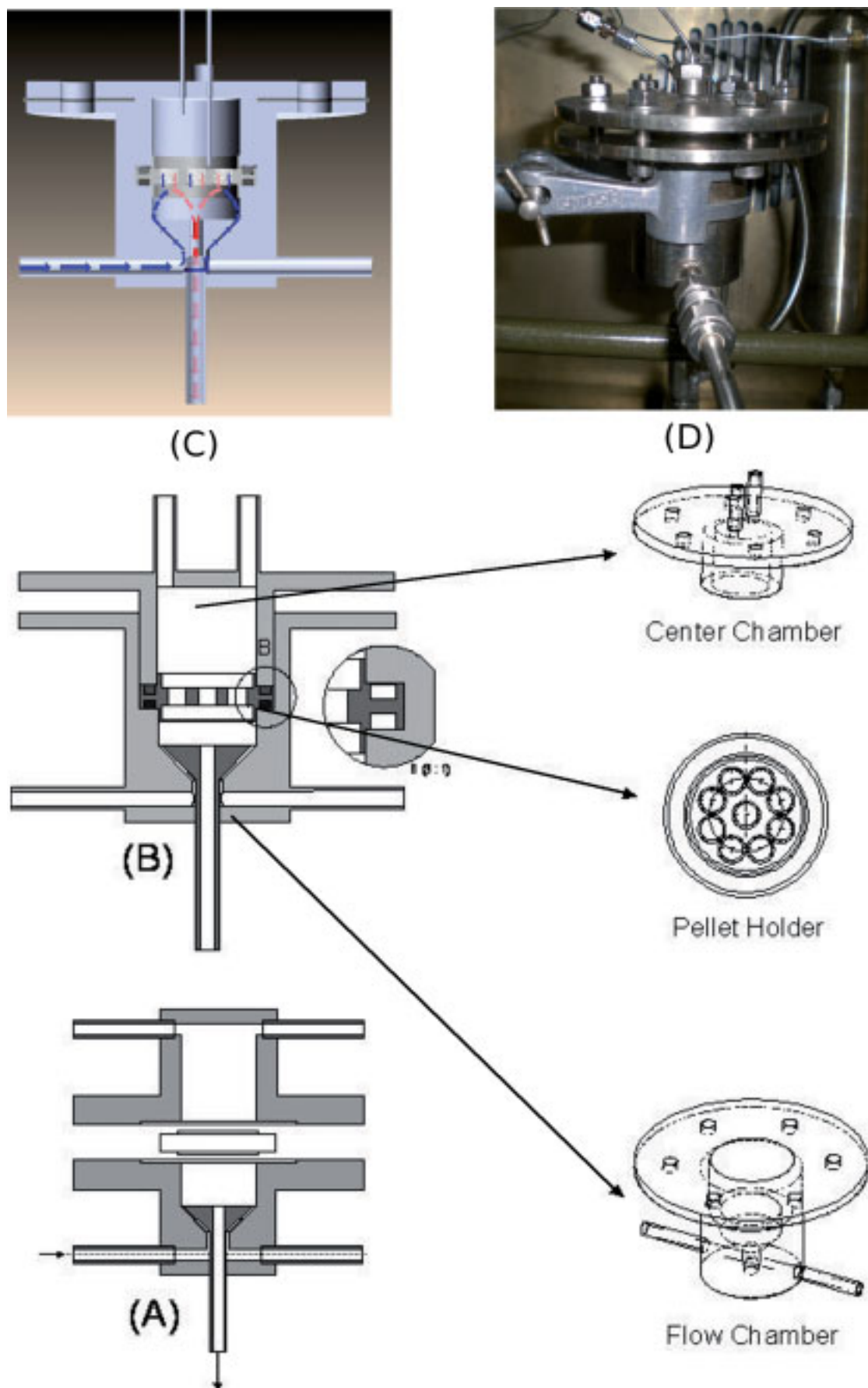


Figure 3.1: Drawings and pictures of the single pellet reactors. A) drawing of the SPR from the previous study⁷⁰, B) drawing of an improved design, C) 3-D drawing of the final version, D) picture of the constructed SPR in oven.

After considering various gasket types, it has been decided to use o-ring gaskets, which do not require considerable forces to tighten. But they require some grooves to be inserted. Thus, the design of the pellet holders had been changed accordingly to include such grooves (see fig.3.1 close-up section and pellet holder). Consequently, instead of four large bolts, six small bolts are used in the design (fig.3.1 (B) center- and flow-chambers, and (D)) with corresponding small nuts. Even hand-tight nuts were then able to make the reactor gas-tight for low pressures owing to this design.

By keeping the current design and changing only the gasket-type, a recurrence of the tilting problem was still possible for getting gas-tightness at high pressures. This problem is dealt with inserting one half of the reactor into the other (see fig.3.1 (B) compared to (A)). In that way the possibility of lateral shift and/or tilting are avoided.

The two 6mm pipe connections to the center-chamber (upper-chamber) (see fig.3.1 (A)), which were to the sides are now taken to be perpendicular to the top-wall of the chamber (fig.3.1 (B)), thus clearing the reach to the nuts. These pipes connected to the center-chamber serve for the sample-taking, and pressure and temperature measurements. The reason to have relatively large pipes here was to allow the insertion of the temperature probe into the chamber. Another change thus was reasonable: the sample-taking and pressure measurement are again done through two pipes, but this time $1/8\text{inches}$ in diameter, and the temperature probe is inserted from another opening close to the center of the top-wall (see fig.3.1 (C) and (D)), making the space reserved for these insertions much more compact and the reach to the nuts easier.

The final design (fig.3.1 (C)) is then constructed (fig.3.1 (D)) in the mechanical workshop of the university and successfully used in the experiments.

3.1.2 Re-design of Turbo-Reactor

The patented⁵⁹ turbo-reactor at the institute is a differential reactor with internal recycle. It has a single stage propeller-wings (turbine mixing) and

also makes use of the inlet flow as a jet(turbo)-stream to achieve good gas mixing even at low gas densities. It is acquired from the *Reaktionstechnik* department of *Martin-Luther-University, Halle-Wittenberg* where it had been developed. The reactor interior is so designed that it directs and routes the gas in a way to support and maintain good gas circulation⁶⁰. The catalyst housing is ring-shaped, and its height can be altered so to allow for different catalyst loadings. This housing is located at the upper half of the reactor and it faces the ring-shaped propeller located at the lower part (see fig.3.2). Above 3000 rpm, the reactor shows nearly ideal-CSTR behaviour and has very good mixing⁶⁰.

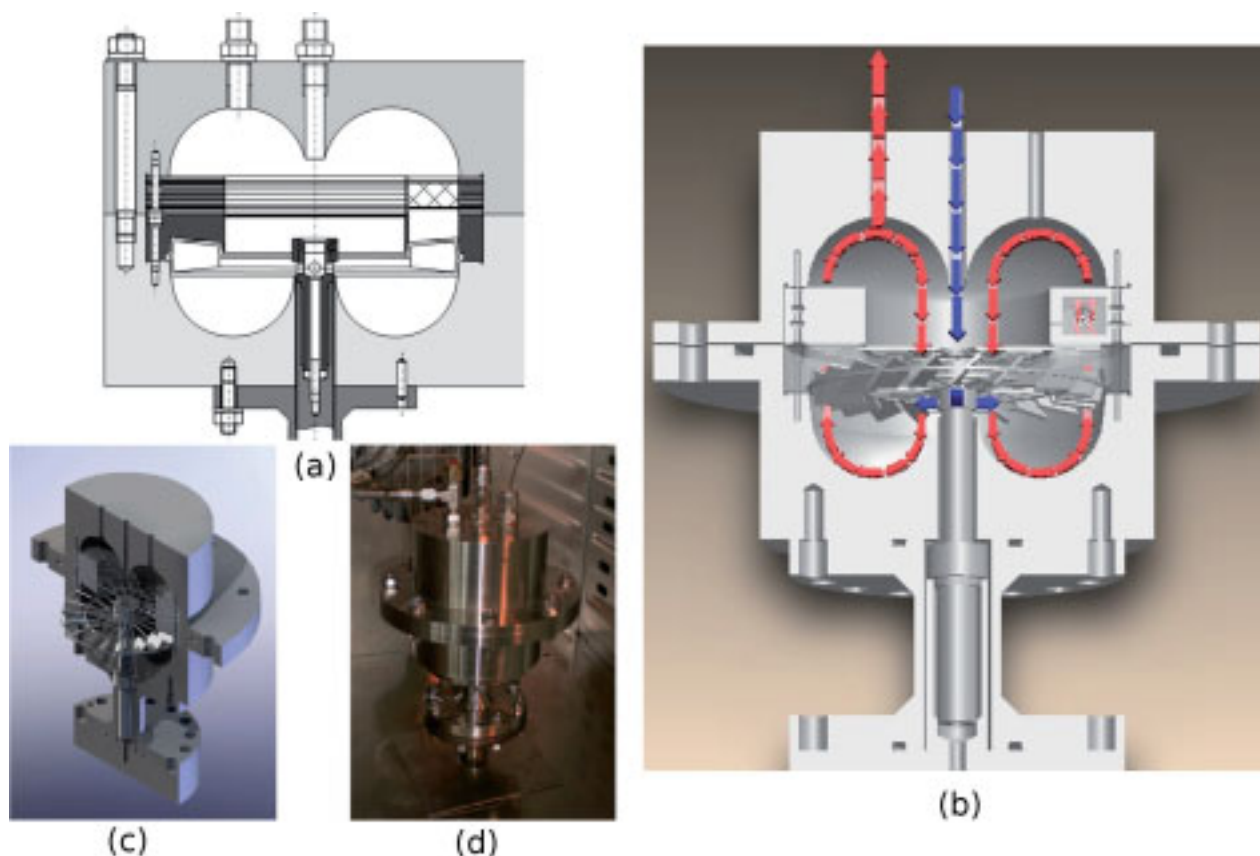


Figure 3.2: Drawings and pictures of the turbo reactors. a) drawing of the original turbo reactor, b) drawing of the new design with paths, c) 3-D view of the new reactor, d) picture of the constructed turbo reactor in oven.

From practical and experimental points of view, the actual design and the size of this reactor were not appropriate for the purposes of this thesis. The reactor and catalyst cage volumes were too large requiring high catalyst loadings and flow rates for proper operation, the gasketless flange assembly

was also hard to get gas-tight due to wear off in years and also required relatively large force for tightening. Moreover the heating of the reactor was done by an electrically driven heating coil that was to be wrapped around the reactor. The heat-isolation was to be achieved by wrapping isolation ribbon over the wrapped-coil. Therefore, the loading of the catalyst was only possible after unwrapping the isolation and the heating coil, which later after loading had to be wrapped again carefully. Due to these handicaps, the operation of this reactor was also not user-friendly requiring intensive care (to avoid tearing off of the heating coil) and extensive time devotion during preparations.

Taking into these points into consideration, first the reactor is scaled-down to around 4.2 times smaller volume. The material of construction was nickel galvanized CuNi_2Si , which was chosen to give good heat transfer through the relatively thick reactor wall, and the galvanization was done to hinder any reaction that might be catalyzed by the internal surface of the reactor. In the new design, stainless steel was used instead. This has the advantage of higher mechanical strength thus allowing thinner walls and lighter reactor, and it is also not catalytically active so the possibility of surface reaction on the inside of the reactor is prevented. Since smaller dimensions are used, same operating pressures can be achieved using thinner walls, consequently the drawback of lower heat transfer rates (due to lower heat transfer coefficient of stainless steel) is compensated. The untight gasketless flange assembly is replaced by o-ring gaskets. This allowed the usage of smaller nuts and bolts, again leading to easier tightening/loosening. The reactor is placed inside an oven for temperature control. On the other hand, the motor driving the propeller is left outside the oven in order to protect it from high temperatures. The shaft connecting the motor and the propeller is inserted into the oven from a hole drilled through the floor of the oven. As a result, there was no need for wrapping of the heating coil and the isolation ribbon. These, altogether, allowed for faster and easier loading of the reactor, and greatly decreased the time between subsequent runs. The final design is constructed in the workshop of the university (TUHH) and successfully used for kinetic measurements.

The original and the new design of the reactor, along with its picture inside the oven can be seen in fig.3.2.

3.1.3 Building-Up Experimental Set-up

The experimental set-up; two reactors, measuring and flow-controller equipment, and gas-chromatograph for analysis, is also designed and self assembled. The whole flow diagram of the set-up can be seen in fig.3.3.

The experiments with the single-pellet reactor (SPR) require longer runs (>24hrs.) to reach steady-state, and thus the reactor needs to be left without supervision during some part of the experiments. Therefore, for safety reasons, a hydrogen sensor is used to check the gas content inside the oven, which in case of any leak, has the ability to cut-down the inlet flow. The mixing chamber before the SPR is a chamber filled with glass-beads, and serves for the equilibration of temperature of the inlet gases with the reactor. Also it serves as a reservoir (large volume) to avoid larger pressure drops during sample-taking. The temperature on the two sides of the pellet holder, the pressure on the reactor chamber side along with the pressure difference across the pellet holder can all be monitored. Thus, pressure and temperature gradients across the pellet can be monitored. Also, for the turbo-reactor, monitoring of the temperature of the catalyst cage and the reactor volume, along with the pressure inside the reactor was possible.

The 6-way valve, V11, and the sample loop connected to it (between connections 2 and 5 of V11) are the heart of the sample-taking. In the position shown in the fig.3.3, this sample loop is connected to a vacuum pump (for purging gases) through V9 and V10. In the second possible position, that is achieved by switching V11, a connection of the sample loop to the chromatograph is possible, thus sending the sample (kept inside sample loop) for analysis. In general, the sample loop is first emptied by making a vacuum, then using corresponding valves, the sample is sucked into it (from the desired reactor and position), after that it is connected to atmosphere (through V17) for pressure equilibration and finally by switching V11 this sample is sent to chromatograph for analysis. The (atmospheric) pressure equilibra-

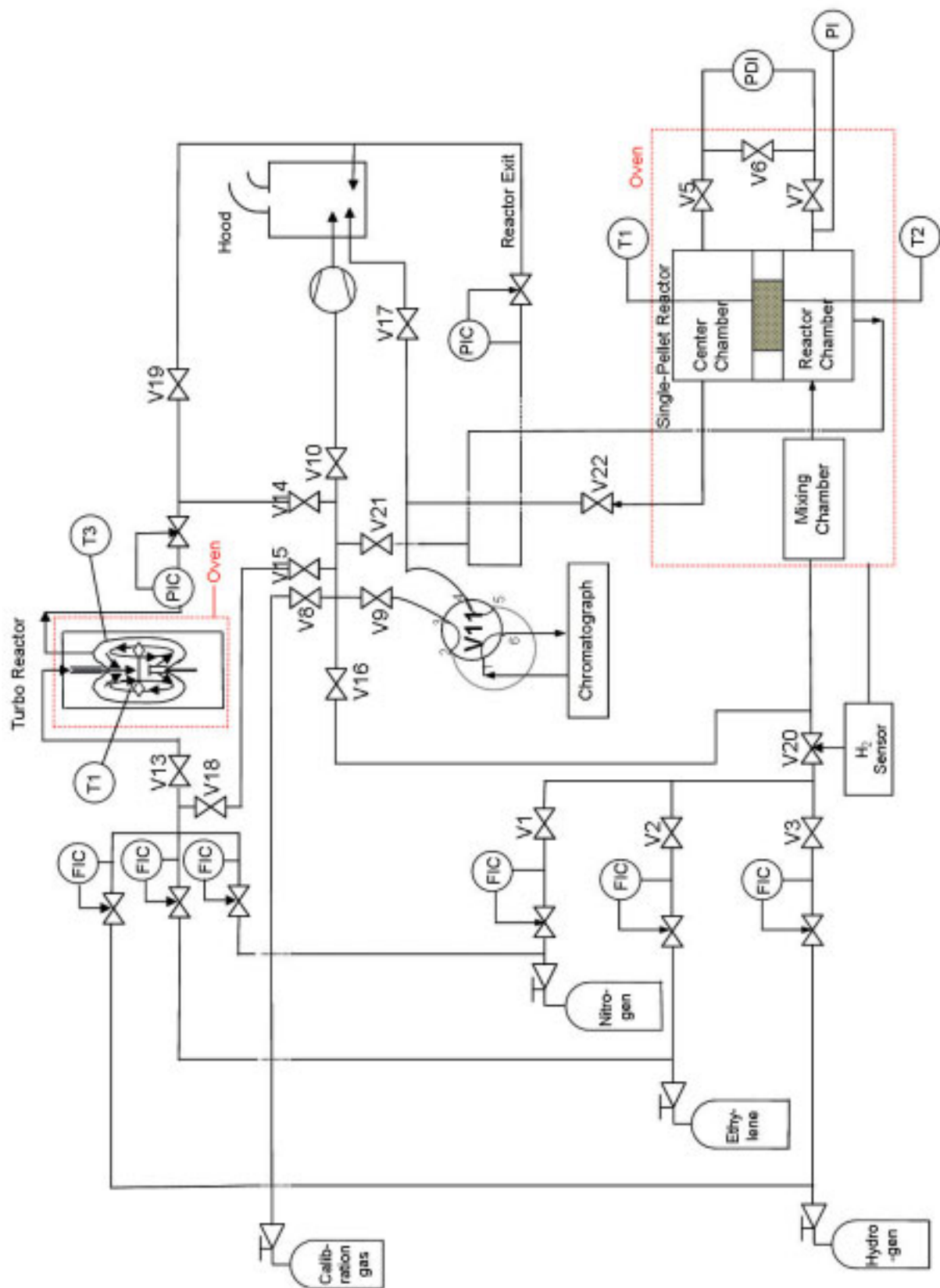


Figure 3.3: Flow-chart of the experimental set-up.

(FIC: flow rate indicator and controller; PDI: pressure difference indicator; PI: pressure indicator; PIC: pressure indicator and controller; T: temperature measurement; V: valve)

tion is required to make sure that everytime the same amount of sample (at atmospheric pressure and temperature) is analyzed, and thus the samples taken are comparable. Additionally, a calibration gas with known composition of gases is analyzed after each and every sample-taking to determine the composition of the samples.

3.1.4 Pore Structure Analysis

The determination of the pore size distribution of the pellets used is done by both nitrogen-sorption and mercury-porosimetry measurements. Beside that, mean pore radius, specific surface area and porosity are also extracted from these measurements. The measurements are performed partially in our institute and partially at the “Bauphysik” department of our university. There was also some limited data supplied by the manufacturer. The results from mercury-porosimetry, nitrogen-sorption and manufacturer (nitrogen-sorption) data are then all analyzed to determine the most reliable results. With respect to the equipment used, it can basically be said that the mercury-porosimetry is found to be the more suitable analysis for the pore ranges the pellets had. In many cases, nitrogen-sorption was not able to determine some part of the pore size distribution. Therefore, the results presented in table 3.1 correspond to mercury-porosimetry analysis. On the other hand, nitrogen-sorption measurements can in general be thought to be focusing on finer pores, giving a cross-checking of the results from mercury-porosimetry for that region.

In table 3.1, various properties of the used pellets are summarized. Two different catalyst distribution types (egg-shell or homogeneous), different active materials (Pd or Pd-Ag), various loadings (0.001-0.3 wt.%) and various surface areas ($7.6-108.5 \left[\frac{m^2}{g}\right]$) can be noticed at first glance. On the other hand, the pellet dimensions and the porosity were tried to be kept relatively constant. So the pellets can be grouped in various ways for comparison.

Table 3.1: Characteristic values for the catalyst pellets used. In all cases, the active material (catalyst) is impregnated onto an alumina support. In the table; \tilde{r}_{pore} represents the peak value of the pore radius distribution from the differential intrusion curve, \bar{V}_{pore} is the pore volume, $\bar{\epsilon}$ is the porosity, \bar{D}_{pellet} and \bar{L}_{pellet} are average diameter and length, \bar{m}_{pellet} is average mass and S_{area} is the surface area.

Name Y-.....	Active Mat.	Loading [wt. %]	Distr.*	\tilde{r}_{pore} [nm]	\bar{V}_{pore} [$\frac{cm^3}{g}$]	$\bar{\epsilon}$ [%]	\bar{D}_{pellet} [mm]	\bar{L}_{pellet} [mm]	\bar{m}_{pellet} [g]	S_{area} [$\frac{m^2}{g}$]
40079	Pd ^e	0.035	bi-	117 <5	0.206 >0.227	63	4.3	4.4	0.096	14.0
40787	Pd-Ag ^e	0.035	bi-	68 12.6	0.309 0.146	64	4.3	4.7	0.106	42.6
40788	Pd-Ag ^e	0.035	bi-	74 9.6	0.025 0.552	65	4.7	5.1	0.105	108.5
40789	Pd-Ag ^e	0.035	mono-	116	0.429	60	4.4	4.6	0.100	9.2
41303	Pd ^e	0.1	mono-	113	0.398	59	4.3	4.5	0.103	7.9
41304	Pd ^e	0.3	mono-	113	0.405	61	4.3	4.5	0.102	8.9
41573	Pd ^h	0.3	mono-	110	0.410	61	4.4	4.6	0.101	15.9
41574	Pd ^h	0.3	bi-	118 13	0.466 0.010	63	4.4	4.6	0.090	13.5
41575	Pd ^h	0.3	bi-	84 13	0.321 0.135	63	4.5	4.9	0.105	31.4
41874	Pd ^h	0.03	mono-	223	0.418	61	4.4	4.6	0.100	7.6
41875	Pd ^h	0.03	bi-	216 23	0.469 0.012	64	4.6	4.6	0.090	12.3
42099	Pd ^h	0.001	mono-	110	0.417	60	4.4	4.6	0.103	14.2
42100	Pd ^h	0.001	bi-	117 11	0.485 0.015	65	4.4	4.6	0.090	20.2
42218	Pd ^h	0.001	tri-	304 54 11	0.021 0.356 0.032	58	4.4	4.5	0.098	21.2

* pore radius distribution; mono-disperse, bi-disperse and tri-disperse indicating one, two and three distinct peaks in pore size distribution results from mercury-posimetry.

e : egg-shell loading, *h* : homogeneous loading

3.1.5 Experimental Results from Reactors

Single-Pellet Reactor

Constant inlet flow-rate and compositions are used for all different series of experiments. The response of the reactor, i.e., the exit and center concentrations, are then measured. The pressure is kept constant and the temperature is varied, and the pattern with respect to temperature is also investigated.

In all the experiments, the concentration of the nitrogen is found to be higher in the center chamber than the reaction chamber. This finding is an indication of the interaction between different components, that is, the effect of a species' flux on the other's concentration gradient. The ethylene and hydrogen diffusing into the pellet drag nitrogen in the direction of the center chamber. The reaction product, ethane, on the other hand flows in the opposite direction and drags nitrogen backwards. Due to the reaction stoichiometry, ethylene, hydrogen and ethane have the same value of fluxes, ethane being in the opposite direction. As an early guess, one would expect that the effect of ethylene and ethane, which are roughly similar in structure, would cancel and due to the excess hydrogen flux in the direction of center chamber nitrogen concentration would be higher in the center. The results support this early hypothesis about the behaviour of the nitrogen. Additionally, this behaviour is a clear indication of the interaction between the fluxes. This phenomenon, one of the species building a concentration gradient without having net-flux, is already known to occur in multi-component diffusion systems and is named as *diffusion barrier*.

In the first series the catalyst Y40079, Y40787, Y40788 and Y40789 are usedⁱ. These pellets have all a Pd loading of 0.035% with different pore structures. The results for this series are summarized in table 3.2.

One can notice from the exit compositions (see table 3.2) that for catalyst Y40789 no product could be detected at the exit. Although some product was found at the center chamber, practically the reaction rate was zero. Thus Y40789 was not taken into account any further.

ⁱMore detailed information about this series can be found in Chilamkurthi⁷¹.

Table 3.2: The experimental results for series **SP1**, the **Single Pellet** reactor series **1**. Nine pellets are used for each experiment, the pressure was 3 bara and total inlet flowrate was 200 [ml_{rc}/min] with the following composition: 60.3% N_2 , 20% C_2H_4 , and 19.7% H_2 . Each experiment is repeated at least once and the average value of these data are shown in the table.

SP1_	Pellet	T [°C]	Exit Composition [%]				Center Composition [%]			
			N_2	C_2H_4	C_2H_6	H_2^*	N_2	C_2H_4	C_2H_6	H_2^*
1		60	59.7	20.1	0	20.2	60.0	18.3	0.3	21.3
2	Y40789	120	60.0	20.2	0	19.8	60.7	18.2	1.2	19.9
3		180	59.8	20.1	0	20.1	60.5	19	0	20.5
4		60	62.8	15.8	5.3	16.1	65.9	0	21.6	12.5
5	Y40079	120	63.0	15.8	5.1	16.1	65.7	0	21.5	12.8
6		180	62.3	16.8	4.4	16.6	65.0	0	21.4	13.6
7		60	63.3	15.2	6.1	15.5	66.5	0.6	20.9	11.9
8	Y40787	120	63.0	15.7	5.8	15.5	66.1	0.9	21.0	12.0
9		180	62.3	16.4	4.8	16.5	65.0	0.7	21.1	13.2
10		60	63.7	14.5	7.1	14.7	67.2	0.8	21.0	11.0
11	Y40788	120	63.0	15.8	5.1	16.1	65.9	1.2	20.3	12.7
12		180	62.4	16.4	4.3	16.9	65.2	1.1	19.7	14.0

* The detection of H_2 was not possible with the equipment in use, and thus it is calculated by subtracting the other values from 100. As a result, H_2 values accumulates the errors from others and have the most uncertain values.

A plot of reaction rate against the temperature for SP1 can be seen in fig.3.4. Ethylene is used as the tie component for the calculation of the reaction rates, that means, an ethylene mass balance is made between the inlet and exit, and the rate of consumption of ethylene is calculated. There are various points this figure leads to. At first glance, one can notice that the reaction rate decreases with increasing temperature. This, even though not very common, is a known phenomenon in heterogeneous catalysis. The reason of such a decrease is the effect of the surface coverage on the reaction rate. Even though the reaction rate constant increases rapidly with temperature due to Arrhenius' Law, the adsorption constants decrease and the surface can become so low in coverage that the reaction rate decreases with increas-

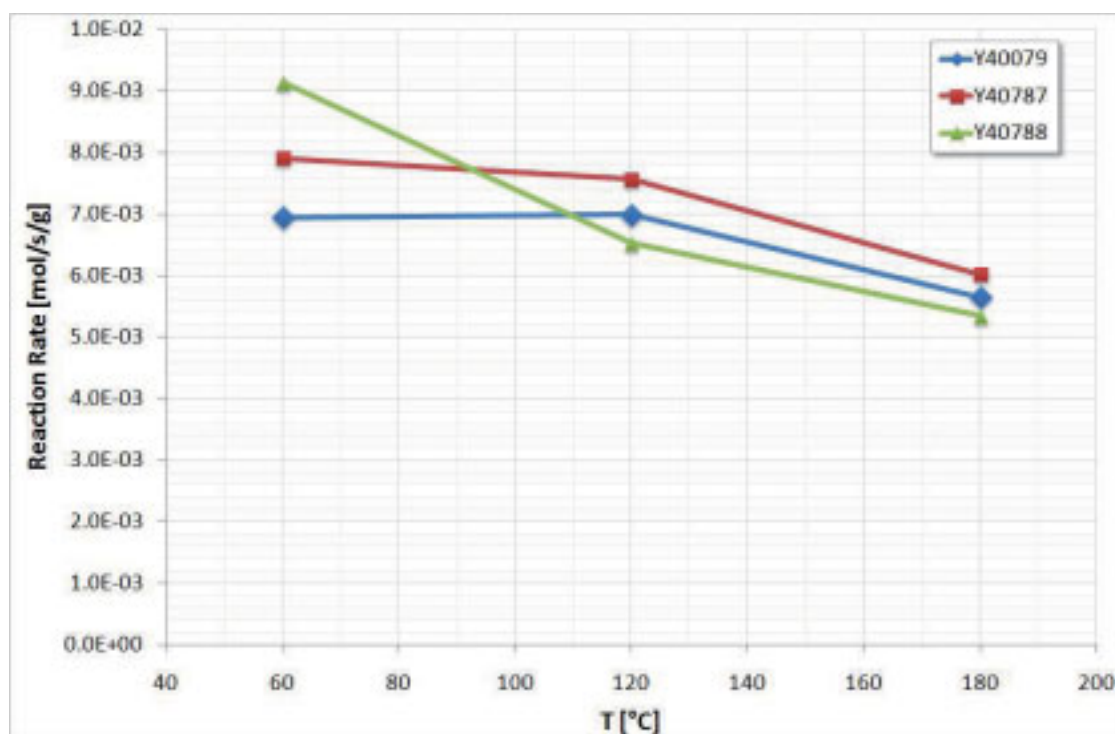


Figure 3.4: Plot of temperature vs reaction rate for experimental series SP1.

ing temperature. Such a behaviour is known to occur also, for example, for the oxidation of carbon-monoxide. Nevertheless, it should be noted that this behaviour is highly dependent on the reaction conditions, i.e., concentration of the species, their relative ratios, temperature, pressure, catalyst, etc. Consequently, changing some of these parameters will easily bring the system to the more common case, reaction rate increasing with temperature.

From the figure (fig.3.4), it can also be noticed that the Y40788 is most affected from this reaction rate decrease. It should be reminded that this particular pellet has the highest surface area ($108.5 [m^2/g]$) among the three. Because of this difference in response to temperature, the optimum pore structure becomes dependent on temperature, or more generally, on operating conditions. For 60°C Y40788, but for 120°C Y40787 ($42.6 [m^2/g]$) gives the highest reaction rate and consequently the highest conversion. So the rule of thumb, “the higher the surface area, the faster the reaction rate” is not valid for this case.

Another notice should be made for the center composition (see table 3.2). The ethylene concentration in the center has either very low values

(Y40787 and Y40788) or it is zero (Y40079). This indicates that the diffusion resistance is high and ethylene could hardly reach the center chamber. In such a case, it becomes harder to discuss about the concentration profile inside the pellet because for all the pore structures the values are close to each other. Therefore, one should operate at other conditions where differences would appear. Nevertheless, looking at the center concentrations it can be said that again Y40788 exhibits the most temperature affected response as in the reaction rate case.

An easier case to examine should not show the decrease of reaction rate with increasing temperature, i.e., more predictable/common response, and it should have less diffusion resistance (relative to reaction rate) to allow diverse ethylene concentrations in the center. Thus many trials in the single-pellet reactor with various catalyst pellets (Y41303-41875ⁱⁱ) and reaction conditions (temperatures, pressures and inlet compositions) are made to determine such conditions. Simultaneously, the range of increasing reaction rate with increasing temperature is also investigated via kinetic reactor experiments. Consequently, a set of condition-pellet pairs are foreseen, which were expected to exhibit the desired qualities.

Therefore, the pellets Y42099-42218ⁱⁱⁱ under a pressure of 1.1 bara, temperatures between 20 to 100°C, and a total inlet flowrate of 675 [ml_{rc}/min] with 81% N_2 , 13% C_2H_4 , and 6% H_2 are investigated.

From the table 3.3 it can be observed that the center-chamber ethane values now are not close to zero, and they span a relatively large range of values (between 3.1-13.5 %). Additionally, for this series the temperature range is chosen different from the previous ones, and a finer sampling is made with respect to it. With such an approach, it will be easier to predict the responses of this complicated system.

The reaction rate behaviour with respect to temperature is plotted in fig.3.5 and is now also as desired, i.e., increasing with temperature. The

ⁱⁱFor example, the experiments and results with pellets Y41573-41575, and Y41874-41875 can be found respectively in Bonaventure⁷² and Omaynikova⁷³.

ⁱⁱⁱMore detailed information about the experiments respectively with Y42099-42100 and Y42218 can be found in Marinova⁷⁴ and Bojkova⁷⁵.

Table 3.3: The experimental results for series **SP2**, the **Single Pellet** reactor series **2**. Nine pellets are used for each experiment, the pressure was 1.1 bara and total inlet flowrate was 675 [ml_{rc}/min] with the following composition: 81% N_2 , 13% C_2H_4 , and 6% H_2 . Each experiment is repeated at least once and the average value of these data are shown in the table.

SP2_	Pellet	T [°C]	Exit Composition [%]				Center Composition [%]			
			N_2	C_2H_4	C_2H_6	H_2^*	N_2	C_2H_4	C_2H_6	H_2^*
1		20	79.6	14.0	0.05	6.3	80.2	9.7	4.6	5.4
2		25	79.7	13.7	0.03	6.6	80.1	10.2	3.8	5.8
3		30	79.7	13.4	0.06	6.8	80.7	10.5	3.5	5.2
4		35	79.8	13.6	0.08	6.5	80.3	11.1	3.1	5.4
5	Y42099	40	80.1	13.4	0.11	6.5	81.4	10.0	4.3	4.3
6		45	79.8	13.8	0.08	6.4	80.8	9.5	5.0	4.6
7		50	80.6	13.1	0.21	6.1	82.5	8.8	5.5	3.2
8		55	80.0	13.6	0.00	6.5	80.7	8.8	5.1	5.4
9		60	80.7	13.1	0.12	6.1	82.0	7.4	6.5	4.2
10		65	80.1	13.4	0.02	6.4	80.6	9.4	4.3	5.7
11		20	80.2	13.8	0.07	6.0	80.9	7.3	7.0	4.8
12		25	80.2	13.5	0.09	6.2	80.7	6.2	7.6	5.4
13		30	80.2	13.3	0.03	6.4	80.8	6.9	6.6	5.6
14		35	80.6	13.2	0.15	6.0	81.9	1.2	13.0	3.8
15		40	80.3	13.4	0.11	6.2	80.9	7.9	6.2	5.1
16		45	80.1	13.2	0.06	6.7	81.0	8.6	5.2	5.3
17		50	80.3	13.2	0.13	6.3	81.1	7.9	5.9	5.1
18		55	80.3	13.2	0.12	6.4	81.2	7.6	6.3	4.9
19	Y42100	60	80.0	13.1	0.17	6.7	81.4	6.7	7.5	4.4
20		65	80.6	13.2	0.14	6.0	81.7	5.8	8.2	4.2
21		70	79.9	13.1	0.19	6.7	80.8	5.6	8.6	4.9
22		75	80.0	13.4	0.19	6.4	80.9	4.9	9.4	4.8
23		80	80.3	13.4	0.20	6.2	81.6	3.7	10.6	4.1
24		85	80.2	13.2	0.22	6.3	81.7	1.3	13.1	3.9
25		90	79.5	13.6	0.22	6.8	80.8	1.1	13.6	4.6
26		95	80.6	13.1	0.22	6.1	81.9	1.0	13.2	3.8
27		100	80.4	13.2	0.22	6.2	81.9	1.0	13.3	3.8
28		30	81.2	12.9	0.06	5.9	81.9	3.5	10.0	4.8
29		45	81.2	12.9	0.11	5.8	82.0	1.6	11.9	4.5
30	Y42218	60	81.4	12.7	0.13	6.1	81.8	0.2	13.3	4.6
31		75	81.2	12.7	0.15	6.0	81.9	0.1	13.4	4.8
32		90	81.1	12.7	0.16	6.1	81.8	0.0	13.4	4.8
33		100	81.6	12.6	0.17	5.7	82.8	0.0	13.5	3.8

* The detection of H_2 was not possible with the equipment in use, and thus it is calculated by subtracting the other values from 100. As a result, H_2 values accumulates the errors from others and have the most uncertain values.

error bars in the figure indicate the minimum and the maximum values measured for the corresponding condition. To ensure reliability, some of the measurements are repeated more than once, in some cases reaching up to a total of five measurements. It should be noted that at 35°C the Y42100 did not achieve a steady-state even for a period of ten days and showed some kind of an oscillatory behaviour. Also at 60°C both Y42100 and Y42218 gave results that are out of the general trend, i.e., too low reaction rates with very high dispersion of results. So, these measurements are not taken into consideration. The reason behind this behaviour, whose extensive investigation is out of the scope of this work, is most probably the complicated surface kinetics of this reaction. It is known that this reaction shows oscillations under certain conditions [e.g., see Heese³⁷].

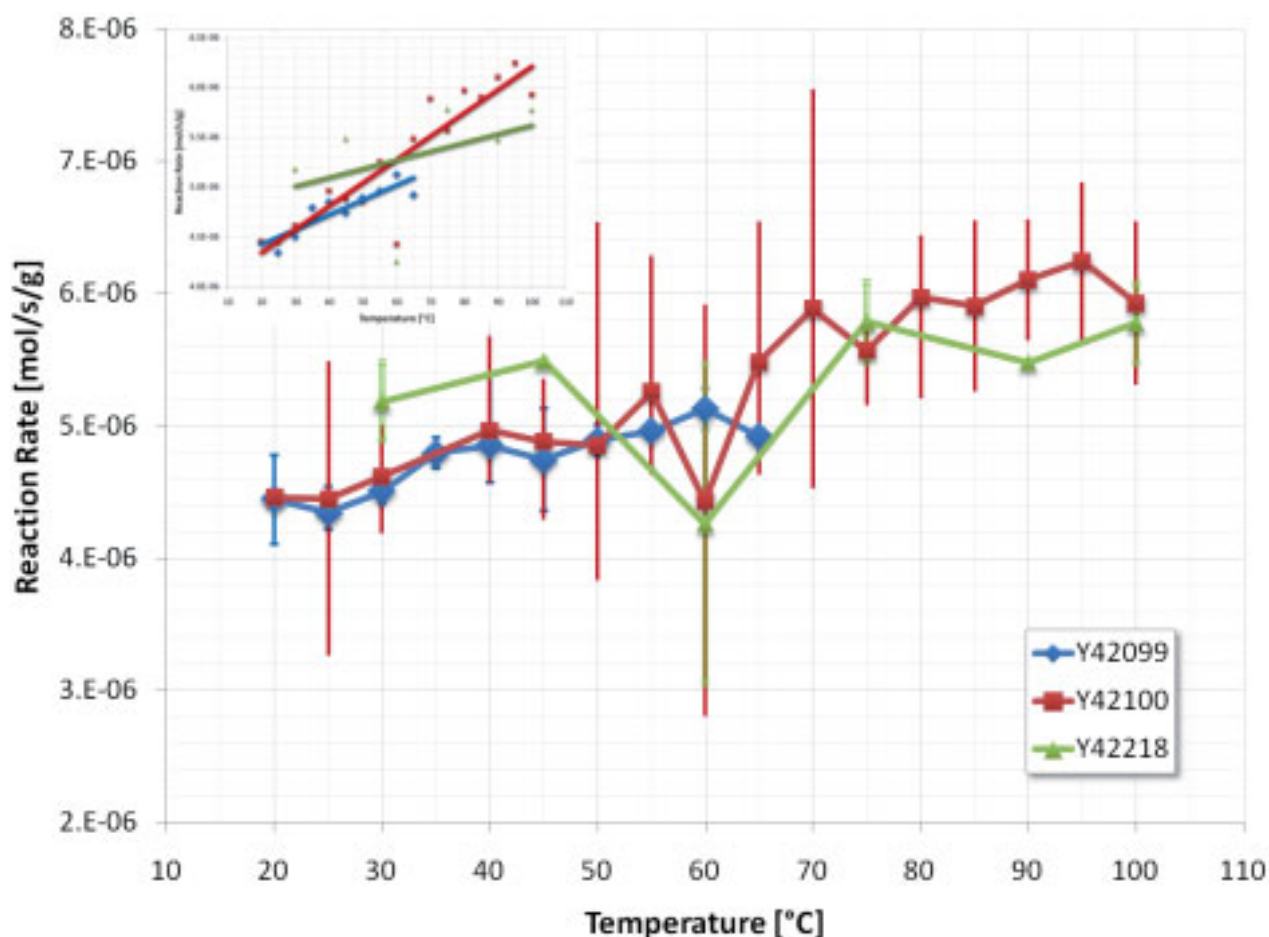


Figure 3.5: Plot of temperature vs reaction rate for experimental series SP2. On the left upper corner the trend of the individual pellets are indicated by linear fits. Error bars indicate the maximum and minimum values measured.

The left-upper corner of the fig.3.5 shows the general trend of the reaction

rate for each pellet. As expected, the reaction rates are nearly linear and show different slopes. The different slopes are again an indication of the effect of the pore structure. As the conditions change, the transport in the pores are affected differently for different pellets. Therefore, the rate of change of the apparent reaction rate varies for different pore structures.

Concerning the optimum pore structure, the same conclusion is reached as in the SP1-case although the general behaviour and the conditions are not similar. An optimum pore structure is operating-condition dependent. For example, at 30°C Y42218, but at 90°C Y42100 gives the higher reaction rate (see fig.3.5), consequently the highest conversion. For this study, it seems that there is no global optimum pore-structure, but local optima depending on the corresponding reaction conditions. And thus the rule of thumb, “the higher surface area, the higher reaction rate” is inappropriate for this case.

The next two figures, fig.3.6 and 3.7 indicating the center content for ethylene and ethane respectively, are like mirror images of each other, although they originate from different measurements. Since ethylene is a reactant and ethane is the product, such a behaviour could be expected. Nevertheless, this good correspondance in the behaviour can just be seen as an indication of the reliability of the measurements.

Turbo-Reactor and Kinetics

As already known from the UCKRON test problem^{iv}, the fitting of kinetic model equations to the experimental data does not necessarily lead to the actual reaction mechanism and various other models/paths can also be found to represent the data satisfactorily. It has been also noted that the hydrogenation of ethylene is a deceptively simple reaction which possesses an extremely rich and complicated chemistry²⁷, and, therefore, complicate kinetic models will be required to represent its versatile behaviour. On the other hand, elucidating the reaction mechanism of ethylene hydrogenation or determining its actual reaction mechanism are not in the scope of this thesis. The actual purpose of the work presented here is to find a satisfactory mathematical

^{iv}See for example p.219 in Berty⁷⁶.

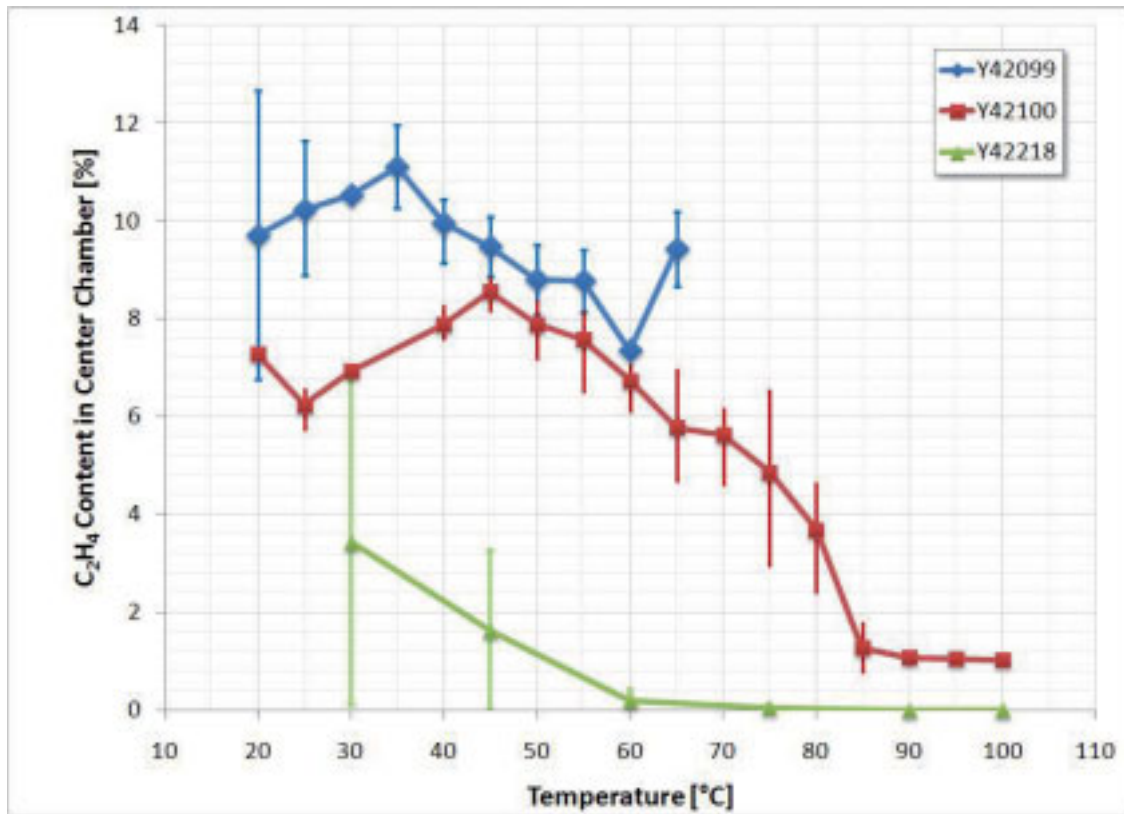


Figure 3.6: Ethylene content in the center chamber for SP2.

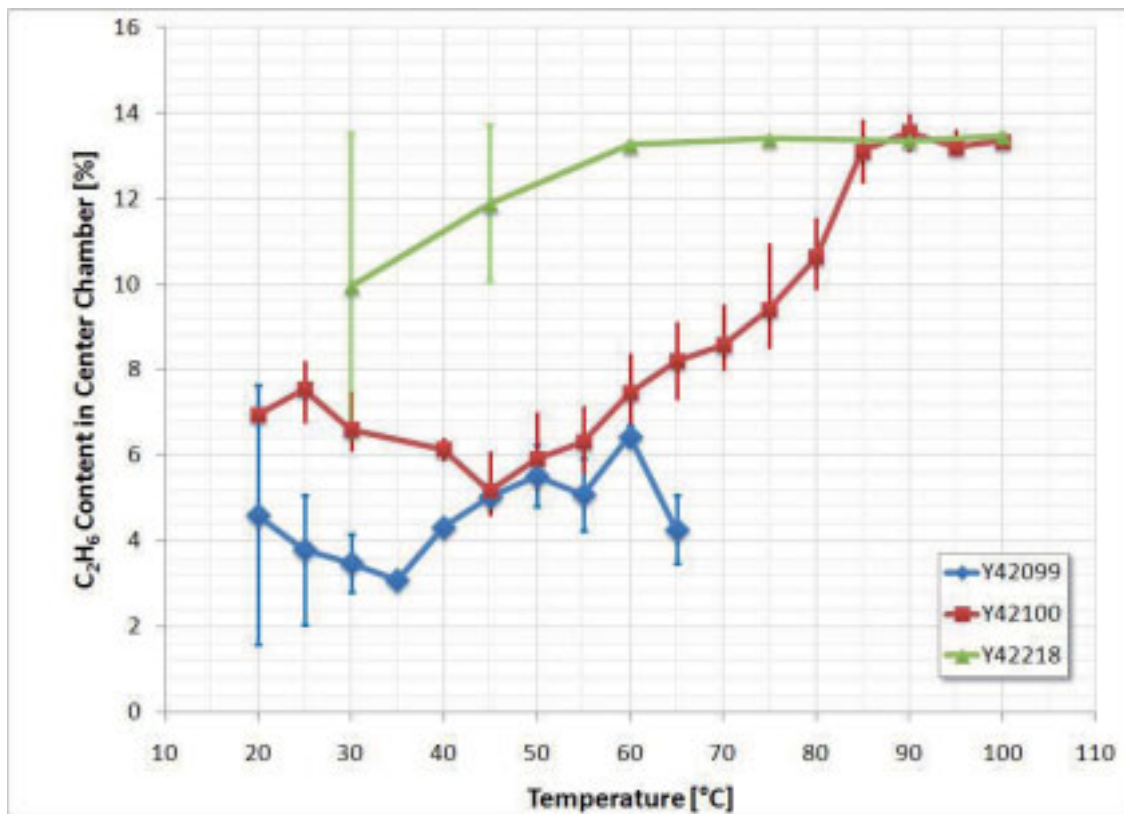


Figure 3.7: Ethane content in the center chamber for SP2.

equation based on kinetic experiments that represents the reaction rate in the region of interest.

Actually, the versatile nature of the reaction has also been observed during the work done throughout this study. Some of these, interest arousing properties, can be summarized as: decreasing reaction rate with increasing temperature^v, oscillatory behaviour of reaction rate^{vi}, and the strong dependence of reaction orders to the reactant concentrations and temperature. Anyhow, this behaviour can be avoided by simply changing the operating conditions; most of the time it was sufficient to change the relative ratio of ethylene to hydrogen. And this strategy was followed to avoid any complications that could arouse from such phenomena.

A note can be made here concerning a future study of mechanism of ethylene hydrogenation or of another reaction in general. In their interesting and critical paper, Lynggaard *et al.*⁷⁷ emphasize that *“Abrupt changes in slope in the Arrhenius plot are traditionally interpreted as the signature of a change in rate limiting step or the onset of diffusion phenomena. One of the main results of our analysis is that simple mechanisms with realistic parameters display such signatures without a change in rate limiting step and in the absence of transport phenomena.”*. Eventually, it should be possible to enclose such versatile behaviour even by utilizing simple mechanisms.

The most relevant series of kinetic experiments can be numbered as *TR1*, in which the catalysts with a loading of 0.3, and *TR2*, in which loading 0.001 wt% Pd, were used. The *TR1* and *TR2* kinetic experiments were conducted in different reactors, respectively in the original and in the new turbo-reactors (see p.28 for the reactors). Flow characteristics and optimum operating conditions studies for the original turbo-reactor were already available⁶⁰, and a preliminary study for the new turbo-reactor was conducted at the institute

^vSee Bonaventure⁷². This phenomena is known to occur for heterogeneously catalyzed reactions, e.g., in the oxidation of CO, due to the effect of the adsorption constants and surface coverage values on the reaction rate. It is not a violation of the Arrhenius' Law, not the reaction rate constant but the reaction rate decreases with increasing temperature.

^{vi}See Marinova⁷⁴. In this particular case what is meant by the oscillatory behaviour is the continual change (increase-decrease) of concentration. But the reaction did not come to a steady-state even if the system was allowed to proceed for more than two hundred hours. The oscillations seemed to dampen and to have a converging behaviour nevertheless.

accompanying this work⁷⁸. One of the basic findings of these studies is that a min. of 1500 (original-reactor) and 3000 *rpm* (new-reactor) is required to have a good mixing inside the reactors^{vii}.

Various mathematical expressions are used for fitting the collected data, see table 3.4. All models, in accordance with the literature, are based on Langmuir-Hinshelwood type approaches and the simple power-law (model 1), except the last one, which is an Eley-Rideal type model (model 11).

A pressure of 3 *bar*, temperatures of 30, 60 and 90 °C, 0.0213 *g* of catalyst^{viii} and an inlet flow rate of 2000 *ml/min_{rc}* are used in series *TR1*. Fifteen experiments are done for each temperature and the best fit to the data was the *model 4*.

The fitted parameters for *model 4* can be seen in table 3.5. There are some discrepancies to be noticed in this fit; the adsorption constant values increase with increasing temperature, the reaction rate constant decreases with increasing temperature and the adsorption constant for ethane has a negative value, which are all conflicting the theory. Therefore, it can be said that the mathematical equation describes the behaviour of the reaction, but none of the parameters represent what they were supposed to represent; they are not adsorption constants and a reaction rate constant.

A fit to the simple power law (*model 1*) delivers temperature dependent reaction orders with sum of squares of errors in the range of 10^{-6} . The respective values of β and α are 0.31, 0.4, 0.88 and 0.88, 0.87, 0.45 for 30, 60 and 90 °C. The Arrhenius plot is nearly perfectly linear and delivers an activation energy of 5.2 *kcal/mol*.

One also gets a good fit using *model 6*. The fit values, along with the sum of squares of the errors, can be found in table 3.6. In this case, the fitted parameter values behave according to the theory. The k_{rxn} values used in the Arrhenius plot gives an activation energy of ca. 6 *kcal/mol*.

In the series *TR2*, a pressure of 1.1 *bar*, temperatures of 30, 50 and 100

^{vii}These values actually depend also on the inlet flow-rate, and the particle size used.

^{viii}The pellets of Y41573 (0.3 wt% loading) is grinded and the fraction $0.5 < \bar{x} < 0.8$ mm was used in the experiments. The original turbo-reactor is utilized with a 1500 rpm rotation speed.

Table 3.4: Various kinetic models fitted to the data from the turbo-reactor.

Label	Kinetic Model Equations
1	$R_{rxn} = k_{rxn} \cdot C_E^\alpha \cdot C_H^\beta$
2	$R_{rxn} = \frac{k_{rxn} \cdot K_E \cdot C_E \cdot K_H \cdot C_H}{1 + K_E \cdot C_E + \sqrt{K_H \cdot C_H}}$
3	$R_{rxn} = \frac{k_{rxn} \cdot K_E \cdot C_E \cdot K_H \cdot C_H}{(1 + K_E \cdot C_E)(1 + K_H \cdot C_H)}$
4	$R_{rxn} = \frac{k_{rxn} \cdot K_E \cdot C_E \cdot K_H \cdot C_H}{(1 + K_E \cdot C_E + \sqrt{K_H \cdot C_H} + K_A \cdot C_A)^3}$
5	$R_{rxn} = \frac{k_{rxn} \cdot K_E \cdot C_E \cdot K_H \cdot C_H}{(1 + K_E \cdot C_E)^{1.25}(1 + K_H \cdot C_H)}$
6	$R_{rxn} = \frac{k_{rxn} \cdot K_E \cdot C_E \cdot \sqrt{K_H \cdot C_H}}{1 + K_E \cdot C_E + \sqrt{K_H \cdot C_H}}$
7	$R_{rxn} = \frac{k_{rxn} \cdot K_E \cdot C_E \cdot \sqrt{K_H \cdot C_H}}{(1 + K_E \cdot C_E + \sqrt{K_H \cdot C_H})^2}$
8	$R_{rxn} = \frac{k_{rxn} \cdot K_E \cdot C_E \cdot K_H \cdot C_H}{(1 + K_E \cdot C_E)(1 + \sqrt{K_H \cdot C_H})^2}$
9	$R_{rxn} = \frac{k_{rxn} \cdot K_E \cdot C_E \cdot \sqrt{K_H \cdot C_H}}{(1 + K_E \cdot C_E)(1 + \sqrt{K_H \cdot C_H})}$
10	$R_{rxn} = \frac{k_{rxn} \cdot K_E \cdot C_E \cdot K_H \cdot C_H}{(1 + K_E \cdot C_E + \sqrt{K_H \cdot C_H})^3}$
11	$R_{rxn} = \frac{k_{rxn} \cdot K_E \cdot C_E \cdot C_H}{1 + K_E \cdot C_E}$

Table 3.5: Model 4 fitted parameter values to *TR1* experiments.

Parameter	30°C	60°C	90°C	Unit
k_{rxn}	1.68	1.36	1.19	$[10^{-2} \cdot \frac{mol}{g_{cat} \cdot s}]$
K_{H_2}	0.836	1.18	1.62	$[\frac{m^3}{mol}]$
$K_{C_2H_4}$	0.103	0.136	0.167	$[\frac{m^3}{mol}]$
$K_{C_2H_6}$	-0.231	-0.342	-0.456	$[\frac{m^3}{mol}]$
sum of squares	$3.29 \cdot 10^{-8}$	$4.10 \cdot 10^{-8}$	$3.36 \cdot 10^{-8}$, R_{rxn} values $\cong 10^{-3}$

Table 3.6: Model 6 fitted parameter values to *TR1* experiments.

Parameter	30°C	60°C	90°C	Unit
k_{rxn}	1.07	2.61	5.51	$[10^{-2} \cdot \frac{mol}{g_{cat} \cdot s}]$
K_{H_2}	12.7	1.85	0.478	$[10^{-2} \cdot \frac{m^3}{mol}]$
$K_{C_2H_4}$	3.60	2.45	1.88	$[10^{-2} \cdot \frac{m^3}{mol}]$
sum of squares	$1.31 \cdot 10^{-6}$	$1.04 \cdot 10^{-6}$	$1.19 \cdot 10^{-6}$, R_{rxn} values $\cong 10^{-3}$

°C, 0.9336g^{ix} of catalyst and an inlet flow rate of 200 ml/min_{rc} are used.

For this case, the *model 1* was a fair fit with again the reaction orders being temperature dependent, but the reaction rate constant is decreasing with increasing temperature. The α and β values were, respectively, -0.768, -0.140, -0.0671 and 0.841, 1.08, 2.48 (corresponding to 30,50,100°C). These values are in accordance with the findings in the literature; it is common to have slightly negative values for ethylene and a value around one for hydrogen. But the behaviour of k_{rxn} with respect to temperature, indicates that a much more complex phenomena are occurring.

^{ix}The pellets of Y42099 (0.001 wt% loading) is grinded and the fraction $0.5 < \bar{x} < 0.8$ mm was used in the experiments. The new turbo-reactor is utilized with a 3000 rpm rotation speed.

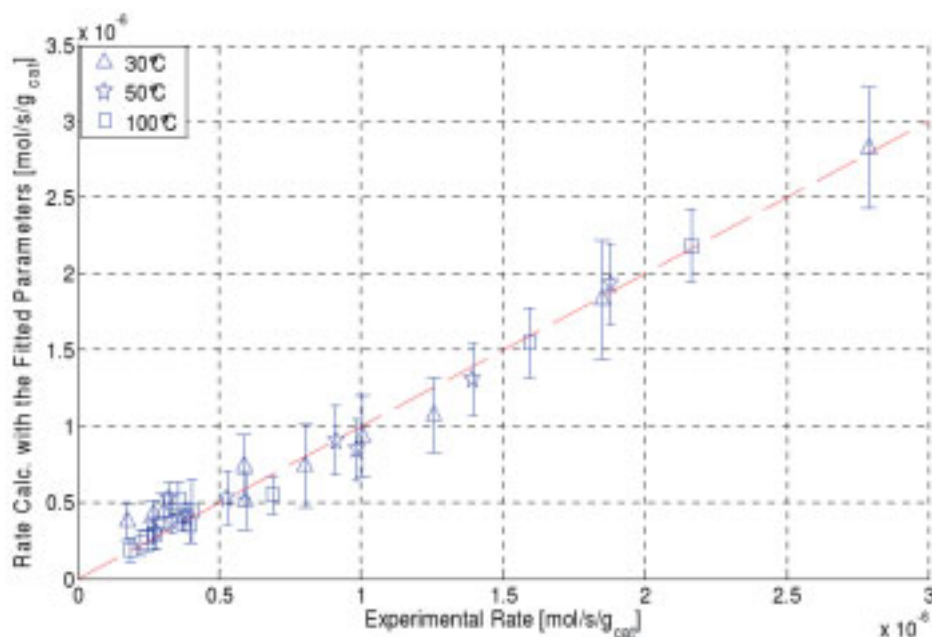


Figure 3.8: Fitting of *model 4* to experimental data (*TR2*) with 95% confidence interval.

The best fit, on the other hand, was achieved again for *model 4*; the parameter values found can be seen in table 3.7, and the correspondance between calculated and experimental reaction rates are plotted in fig.3.8. But this time, contrary to *TR1* case, the k_{rxn} and adsorption constant values for ethylene and hydrogen behave according to the theory. Only the ethane adsorption coefficient remains a negative value. The Arrhenius' plot delivers a good fit with an activation energy of 3.38 kcal/mol.^x The adsorption constants for ethylene and hydrogen fit to the *van't Hoff equation*^{xi} and heat of adsorption values of -4.73 and -4.38 kcal/mol can be extracted from this fit. Here, the $K_{C_2H_6}$ should not be treated anymore as an adsorption coefficient, but as a parameter defining the relationship between the ethane concentration and the reaction rate.

It can be concluded that since *model 4* fits best to the experimental data for very different conditions, it is the best model to describe the ethylene hydrogenation under the conditions investigated. The simple power law (*model*

^xThe coefficient of determination was $R^2 = 0.967$ and a value of $2.262 \cdot 10^{-3} \frac{m^3}{g_{cat} \cdot s}$ for k_0 (preexponential factor) can be extracted from the intercept.

^{xi}The *van't Hoff equation* is $\ln(K_{ads}) = \frac{\Delta S}{R_{gas}} - \frac{\Delta H_{ads}}{R_{gas}} \cdot \frac{1}{T}$ and a plot of $1/T$ vs. $\ln(K_{ads})$ delivers a slope of $-\frac{\Delta H_{ads}}{R_{gas}}$ and an intercept of $\frac{\Delta S}{R_{gas}}$.

Table 3.7: Model 4 fitted parameter values to *TR2* experiments.

Parameter	30°C	50°C	100°C	Unit
k_{rxn}	0.892	1.05	2.46	$[10^{-5} \cdot \frac{mol}{g_{cat} \cdot s}]$
K_{H_2}	0.461	0.190	0.0973	$[\frac{m^3}{mol}]$
$K_{C_2H_4}$	8.64	6.13	2.25	$[10^{-2} \cdot \frac{m^3}{mol}]$
$K_{C_2H_6}$	-2.18	-2.48	-1.60	$[\frac{m^3}{mol}]$

1) is practically hard to use since its constants depend on the experimental conditions. So for every new, say temperature, one needs to make experiments and determine these constants. On the other hand, that is not the case for *model 4*, even for the case it results in conflict with the theory, the parameters seem to fit to the theoretical equation with unexpected/theoretically impossible values. And thus using these determined parameters, one can estimate the reaction rate for different conditions.

Any further investigation concerning kinetic fit and/or reaction mechanism of this reaction should also examine this interesting relation between the actual reaction rate and the model; either modifying this model or try to elucidate the reason behind this accordance of the model with the experimental results (even sometimes the constants turn out to be unrealistic).

3.2 Modeling

This section starts with the geometrical modeling of pores, and then compares two different geometrical models; a simpler bi-disperse parallel pore model with a 3-D network model. The results indicate that the complex model is surprisingly not better than the simpler one. Both models determine one or two components' concentrations correct but result in larger errors for the rest. This indicates that one should concentrate not on the geometrical modeling but on the governing transport equations for this case. Following the conclu-

sions from the previous 3-D modeling work, a focus on surface diffusion and its modelling under Knudsen flow conditions has been given. Through mass balances, it is shown that an equilibrium between gas phase and surface is theoretically impossible. It is also reminded that the traditional modeling of Knudsen flow in chemical engineering applications has limited validity, and a more precise approach should be utilized. An alternative modeling of Knudsen flow with cosine-law of reflection from surfaces has been introduced. Additionally, the concept of outer-surface area, which is necessary to define the boundary conditions for surface flow, is introduced. Consequently, a novel modeling approach has been developed to incorporate all these points and used along with finite-difference approach. Sample systems are simulated and are found to be in accordance with the literature proving the validity of the approach. Further simulations are then used to show the diversity in the behaviour of such systems. Results from sample systems under simultaneous Knudsen and surface flow: for different pore lengths, for concentration dependent surface diffusion coefficients, for multi-component surface diffusion and reaction are presented. In general, it can be said that when there is considerable surface flow, the common approach for modeling is not representative, and the system exhibits various deviations from the expected behaviour. Additionally, the results of these simulations are used to back-calculate the surface diffusion coefficient by using the typical assumptions, such as adsorption-desorption equilibrium. The back-calculated surface diffusion coefficients are found to exhibit concentration dependence, although a constant value was used, and under considerable surface flow rate the errors in back-calculation are found to be more pronounced. Although, it is not possible to derive general conclusions from these sample results, the findings rise questions and doubts about traditional modeling and surface diffusion parameters achieved thereby. Nevertheless, extensive research is necessary to be able to fully understand the behaviour of these diverse systems and the extent of error associated with the utilization of common/traditional assumptions.

3.2.1 Modeling of Many Pores

Geometrical modeling of the pore structure is the first step of modeling the transport and reaction in porous structures.

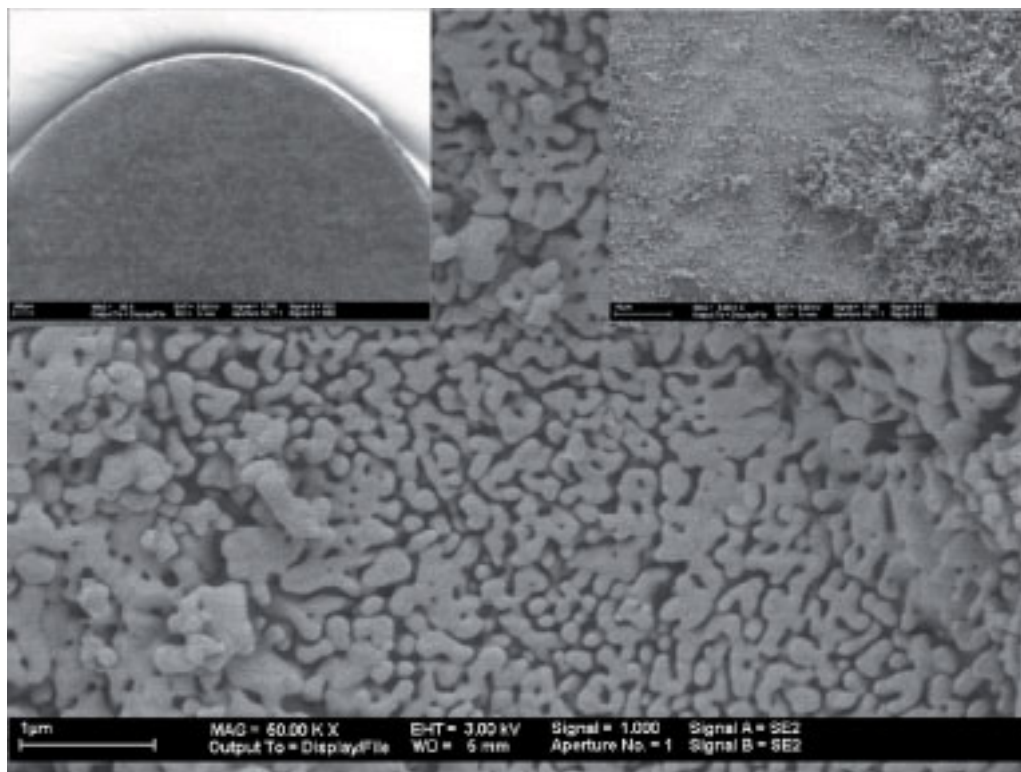


Figure 3.9: SEM (Scanning Electron Microscopy) images of a catalyst surface at different magnifications. The surface of a cylindrical-pellet used (4.5mm in diameter), with 90 (left-corner), 5000 (right-corner) and 50000 times (main) magnification, is seen in the figure.

In reality the catalyst pore structure is very complex (see fig.3.9); the cross-section is somewhat arbitrary in shape and changing along the pore length, the pores are not straight, connections with other pores are geometrically irregular and thus the beginning and the end of a pore may not be obvious most of the time, the spatial distribution of pores does not follow a particular framework, etc. So in practice, simplifications are commonly used. For example, cylindrical pores with constant cross-section, fixed spatial distribution patterns, etc.

Probably, the simplest model one can think of is the parallel pore model. For mono-disperse structures, the model is simply similar independent parallel pores with exactly the same properties. So modeling of a single pore

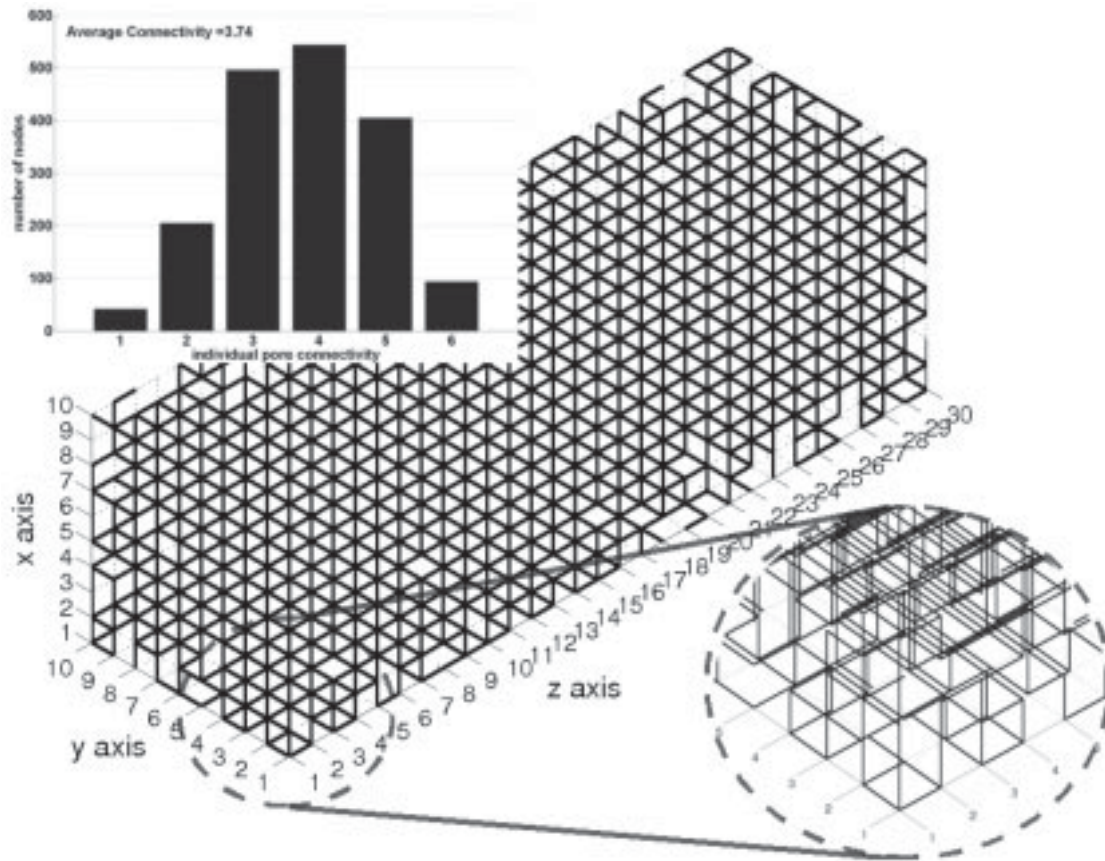


Figure 3.10: A 3-D pore network built and the belonging pore connectivity for it. A network $10 \times 10 \times 30$ nodes is shown with an average connectivity of 3.74. Six nodes are found to have no connection to any pore, i.e., zero connectivity, other connectivity values are given in the histogram.

is enough to fully define the system. For bi-disperse systems, one can also build a similar structure by assuming that the larger pores build the parallel pore structure and the smaller pores act as connections between them. On the other hand, one of the geometrically most complex structure would be a 3-D network of pores. Such a network is also built in this work. A Matlab program using an average connectivity and a fixed pore length value, but allowing the individual nodes to have different connectivities and the pores have different radii is written for that purpose. An example of a built 3-D pore network is shown in fig.3.10.

In general, one should determine what level of complexity is necessary to achieve the desired level of precision. That means one needs to answer the following question: “Is a more complex pore structure always a better modeling of the system at hand?”.

3.2.2 Comparison of Two Geometrical Models

A three dimensional pore network model was already available at the department⁷⁰. Another model, a simple parallel pore model for bi-modal systems, is built⁷⁹ and used to simulate a sample system from this previous work⁷⁰. The model and the results can be summarized as follows (more details about solution procedure and modeling can be found in Günbulut⁷⁹).

The parallel pore model, which is very simple compared to a three dimensional pore network model, is used to model a bi-modal pore structure using hexagonal unit cells. The larger pore is placed at the center of the unit cell extending axially through the hexagonal prism. The smaller pores cross the larger one perpendicularly, and extend along the diagonals and dividing chords of the hexagon, adding up to 12 smaller pores per unit cell in total (see figure 3.11). Such a configuration was chosen since it was able to reach the porosity of the real system.

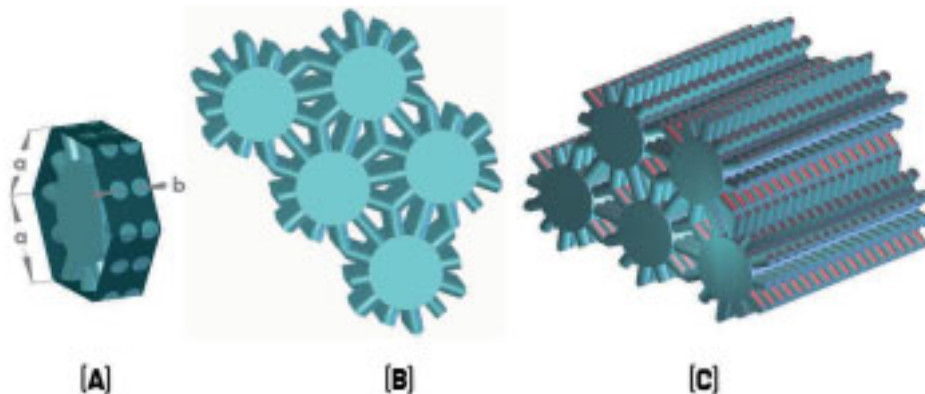


Figure 3.11: Hexagonal unit cell and graphical representations of the parallel pore models using it. [A] hexagonal unit cell with characteristic dimensions a and b , [B] face view of the parallel pores, [C] isometric view of the parallel pores

The characteristic lengths in figure 3.11, side length a and depth b , can be calculated from the pore structure analysis experiment results, e.g., mercury-porosimetry or nitrogen-sorption experiments. The two values can be calculated as follows:

$$a = \sqrt{\frac{2\pi \cdot r_{p,l}^2}{3\sqrt{3} \cdot \bar{V}_{pore,l} \cdot \rho_{bulk}}} \quad (3.1)$$

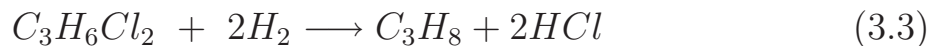
$$b = \frac{4\pi \cdot r_{p,s}^2}{\sqrt{3} \cdot a^2 \cdot \bar{V}_{pore,s} \cdot \rho_{bulk}} \cdot \left[\left(\frac{\sqrt{3}}{2} + 1 \right) \cdot a - 2 \cdot r_{p,l} \right] \quad (3.2)$$

An experiment with catalyst Y34315 at 433K and 3.5bar with a hydrogen to dichloropropane mole ratio of 10 (see Rieckmann⁷⁰) was chosen to be the sample system to investigate. The catalyst Y34315 has a total length of 2.8[mm], and it has two different pore sizes, i.e., bi-disperse pore structure (see table 3.8). This structure leads to characteristic lengths of $a = 4.731[nm]$ and $b = 3.252[nm]$.

Table 3.8: Pore size distribution data for catalyst Y34315.

Pore type	Pore size	Pore volume
	r_p	\bar{V}_{pore}
	[nm]	[$m^3 \cdot kg^{-1}$]
larger, l	3.2	0.4×10^{-3}
smaller, s	2	0.07×10^{-3}
total		0.47×10^{-3}

The probe reaction for the experiment was the hydrogenated dechlorination of 1,2-dichloropropane (DCP)



and it was found to follow the following kinetic expression under such conditions:

$$R_{rxn} = k_0 \cdot \exp\left(\frac{-E_a}{RT}\right) \cdot \exp\left(\frac{-t}{\tau}\right) \cdot \frac{K_{H_2} \cdot P_{H_2} \cdot K_{DCP} \cdot P_{DCP}}{(1 + K_{H_2} \cdot P_{H_2} + K_{DCP} \cdot P_{DCP})} \quad (3.4)$$

The parameters used in the the above equation is tabulated in table 3.9.

In modeling, the pressure inside the pore is also allowed to change with Hagen-Poiseuille correlation. This also allows to check for theoretical change of pressure inside such a pore. The dusty-gas model approach is used to model

Table 3.9: Parameter values for the kinetic expression in eq. 3.4

Parameter	Value	in units of
k_0	7.0114×10^8	$[mol \cdot kg^{-1} \cdot s^{-1}]$
E_A	92108	$[J \cdot mol^{-1}]$
τ	10.44	$[days]$
K_{H_2}	1.528×10^{-6}	$[Pa^{-1}]$
K_{DCP}	1.099×10^{-5}	$[Pa^{-1}]$

the diffusion inside pores. The resulting dimensionless equation system can be summarized as follows:

$$\frac{d}{dz}[N] = L_t \cdot [R_{rxn}] \quad (3.5)$$

$$\frac{d}{dz}[X] = -L_t \cdot \frac{1}{C_{mix}} \cdot [B] \cdot ([N] - A \cdot N_1 \cdot [X]) \quad (3.6)$$

$$\frac{dP}{dz} = -L_t \cdot \frac{8\mu}{r_t^2} \cdot \frac{RT}{P} \cdot A \cdot N_1 \quad (3.7)$$

The Matlab function *bvp4c* is used for the solution of the boundary value problem at hand. Since the concentrations of the species do not change steeply throughout large pores, the smaller pores close to one other face practically identical conditions. Therefore, such small pores can be grouped together and connected to a single node on the larger pore. This greatly reduces the number of equations to be solved, thus the computational work. The results given below (see table 3.10) are found by assuming 120 nodes between small and large pores.

The results indicate that there is virtually no pressure drop along the pellet length, which had been also experimentally observed. The mole percentage values at the end of the pellet, i.e., the center chamber for the single-pellet reactor, are given in table 3.10 along with the experimental results and results from the more complex model (i.e., three dimensional pore network model).

Table 3.10: Mole percentages at the center of the pellet collected from different sources.

Species	Parallel Pore Model ⁷⁹	Experimental Results ⁷⁰	Three Dimensional Network Model ⁷⁰
DCP	6.51	6.767	7.64
H ₂	89.94	—	89.92
Propane	1.54	0.69	1.10
HCl	2.01	—	1.34

As seen in table 3.10, the results delivered by the simple parallel pore model are not much different from the much more complex model, i.e., the three dimensional network model. Moreover, for the DCP mole percentage the parallel pore model delivers a much more accurate value if one takes the experimental result as the correct value. But for the other component, both models deliver very big errors. These findings lead to two conclusions; first the simple pore model is not worse than the much more complex approach, on the contrary in this case it estimates the DCP mole percentage better, and second both methods deliver big errors for propane mole fractions. Most probably both methods will deliver good estimates for the hydrogen mole percentage value, since its concentration is very high and thus nearly constant. But this also leads to the expectation that the HCl concentration will be wrongly estimated by both of the methods (if one takes 89.93 (average of both methods) for the hydrogen mole percentage, the value for HCl must turn out to be 2.61 since a total of 100% must be reached). This behaviour suggests one of the following problems: badly estimated parameters (e.g. kinetic parameters, diffusion constants, etc.), a problem in experiments or a problem in modeling (inappropriate models, invalid assumptions). The estimation of diffusion coefficients are well developed, the kinetic parameters had been estimated using a large amount of experimental data and the reproducibility of the single-pellet reactor experiments had been conducted too. Besides, non-isothermal or non-isobaric conditions can be ruled out: it has been both experimentally and theoretically shown that the system is isobaric and a temperature difference had not been experimentally detected. As

a result of these points, one is led into the idea of a deficient model. Rieckmann⁷⁰ notes that although at lower pressures the results are in accordance with experiments at higher pressures the error increases, and she notes that the reason behind such a behaviour may be due to surface diffusion, which is not taken into account in the model above. Therefore, this point will be investigated subsequently. Rieckmann⁷⁰ could find coincidence between her 3-D model and measurements by taking surface diffusion into account.

3.2.3 Notes on Surface Diffusion

As noted at the end of section 3.2.2 surface diffusion can be one of the important features in diffusion through porous structures under specific conditions. It is actually known for a long time that surface diffusion can contribute significantly to the total transport in a porous medium^{80,81}. This contribution is more pronounced for small pore diameters, at lower pressures, that is, in the region where Knudsen diffusion prevails⁸². Macroscopically, the rate of surface diffusion may be measured using the steady-state permeability method or by using a diffusion (Wicke-Kallenbach) cell^{81,83,84}.

For example, in a diffusion cell, the surface diffusion flux can be calculated as follows²³: First, the flux of a gas, which is expected not to be adsorbed, is measured. The gas often employed is helium. Then, expecting that non-surface diffusion will occur by the Knudsen mechanism, the expected flux for the test gas, A , is calculated from Graham's law^{xii}:

$$J_A(\textit{nonsurface}) = -J_{He} \cdot \sqrt{\frac{M_{wHe}}{M_{wA}}} \quad (3.8)$$

The difference between the experimental measurement and the nonsurface estimate is the surface diffusion flux:

$$J_A(\textit{surface}) = J_A(\textit{experimental}) - J_A(\textit{nonsurface}) \quad (3.9)$$

^{xii}In general, Graham's law for an n component system reads as: $\sum_{i=1}^n (J_i \cdot \sqrt{M_{wi}}) = 0$

Typically, the flux inferred for the surface diffusion is less than half of that total flux measured experimentally²³.

The determination of the surface diffusion coefficient from the surface flux requires the estimation of the surface driving force, that is, the corresponding concentration gradient. Commonly for this purpose, an adsorption isotherm (Henry's Law, Langmuir adsorption isotherm, etc.) is chosen, and to facilitate the corresponding calculations, it is assumed that the adsorption-desorption equilibrium has been achieved. In some cases explicitly, often also implicitly, equilibrium assumption is commonly used in modeling of transport phenomena in porous media^{16,22,80,82,83,85-90}, where surface diffusion is assumed to take place. As a consequence, the surface coverage and the surface concentration gradient are straightforwardly determined based on the adsorption equilibrium equation.

Although at first sight it seems reasonable, the equilibrium assumption is inappropriate and creates a misconception in modeling. An equilibrium between the gas phase and the surface allows no mass interchange between the two phases and sets the surface flow value to zero. This contradicts the existence of the surface diffusion. A publication concerning this point and also the following justification has already been made by Argonul *et al.*⁹¹.

A (steady-state) mass balance for each flow separately helps to reveal that the equilibrium assumption contradicts the existence of surface flow. The mass transport streams and the control volumes are illustrated in figure 3.12.

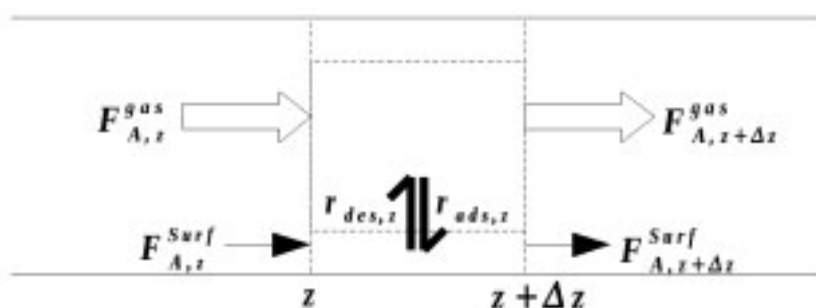


Figure 3.12: Differential control volumes in the pore and various mass flows related.

Mass balance for the gas phase flow has to be made around the core

control volume:

$$F_{A,z}^{gas} - F_{A,z+\Delta z}^{gas} = (r_{ads,z} - r_{des,z}) \cdot 2\pi r_{pore} \cdot \Delta z \quad (3.10)$$

where F is the flow rate [$mol \cdot s^{-1}$], r_{pore} is the pore radius [m], and r_{ads} and r_{des} are, respectively, the adsorption and desorption rates [$mol \cdot m^{-2} \cdot s^{-1}$].

Whereas, the mass balance for the surface flow shall be expressed around the annular control volume:

$$F_{A,z}^{Surf} - F_{A,z+\Delta z}^{Surf} = (r_{des,z} - r_{ads,z}) \cdot 2\pi r_{pore} \cdot \Delta z \quad (3.11)$$

By rearranging eq. 3.10 and 3.11, and knowing that for an infinitesimally small Δz , the derivative $dF_{A,z}/dz$ will replace the difference $(F_{A,z+\Delta z} - F_{A,z})/\Delta z$, it follows that:

$$(r_{des,z} - r_{ads,z}) \cdot 2\pi r_{pore} = \frac{dF_{A,z}^{Surf}}{dz} = -\frac{dF_{A,z}^{gas}}{dz} \quad (3.12)$$

Furthermore, the equilibrium assumption implies that the rates of adsorption and desorption are equal, thus the term on the left-hand side of eq.3.12 becomes zero:

$$(r_{des,z} - r_{ads,z}) = 0 \quad (3.13)$$

Consequently, through eq.3.12 and 3.13, the first derivatives of the gas phase and the surface flows become zero as well:

$$\frac{dF_{A,z}^{Surf}}{dz} = \frac{dF_{A,z}^{gas}}{dz} = 0 \quad (3.14)$$

This leads to constant gas phase and surface flows for the entire length of the pore:

$$F_{A,0}^{Surf} = F_{A,z}^{Surf} = F_{A,L}^{Surf} = constant \quad (3.15)$$

$$F_{A,0}^{gas} = F_{A,z}^{gas} = F_{A,L}^{gas} = constant \quad (3.16)$$

A more detailed drawing of the porous structure model and flow through

a single pore is given in figure 3.13. An incoming surface flow into the pore originating from the left outer-surface of the porous structure can be seen in the figure. This is due to the adsorption and desorption on this facial surface. Owing to mass balance on that surface, this surface flow, i.e. $F_{A,0}^{Surf}$, has to be equal to the difference between the corresponding adsorption and desorption rates on the outer-surface area per pore^{xiii}, A_{pp}^{outer} :

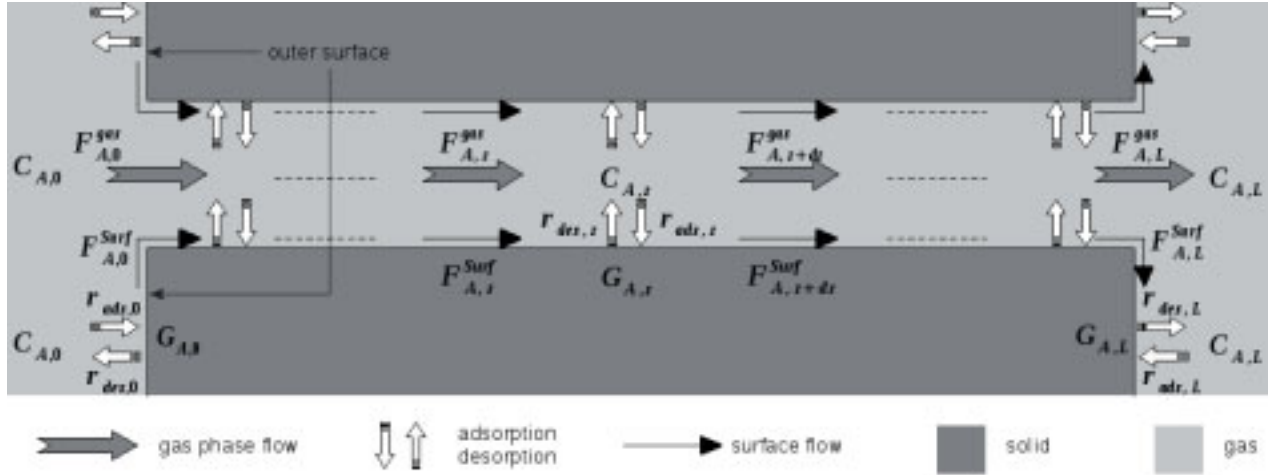


Figure 3.13: Schematic drawing of surface flow and gas phase flow with adsorption and desorption rates in a single pore having outer-surfaces at both ends.

$$(r_{ads,0} - r_{des,0}) \cdot A_{pp}^{outer} = F_{A,0}^{Surf} \quad (3.17)$$

For the above derivation, it was assumed that the surface concentration on the corresponding outer-surface was constant^{xiv}.

Combination of equation 3.17 and the equilibrium assumption sets the surface flow at the entrance of the pore to zero.

$$(r_{ads,0} - r_{des,0}) = 0 = F_{A,0}^{Surf} \quad (3.18)$$

^{xiii}The outer-surface area per pore can be calculated by making use of the porosity, ε . The ratio of solid area (outer-surface area) to the free cross-sectional area is $(1 - \varepsilon)/\varepsilon$. The outer-surface area per pore can then be calculated from the multiplication of this ratio with the cross-sectional area of a pore: $A_{pp}^{outer} = \pi r_{pore}^2 \cdot \frac{1 - \varepsilon}{\varepsilon}$

^{xiv}It may be worth noting that if a definite geometrical shape, e.g., circle, could be assigned to the outer-surface area per pore, a concentration gradient on the face could be calculated and the surface flow at the entrance of the pore could be calculated accordingly. Consequently, the constant outer-surface concentration assumption could be omitted. But, this assumption does not have an effect on the final conclusion.

From equations 3.16 and 3.18, it follows that the surface flow has to be zero throughout the pore. Consequently, the only way of transport will be the gas phase flow.

$$F_A^{gas} = F_A^{total} \text{ and } F_A^{Surf} = 0 \quad (3.19)$$

This result is inconsistent with the statement claiming the existence of the surface flow, i.e., the starting point, and it is a result of the utilization of the adsorption-desorption equilibrium assumption.

For a flow system, there has to exist a source and a sink, between which the material is transported by means of different transport mechanisms. For the system in question, although the source and the sink are not given explicitly, it is commonly taken for granted that there are two reservoirs on the left and on the right of the porous medium (or the pore). Based on the flow of species A , the left and right reservoirs become the source and the sink, respectively. The two transport mechanisms, gas-phase and surface flows, serve as connections between these reservoirs. The connection through the gas-phase flow is direct, the molecules directly flow from one reservoir to the other via this mechanism. On the other hand the surface flow connects the two reservoirs indirectly. For this connection, first the molecules have to get onto the surface (adsorption), then they have to be transported (surface diffusion) and finally they have to be released (desorption). The adsorption equilibrium assumption hinders this transport mechanism by preventing the first and the last steps to occur. Thus physically under equilibrium conditions, it is not possible that a surface flow appears (see equation 3.19). On the other hand, a surface concentration gradient and consequently a surface flow can be calculated through the same assumption by the utilization of the gas-phase concentrations and equilibrium constants. These two contradictory findings demonstrate the inconsistency and the resulting misconception in modeling surface diffusion with adsorption equilibrium. Throughout adsorption equilibrium and surface flow cannot exist simultaneously, although a finite value for the surface flow can be calculated. Thus equilibrium assumption becomes inappropriate for such systems.

The rates of adsorption and desorption can still be expected to be close to each other. If they are really much higher than the diffusion rates, they should not be very different in magnitude. This is due to the fact that their difference is equal to the rate of change of diffusion rates (see equation 3.12). This rate of change is expected to be comparable with the diffusion rates themselves. On the other hand, very high adsorption and desorption rates means also that any small difference relative to them might be not that small compared to the diffusion rates. Thus small differences between the adsorption and desorption rates may cause considerable changes in the diffusion rates, and affect accordingly the gas phase and surface concentration profiles. Consequently, precise estimations of these rates are required for realistic modeling.

If we indicate the rate difference between adsorption rate and desorption rate as ADRD (Adsorption-Desorption Rate Difference), it can be thought that the ADRD will be positive on the left outer-surface since (net-)adsorption is expected to be dominant on this side. The molecules are expected to adsorb on the facial surface and in the pore, and serve to maintain the surface flow. Along the pore, ADRD will cease slowly and at an arbitrary point it will become zero indicating a local equilibrium point. The exact place of this local equilibrium point is expected to be dependent on many parameters, which affect the rates of diffusion and ADRD as well, such as; surface properties, gas concentrations, temperature, etc.. Beyond this point, desorption will be expected to be dominant (a negative ADRD) and the adsorbed species will be released back to the gas phase from the remaining part of the pore and finally from the outlet-side (right) outer-surface. All of these imply that up to the local equilibrium point the surface will have below-equilibrium and beyond it above-equilibrium concentrations. Owing to the definition of the steady-state there can be no accumulation of mass, therefore the total amount adsorbing before the equilibrium point should exactly be equal to the total amount desorbing after it. In other words, the integral of ADRD over the whole surface has to be zero.

Since the gas phase flow and surface flow are coupled through the adsorption and desorption rates, the gas phase profile cannot be the same for

the cases without and with surface diffusion. Thus determination of the gas phase profile as if there were no surface diffusion (decoupled flows), and then calculation of the surface concentration profile based on this determined profile will most probably give unrealistic values. Although the total flow stays constant, the individual rates of surface flow and gas phase flow will change along the pore. As a consequence, the individual flows in the system cannot be represented by single values, therefore the utilization of eq. 3.9 is not as straightforward as it is usually interpreted. The surface concentration profile and consequently the surface flux calculated by this way can thus lead to unrealistic results. Consequently, any parameter (e.g., surface diffusion coefficient) based on that calculation will be questionable as well, as long as the error associated with the utilization of the assumption is not estimated.

As a summary, if there exists appreciable surface flow, all the above points indicate that the behavior of the concentrations and the fluxes have to be much more complex than the commonly estimated behavior. It can be expected that for low surface flow rates or very long pores (very low ADRD per unit area) the system may practically behave as if in equilibrium. Even in that case, one should note that adsorption-desorption equilibrium would be a satisfactory simplification but not the reality.

3.2.4 Review of Knudsen Diffusion

Books on mass transfer and diffusion treat the topic *Knudsen diffusion* usually very shortly saying that the diffusion coefficient can be calculated by a simple formula (e.g., Cussler²³, Bennett and Myers⁹², Kärger and Ruthven⁸³, Satterfield⁸⁷, Dogu⁹³). More details about it can only be found in books about vacuum technology (see e.g., Chambers⁹⁴, O'Hanlon⁹⁵, Livesey⁹⁶) or in related articles (such as Steckelmacher⁹⁷). The actual calculation procedure, the idea of conductance and/or transmission probability, beaming effects, entrance and exit effects, pores of different shapes and different lengths, calculation procedure for pores in series, etc., are only covered in publications. For long pores (say $\bar{L} = l_p/r_p \geq 500$) the simple formula gives good

estimates^{xv}, but for shorter pores (and most probably for a network of pores) the error value will not be negligible anymore^{xvi}. Therefore, a review of the basics of *Knudsen diffusion* and some useful parameters related to it would be most valuable for the correct modeling of pores under such conditions.

To determine if a particular system is under Knudsen diffusion conditions, a quantity called *Knudsen number*^{xvii}, N_{Kn} , should be determined. It is defined as the ratio

$$N_{Kn} = \frac{\lambda}{a} \quad (3.20)$$

where λ is the mean free path and a is the characteristic scale, such as radius of a cylindrical pore⁹⁹. Three different regimes of flow can be distinguished depending on the value of the Knudsen number. According to Youngquist⁹⁸, the Knudsen diffusion appears to dominate when $N_{Kn} > 10$, and ordinary diffusion predominates when $N_{Kn} < 0.1$ ^{xviii}. In between, the so called transition region occurs. For different regimes, there exists different procedures and models for flow calculations⁹⁹. We will be concentrating on the sole Knudsen diffusion case.

Another useful parameter that should be emphasized for Knudsen diffusion case is the *transmission probability*, α^t . It is defined to be the probability that a molecule entering from one side of the pore will leave from the other side⁹⁵. This definition then leads to another parameter, *conductance* (C^d), which can be found from the following equation.

$$C^d = \alpha^t \frac{\langle \bar{v} \rangle}{4} A_p \quad (3.21)$$

where $\langle \bar{v} \rangle$ is the thermal velocity of the gas and A_p is the cross-sectional area of the pore. The conductance basically defines the amount of gas (in *volume/time*) that is passing through the pore, provided that the exit side is at absolute vacuum.

^{xv}e.g., for $\bar{L} = 1000$ the error in calculation of transmission probability is $< 1\%$

^{xvi}e.g., for $\bar{L} = 100$ the error is $\approx 5\%$, for $\bar{L} = 50$ the error is $\approx 10\%$

^{xvii}In the literature the Knudsen number may be variously defined, for a cylindrical tube, as $\frac{\lambda}{r_p}$, $\frac{\lambda}{d_p}$, $\frac{r_p}{\lambda}$ or $\frac{d_p}{\lambda}$. See e.g., Chambers⁹⁴, Youngquist⁹⁸, and Sharipov and Seleznev⁹⁹.

^{xviii}For example Livesey⁹⁶ gives another range of values: Knudsen diffusion dominates for $N_{Kn} > 1$, ordinary diffusion dominates for $N_{Kn} < 0.02$.

The α^t value used to get the commonly used Knudsen diffusion coefficient, i.e., $D_{Kn} = \frac{2}{3}r_p\langle\bar{v}\rangle$, is actually equal to:

$$\alpha^t = \frac{8}{3} \frac{1}{\bar{L}} = \frac{8}{3} \frac{r_p}{l_p} \quad (3.22)$$

and as noted before it is only a good approximation for very long pores, additionally it is only valid for cylindrical pores. To see how it is related to the commonly known Knudsen diffusion coefficient one needs to study a sample case. If one assumes a long cylindrical pore with a concentration difference across, i.e., C_1 on the left- and C_2 on the right-side, the net molar flux through it can be calculated by taking the difference of the two flows (in opposite directions).

$$N_{net} = N_1 - N_2 = C^d \cdot C_1 - C^d \cdot C_2 = -C^d \cdot \Delta C \quad (3.23)$$

if now one inserts the conductance (combination of eqs. 3.22 and 3.21) into the above equation, the resulting equation resembles the Fick's first law of diffusion with the commonly used Knudsen diffusion coefficient.

$$N_{net} = -\frac{8}{3} \frac{r_p}{l_p} \cdot \frac{v_g}{4} \cdot A_p \cdot \Delta C = -D_{Kn} \cdot A_p \cdot \frac{\Delta C}{l_p} \quad (3.24)$$

A notice should be made here concerning the insertion of the gradient ($\frac{dC}{dz}$) instead of the difference ($\frac{\Delta C}{l_p}$) in the above equation. Although, generally it does not have an affect on the result, such a replacement is theoretically not correct. The net flux of molecules from the entrance to the exit actually consists of two independent fluxes. Although it is proportional to the pressure difference across the pore, it is not driven by a pressure (or concentration) gradient (p.86, Livesey⁹⁶). It should be also noted that pressure inside such a pore will be anisotropic (p.44, O'Hanlon⁹⁵), contrary to the case in a bulk of a gas. The flow dynamics are thus very different from the continuum flow.

In general, there has been many attempts to estimate the transmission probability with simpler formulae, covering both short and long pores; numerical solutions and integration methods have been applied for its calcula-

tion^{97,99–102}. It is also possible to calculate transmission probability values by *Monte-Carlo* simulation techniques^{95,103,104} or some other more advanced methods¹⁰⁵.

When compared (see table 3.11), one can see the difference between the commonly used estimation (eq. 3.22) and the other more precise values.

Table 3.11: Comparison between transmission probability values calculated with different approaches.

L_p/r_p	eq. 3.22	DeMarcus ⁺	Berman [*]	Monte Carlo Sim. [*]
10	0.2667	0.1909	0.19099	0.1909417
16	0.1667	0.1317	0.13175	—
20	0.1333	0.1093	0.10938	0.1093193
40	0.0667	0.05951	0.05949	—
50	0.0533	—	0.04851	0.0484807
100	0.0267	0.02529	0.02529	0.0252781

taken from ⁺Steckelmacher¹⁰⁶, ^{*}O'Hanlon⁹⁵, ^{*}Szwemin and Niewinski¹⁰³

Talking about Knudsen flow, one should also be aware of the beaming effect. The beaming effect is the deviation of the distribution of molecular velocities from the spherical cosine distribution. At the exit of the pore, as the pore length to radius ratio increases, the molecular velocities start to give a distribution that looks like a pointed beam. In other words, as the pore becomes longer and longer, more and more molecules leaving from the exit tend to have a common direction of departure. Also the molecules leaving from the inlet, are distributed different than the spherical cosine distribution (see fig. 3.14) depending again on the pore length to radius ratio.

When the molecules enter the pore, there will be a reduction in number density at the pore entrance because, compared with the bulk gas, some molecules proceed down the pipe. This reduction can be called the entry loss (entrance effect). Moreover, a gauge located at the exit cross-section looking upstream will measure, a higher pressure than the pressure in the downstream. This difference may be thought as an exit loss (exit effect)

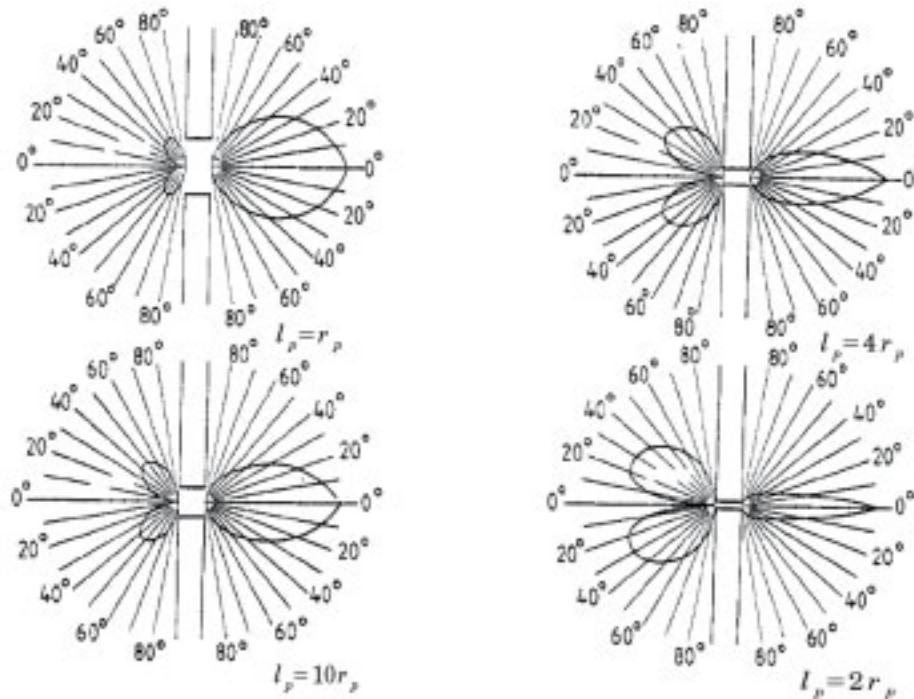


Figure 3.14: Polar diagrams showing beaming effect at the entrance and exit of a cylindrical pore at various pore lengths ($l_p = r_p, l_p = 2r_p, l_p = 4r_p, l_p = 10r_p$)¹⁰⁷.

associated with the motion of the gas molecules becoming once more totally randomized (p.102-104, Chambers⁹⁴).

Calculating the conductance of series (or a network) of such pores will not be straight forward due to the above behaviour. Making an analogy between electrical resistances and the diffusional resistances, leads to the result that a series of conductances would yield a total conductance of

$$\frac{1}{C_{total}^d} = \frac{1}{C_1^d} + \frac{1}{C_2^d} + \frac{1}{C_3^d} + \dots \quad (3.25)$$

That would be the equation for the case given in fig.3.15 (a), where the two pores are isolated by large volumes and the gas leaving one pore is allowed to get back to the bulk state (random distribution). But in the second case, fig.3.15 (b), the pores are connected directly and this randomization is not achieved and the molecules are reflected further.

In such a case, the final transmission probability can be estimated by Oatley's formula (eq. 3.26), which accounts for the pressure drop. This for-

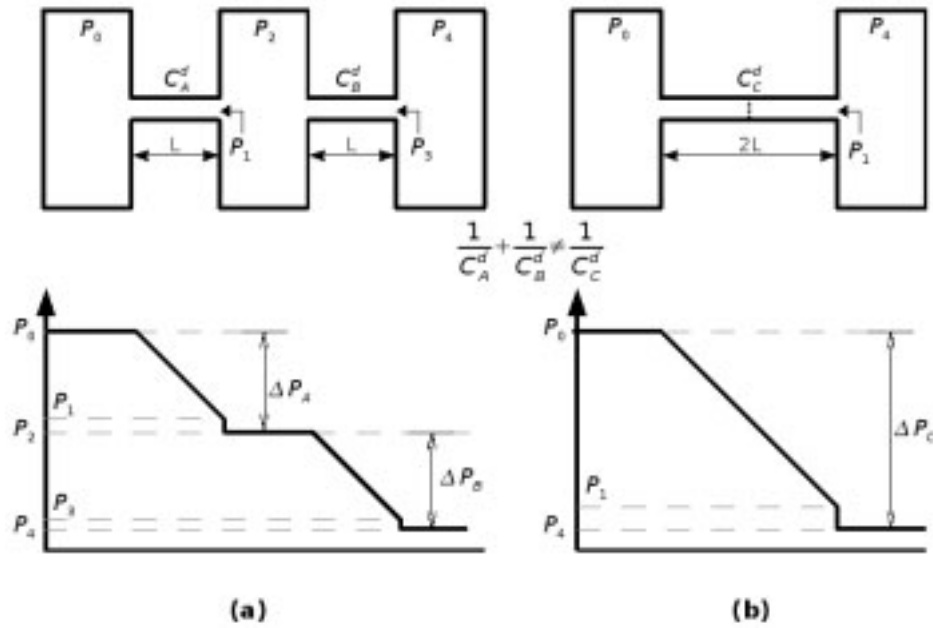


Figure 3.15: Series conductance of two pores: (a) two pores are isolated by a large volume in between, which serves to randomize the velocity distribution of the molecules. (b) two pores are connected directly, therefore the molecules are reflected further and the velocity distribution is thus not randomized. The pressure readings for both cases are those measured by a gauge in the gas stream pointing upstream and parallel to the flow direction⁹⁵.

mula applies to elements of same diameters. But if the series of components are of different diameters, the formula of Haefer, eq. 3.27, should be used. It should be noted that both of these formulae remove the biggest error in calculating the conductance of combinations, that is the exit conductance drop at the end of each junction, but neither formula corrects the entrance effects, that is, non-cosine or beamed entrance flux.

$$\frac{1 - \alpha_{total}^t}{\alpha_{total}^t} = \frac{1 - \alpha_1^t}{\alpha_1^t} + \frac{1 - \alpha_2^t}{\alpha_2^t} + \frac{1 - \alpha_3^t}{\alpha_3^t} + \dots \quad (3.26)$$

$$\frac{1}{A_1} \cdot \frac{1 - \alpha_{1 \rightarrow n}^t}{\alpha_{1 \rightarrow n}^t} = \sum_{i=1}^n \left[\frac{1}{A_i} \cdot \left(\frac{1 - \alpha_i^t}{\alpha_i^t} \right) \right] + \sum_{i=1}^{n-1} \left[\left(\frac{1}{A_{i+1}} - \frac{1}{A_i} \right) \cdot \delta_{i,i+1} \right] \quad (3.27)$$

where A_i is the inlet area of each element, and

$$\delta_{i,i+1} = \begin{cases} 1 & : A_{i+1} < A_i \\ 0 & : A_{i+1} \geq A_i \end{cases} \quad (3.28)$$

O'Hanlon⁹⁵ notes that the beaming effect in most real molecular flow situations does not introduce major effects, because real systems are made up of short tubes connected by elbows, traps, and so on. And it is known that short tubes have near-cosine exit flux. Any component containing an elbow, baffle, chevron, or the like will also scatter molecules and shift the distribution towards cosine.

As a consequence, a simple model with Fick's Law formula using the simple Knudsen diffusion coefficient may not be good enough to mimic the behaviour of real pore network systems. The effect of the length and the spatial distribution of the pores cannot be incorporated by this simple approach. The introduction of a reaction and/or surface diffusion may make the situation even more complicated.

Thus, building a model that has the potential to integrate at least some of the above phenomenon into itself would be taking one step closer to reality. In order to build such a model, one has to return back to the very basics that govern the essentials of the system at hand.

Modeling of Knudsen flow from basics

When the mean free path of the gas is larger than the characteristic scale of the pore, that is under Knudsen flow conditions, the gas-surface interaction becomes a determining parameter in the modeling of gas flow through pores. Knudsen argued that, under free molecular flow conditions, a cosine-law(-distribution) of diffuse emission or reflection from the wall surfaces was the most reasonable assumption. He stated that each molecule is rejected with the same probability in any arbitrary azimuth, and the probability of a given angle of emergence is given by the cosine-law. The direction in which a molecule is leaving the wall is completely independent of the incident one.

Steckelmacher⁹⁷ notes that the Knudsen law (cosine-law) can be accepted as a correct basis for the evaluation of rarefied gas flow in both simple and complex vacuum systems as well as related fields, although under some conditions deviations are known to exist.

In the Cartesian coordinate system, the cosine-law can be written as (see fig. 3.16)

$$dn = \frac{N_0}{\pi} \cos\theta \, d\omega = \frac{N_0}{\pi} \cos\theta \sin\theta \, d\theta \, d\phi \quad (3.29)$$

where dn is the molecular flux through $d\omega$, N_0 is the total molecular flux from the surface element A , θ is the angle with the surface normal, $d\omega (= \sin\theta \, d\theta \, d\phi)$ is the solid angle and ϕ is the azimuthal angle.

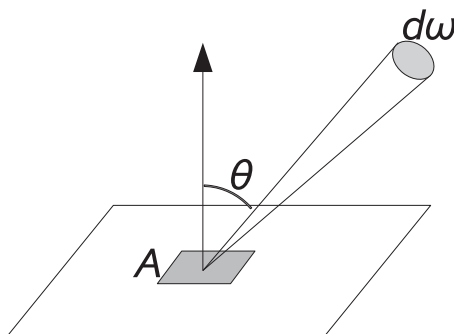


Figure 3.16: Traditional representation of cosine-law. A is a plane surface element, θ represents the angle with the surface normal, $d\omega$ is the solid angle. The molecular flux through $d\omega$, i.e., dn , can be related to N_0 , the total molecular flux from the surface piece A , as follows: $dn = \frac{N_0}{\pi} \cos\theta \, d\omega$.

Nevertheless, the implementation of the formula can sometimes be cumbersome and susceptible to mistakes¹⁰⁸. The above given formula and approach are the traditional way of approaching the cosine-law. But by reconsidering the meaning of the law, an alternative representation, which may be even easier to visualize, can also be given.

Knudsen designed his experimental set-up such that there existed a surface element A on the inner surface of a spherical bulb from which the molecules have been scattered^{109,110}. These molecules are found to cover the inner surface of the spherical bulb homogeneously. The cosine-law formula actually describes this distribution. In other words, if some molecules are scattered from a surface element A (which can be thought to be on a hypo-

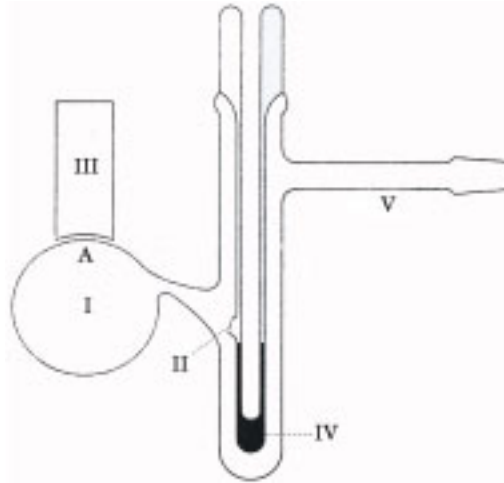


Figure 3.17: A sketch of the Knudsen's experimental set-up used to check the validity of the cosine-law^{109,110}. A is the surface (element) where the evaporated mercury molecules are allowed to be reflected. The bulb, except surface A , is kept at very low temperature to allow the mercury to solidify. The thickness of the mercury on the bulb is found to be homogeneous indicating the validity of cosine-law. I) spherical bulb, II) small hole through which mercury molecules escape into the bulb, III) metal vessel keeping the surface A warm, IV) mercury, V) connection to vacuum.

thetical sphere)(see fig. 3.18) and directed to go through another piece of sphere surface, e.g., A_1 , then according to the cosine-law, the ratio of these molecules to the total number of molecules scattered from A is equal to the ratio of the area of A_1 to the total area of the sphere.

For example, for a cylindrical pore the fraction of molecules leaving an infinitesimally small surface element on the pore wall and passing through the cross-section at a distance h is of interest. The infinitesimal surface element A , the hypothetical sphere, and the cross-section at b are all shown for the case $h = 2r$ in fig. 3.19a. Projecting the pore cross-section (b, c) onto the sphere, center of projection being the surface element A , produces a cone, whose base is the cross-section (b, c), and whose tip is the surface element A (see fig. 3.19b). Therefore, the sought area is the area on the sphere bounded by the intersection of this cone and the sphere. It should be noted that the ratio of the projection area to the total sphere area is independent of the sphere radius, and thus for simplicity the pore radius and the sphere radius are taken be equal. To get an impression of the above mentioned situation,

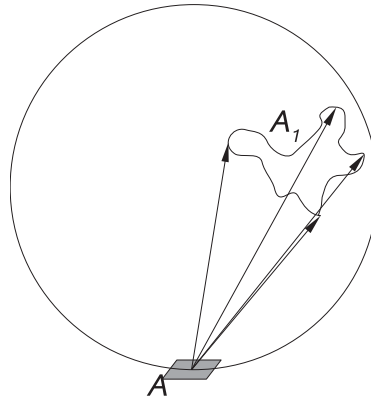


Figure 3.18: Alternative representation of the cosine-law. The fraction of molecules scattered from A and passing through A_1 is found by the ratio of the area of A_1 to the total sphere area, $\frac{n}{N_0} = \frac{A_1}{4\pi r_{sphere}^2}$.

the sphere, the cone, and the projection area on the sphere are all shown in fig. 3.19b-e.

Since the molecules do not collide with each other and travel only by colliding with the pore wall, the calculation of fraction of molecules leaving a surface element in a particular direction is important. Considering that the fraction of such molecules can be calculated by using the projection of the cross-section, this approach can be named as *projection approach*.

There are basically two main quantities to be calculated for such a case. The fraction of molecules leaving a surface element and passing through a pore cross-section at distance h , $\check{F}(h)$, and the fraction of molecules entering from the pore entrance and passing through the cross-section at distance h , $\check{G}(h)$. The exact procedure using projection approach and mathematical formulae for the calculation of these functions are given in the appendix.

If one discretizes the pore into slices, e.g., taking slice i into consideration, the system concerning the scattered molecules from a surface piece looks like as given in fig. 3.20. In the figure, the pore is divided into n slices with a constant thickness of Δz , and the molecules leaving slice i in various directions are shown. \check{F}_{i0} and \check{F}_{iL} are, respectively, the fraction of molecules leaving the pore from left and right ends. The \check{f} values seen in fig. 3.20 represent the fraction of molecules leaving slice i and impinging on another slice. These \check{f} values can be calculated by taking the difference between two

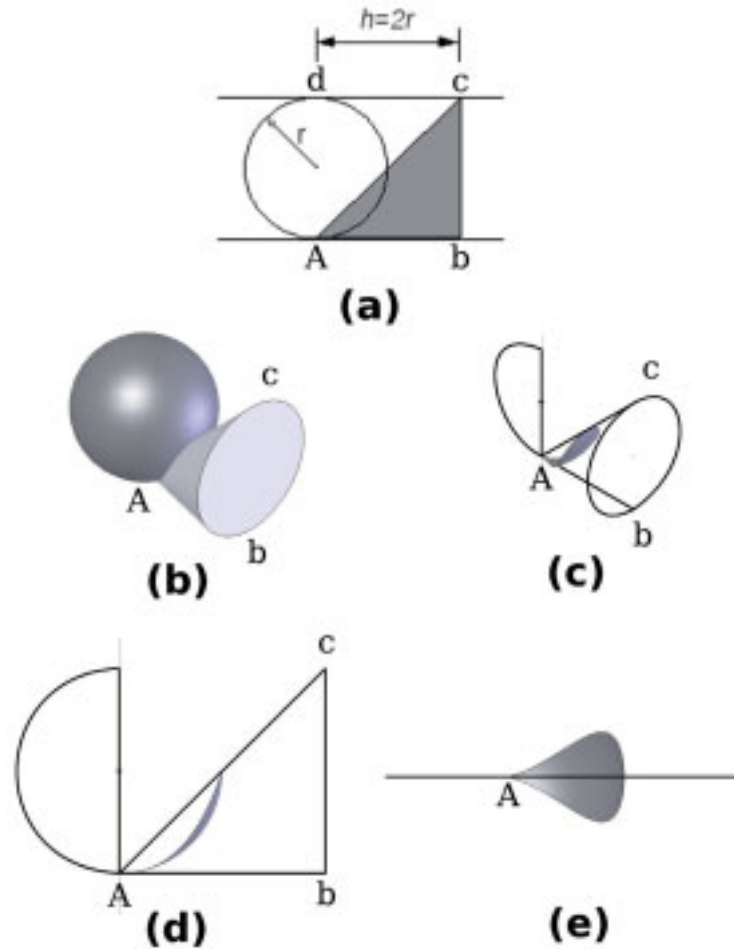


Figure 3.19: Projection of pore cross-section onto a sphere. The surface element A , the imaginary sphere (radius r), the cross-section at h ($h = 2 \cdot r$) are shown in a pore of radius r . (a) A 2-D representation of the system (b) A 3-D representation of the system (c) A 3-D representation of the projection area on sphere (d) Side-view of the projection area (e) Top-view of the projection area.

corresponding \check{F} values. In general, it can be defined as:

$$\check{f}_i = \check{F}\left(\left(i - \frac{3}{2}\right) \cdot \Delta z\right) - \check{F}\left(\left(i - \frac{1}{2}\right) \cdot \Delta z\right) \quad , \quad i \geq 2 \quad (3.30)$$

and

$$\check{f}_1 = 1 - 2 \cdot \check{F}\left(\frac{\Delta z}{2}\right) \quad (3.31)$$

The \check{f} value between the i^{th} and j^{th} slice corresponds to $\check{f}_{|j-i|+1}$.

The $\check{G}(h)$ is defined as the fraction of molecules entering from the pore entrance and passing through the right boundary of the corresponding slice

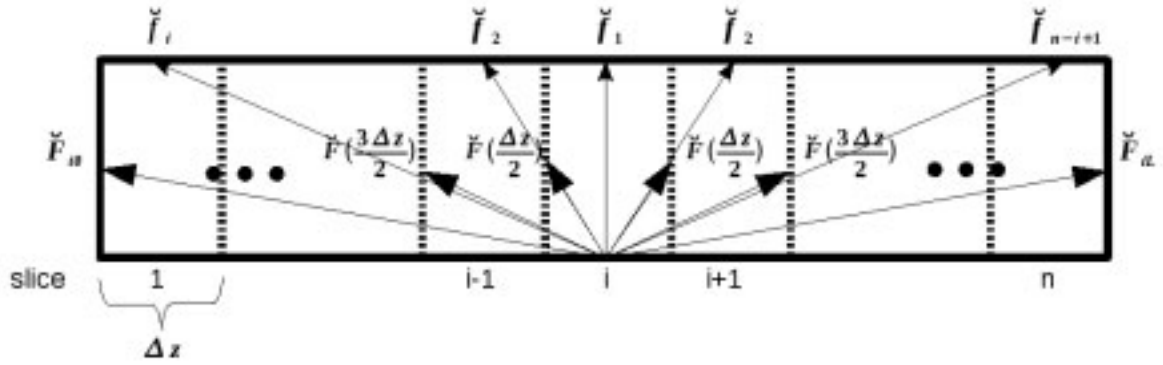


Figure 3.20: The distribution of flow from a slice to the other slices and to the two ends of the pore.

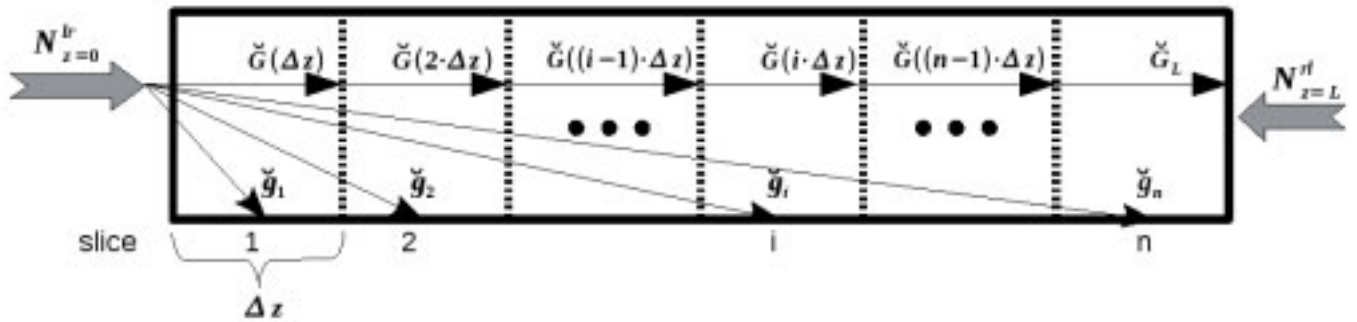


Figure 3.21: The distribution of the flow from the (left) pore entrance between slices and pore exit.

(see fig. 3.21), that is, $\check{G}(i \cdot \Delta z)$ is the fraction of molecules entering from the left pore entrance and reaching the right boundary of the i^{th} slice. Once again, the difference between the fraction of molecules reaching the right boundary and the left boundary of a slice gives the fraction of the molecules impinging on it, i.e., $\check{g}(i)$ (see fig. 3.21). Therefore,

$$\check{g}_i = \check{G}((i-1) \cdot \Delta z) - \check{G}(i \cdot \Delta z) \quad (3.32)$$

and also from fig. 3.21, the fraction of molecules leaving the pore without impinging on it is

$$\check{G}_L = \check{G}(n \cdot \Delta z) \quad (3.33)$$

A plot of \check{F} and \check{G} with respect to the normalized distance, $\frac{h}{r_{\text{pore}}}$, can be seen in fig. 3.22.

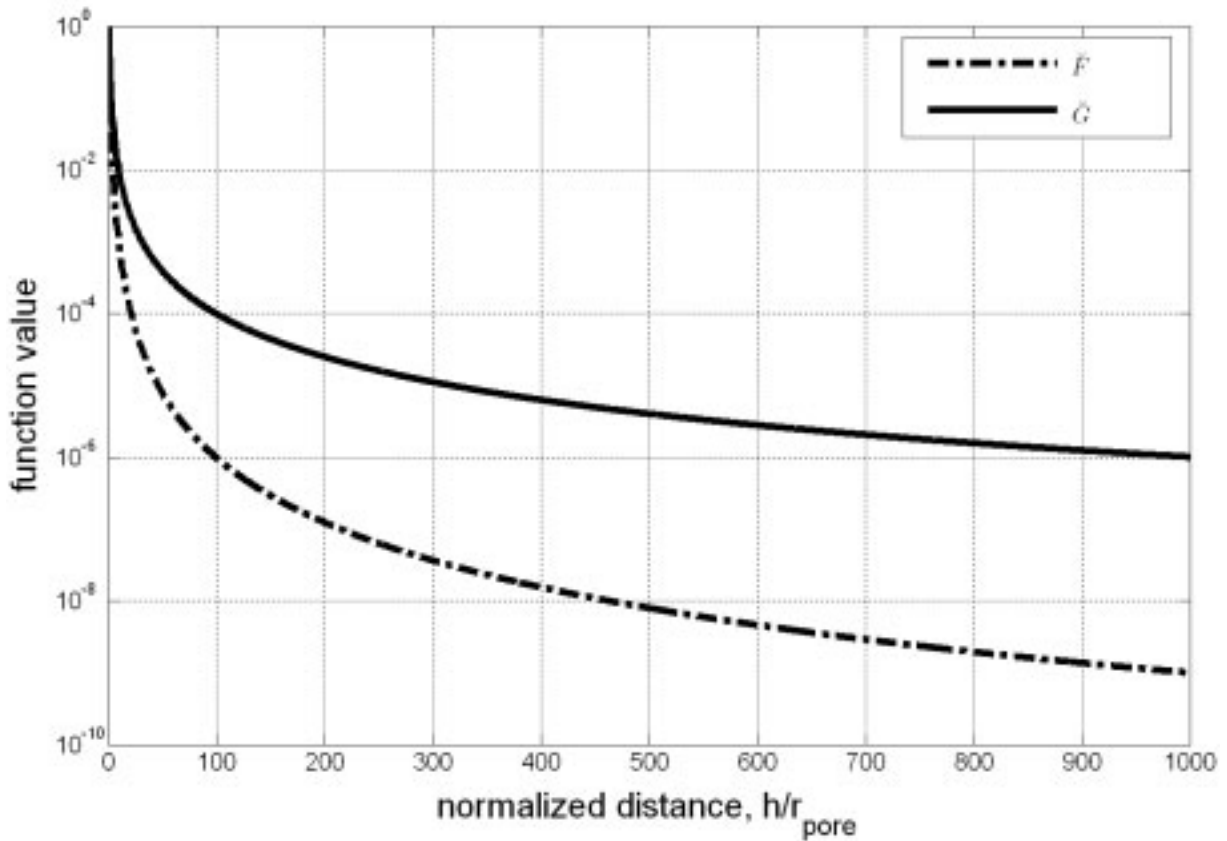


Figure 3.22: The log-scale plot of the functions \check{F} and \check{G} against the normalized distance between the emission point and the cross-section of interest. The distance is normalized with respect to the pore radius, and $\check{F}(0) = 0.5$ and $\check{G}(0) = 1$.

Using the above calculated quantities, the flux through a pore under Knudsen flow conditions, and also the impingement rate on the pore walls can all be calculated.

Calculating sole Knudsen flow using projection approach

The validity of a model can be shown by comparing results with other known models. Therefore, the well known situation sole Knudsen flow through a cylindrical pore into a vacuum is chosen. The results from projection approach will be compared with the results from traditional procedures. The equation system to be solved will be derived and solved using the projection approach.

The system is modelled under the following conditions:

- Steady-state flow
- No collisions between the molecules, i.e., pure Knudsen diffusion in gas phase
- The flux ($[mol/(area \cdot time)]$) of the incoming molecules at the pore entrance is homogeneously distributed over the entrance cross-sectional area, the velocities correspond to the average of the Maxwell distribution corresponding to a given temperature and the flow direction of the molecules follow the cosine-law
- Diffuse scattering (with cosine-law) for the collisions with the walls
- Absolute vacuum on the right end of the pore

In order to calculate the flow through the pore, one has to solve for the unknown impingement rates on the pore wall. Using the discretized pore from figs.3.20 and 3.21, the impingement rate on slices can be calculated by summing up the molecules coming directly from the pore entrance and the molecules coming from slices after reflection. Therefore, for the i^{th} slice, one can write:

$$N_{imp}(i) = N_{z=0}^{lr} \cdot \check{g}_i + \sum_{j=1}^n \left(N_{scat}(j) \cdot \check{f}_{|j-i|+1} \right) \quad (3.34)$$

For the case of gas pressure on both sides of the pore, i.e., no vacuum on the right side, a similar equation (eq. 3.35) would describe the system. Here, the additional term accounts for the molecules entering from the right pore entrance and directly reaching onto the slice i . Since this equation is a more general case, it will be utilized for the rest of the derivations. If one wants to get the case of *absolute vacuum* on the right side, one needs only to set the $N_{z=L}^{rl}$ value to *zero* in the following equations.

$$N_{imp}(i) = N_{z=0}^{lr} \cdot \check{g}_i + N_{z=L}^{rl} \cdot \check{g}_{n-i+1} + \sum_{j=1}^n \left(N_{scat}(j) \cdot \check{f}_{|j-i|+1} \right) \quad (3.35)$$

It should be noted that since a constant slice thickness is used, i.e. $\Delta z =$

const., the \check{g} values for the left entrance can be used also for the right pore entrance by making simple index switching. Since the i^{th} slice from the left is the $(n - i + 1)^{th}$ slice from right, \check{g}_{n-i+1} should be used to calculate the fraction of molecules impinging on i^{th} slice that are entering from right pore entrance.

The eq. 3.35 is only for the i^{th} slice, if all the equations for n slices are written, they can be combined to give a single equation in matrix form (note that $\check{g}_{flipped}(i) = \check{g}(n - i + 1)$):

$$(N_{imp})_{n \times 1} = \check{f}_{n \times n} \cdot (N_{scat})_{n \times 1} + N_{z=0}^{lr} \cdot (\check{g})_{n \times 1} + N_{z=L}^{rl} \cdot (\check{g}_{flipped})_{n \times 1} \quad (3.36)$$

where

$$(N_{imp})_{n \times 1} = \begin{bmatrix} N_{imp}(1) \\ \vdots \\ N_{imp}(i) \\ \vdots \\ N_{imp}(n) \end{bmatrix}, \quad (\check{g})_{n \times 1} = \begin{bmatrix} \check{g}_1 \\ \vdots \\ \check{g}_i \\ \vdots \\ \check{g}_n \end{bmatrix}, \quad (\check{g}_{flipped})_{n \times 1} = \begin{bmatrix} \check{g}_n \\ \vdots \\ \check{g}_i \\ \vdots \\ \check{g}_1 \end{bmatrix} \quad (3.37)$$

$$\check{f}_{n \times n} = \begin{bmatrix} \check{f}_1 & \check{f}_2 & \check{f}_3 & \dots & \check{f}_i & \dots & \check{f}_n \\ \check{f}_2 & \check{f}_1 & \check{f}_2 & \dots & \check{f}_{i-1} & \dots & \check{f}_{n-1} \\ \vdots & \vdots & \vdots & & \vdots & & \vdots \\ \check{f}_n & \check{f}_{n-1} & \check{f}_{n-2} & \dots & \check{f}_{n-i+1} & \dots & \check{f}_1 \end{bmatrix} \quad (3.38)$$

and $\check{f}_{n \times n}$ is a symmetric Toeplitz matrix. In general, a Toeplitz matrix is only perm-symmetric (p.183, Golub and Loan¹¹¹).

Under the condition sole Knudsen flow at steady-state, the impingement rate should be equal to the scattering rate, thus

$$(N_{imp})_{n \times 1} = (N_{scat})_{n \times 1} \quad (3.39)$$

The solution of N_{scat} using the system of linear equations (i.e., eq. 3.36) is then straight forward

$$(N_{scat})_{n \times 1} = \left(\check{f}_{n \times n} - I_{n \times n} \right)^{-1} \cdot \left(-N_{z=0}^{lr} \cdot (\check{g})_{n \times 1} - N_{z=L}^{rl} \cdot (\check{g}_{flipped})_{n \times 1} \right) \quad (3.40)$$

For the simpler case of absolute vacuum on the right side ($N_{z=L}^{rl} = 0$), the equation turns out to be

$$(N_{scat})_{n \times 1} = \left(\check{f}_{n \times n} - I_{n \times n} \right)^{-1} \cdot \left(-N_{z=0}^{lr} \cdot (\check{g})_{n \times 1} \right) \quad (3.41)$$

It may be worth noting that the $\left[\check{f} \right]_{n \times n}$ can be fully specified by its first row. All the values in other rows are a combination of the values in the first row. Therefore, an iterative algorithm can also be utilized to solve for the scattering rates by generating each row at a time instead of a direct solution of eq. 3.40.

An important quantity for Knudsen flow is the transmission probability. The transmission probability, w , is equal to the fraction of molecules leaving from the right pore-entrance, i.e., N_{right}^{out} , divided by the total number of molecules entering from the left.

$$w = \frac{N_{right}^{out}}{N_{z=0}^{lr}} \quad (3.42)$$

The N_{right}^{out} can be calculated by summing up the molecules passing through the pore without impinging on it (see fig. 3.21) and the molecules scattered from the pore slices in the direction of the right pore-entrance (see fig. 3.20):

$$N_{right}^{out} = N_{z=0}^{lr} \cdot \check{G}_L + \left(\check{F}_{iL} \right)_{1 \times n} \cdot (N_{scat})_{n \times 1} \quad (3.43)$$

where $\left(\check{F}_{iL} \right)_{1 \times n}$ is a row vector with elements corresponding to the fraction of molecules scattered from slices in the direction of the right pore-entrance.

The only parameters left for the evaluation, total number of molecules

entering the pore from the left entrance, $N_{z=0}^{lr}$ (fig. 3.21) , and from the right entrance, $N_{z=L}^{rl}$, can be calculated from the kinetic theory of gases as

$$N_{z=0}^{lr} = \frac{P_{left} \cdot \langle \bar{v} \rangle}{4RT} \cdot \pi r_{pore}^2 \quad ; \quad N_{z=L}^{rl} = \frac{P_{right} \cdot \langle \bar{v} \rangle}{4RT} \cdot \pi r_{pore}^2 \quad (3.44)$$

According to the kinetic theory, the number of molecules impinging on a unit surface is given by $\frac{P \cdot \langle \bar{v} \rangle}{4RT}$, where R is the universal gas constant, T is the absolute temperature, and $\langle \bar{v} \rangle = \sqrt{\frac{8RT}{\pi M_w}}$ is the mean average speed of gas molecules, with M_w being the molecular weight of the gas molecules. Therefore when multiplied with the pore cross-section, πr_{pore}^2 , it gives the amount of molecules entering from the pore entrance.

Results and Discussion for sole Knudsen flow case

Eq.3.41 has been evaluated using a MATLAB program. The flow diagram of the program can be seen in fig. 3.23. The results presented here and some additional results (up to p.104) have already been published in Argönül and Keil¹¹².

A note should be made here concerning the used slice thickness. The pore is originally assumed to be discretized into smaller elements than the slices, which are named *sub-slices*. And the \check{F} and \check{G} values for them are calculated before-hand and saved. These finer division of the pore provides higher resolution for the interaction of the pore slices within each other and with the pore entrances. But when it comes to the calculation of, e.g., N_{scat} , the equation system becomes unnecessarily large if one uses the sub-slices. One does not need such a high resolution for the N_{scat} (and later for surface coverage values), which are practically constant for a series of sub-slices. Consequently, the sub-slices can be bundled together into what is now called slices. For example if the relative slice thickness is chosen to be 0.01 ($\Delta \bar{z} = \frac{\Delta z}{r_{pore}} = 0.01$), and the relative sub-slice thickness is 0.002 ($\delta \bar{z} = \frac{\delta z}{r_{pore}} = 0.002$), five sub-slices are to be bundled together. The \check{F} and \check{G} values for the slice can then be calculated by taking the average of these values for the sub-

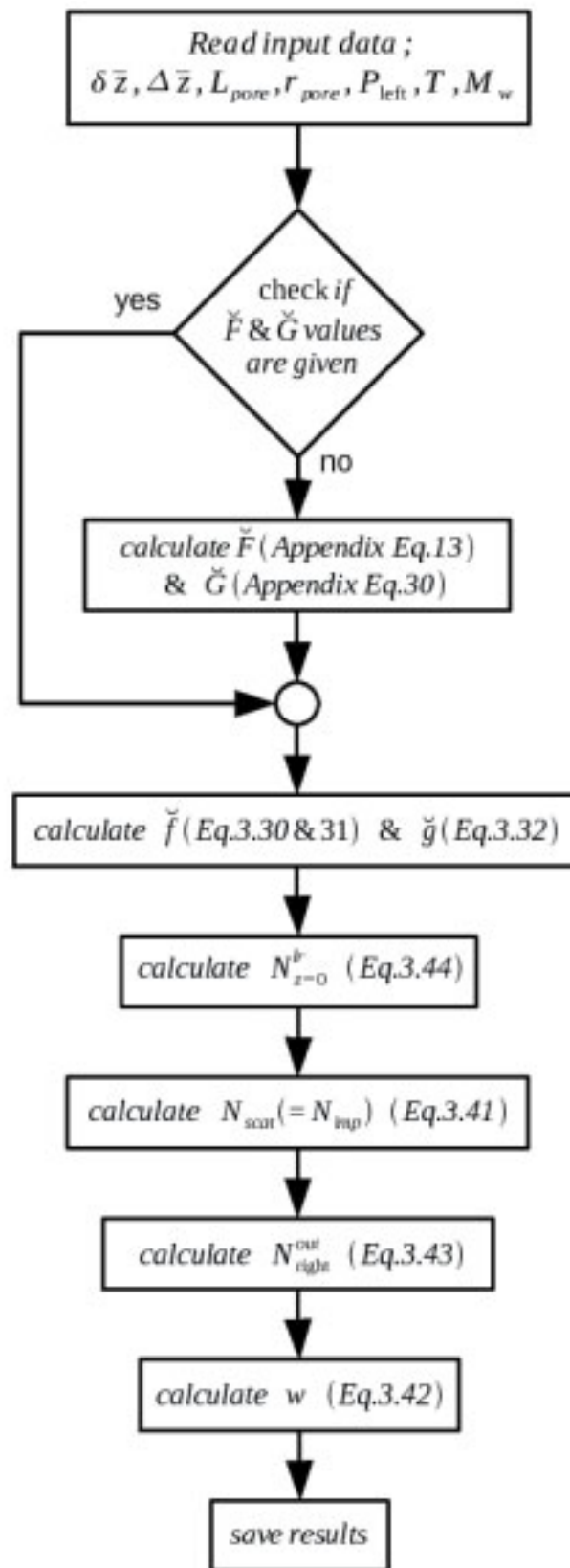


Figure 3.23: The flow diagram of the computer program for sole Knudsen case.

slices. The \check{F} and \check{G} values calculated in that way are more precise than the calculation using the corresponding slice, and also, for example, the matrix $\check{f}_{n \times n}$ is 25 times smaller than the case of using sub-slices. One just needs to choose appropriate values for the $\Delta\bar{z}$ and $\delta\bar{z}$ considering the system at hand.

Table 3.12: The effect of slice thickness on the transmission probability for a pore of length of ten times the pore radius with sub-slice thickness of $2 \cdot 10^{-3} \cdot r_{pore}$.

$\Delta\bar{z}$	n	w
1	10	0.202133
0.5	20	0.193796
0.2	50	0.191401
0.1	100	0.191057
0.05	200	0.190971
0.04	250	0.190961
0.02	500	0.190947
0.01	1000	0.190943

As an example a pore with a length to radius ratio of ten is simulated with various slice thicknesses (with a relative sub-slice thickness, $\delta\bar{z} = \frac{\delta z}{r_{pore}} = 2 \cdot 10^{-3}$). The results are tabulated in table 3.12 and plotted in fig. 3.24. It can be seen that as the relative slice thickness, $\Delta\bar{z} = \frac{\Delta z}{r_{pore}}$, gets smaller, the transmission probability becomes more precise. This also means that one can choose $\Delta\bar{z}$ (and $\delta\bar{z}$) accordingly to reach the desired level of accuracy.

To check the accuracy of the program and the model, calculated values from the projection approach are compared with values from the literature obtained by various methods. In table 3.13 column two shows the values calculated by the Knudsen formulaⁱ, column three presents the values of DeMarcus taken from Steckelmacher¹⁰⁶, column four are values of Berman taken from O'Hanlon⁹⁵ and column five are Monte-Carlo simulation results reported by Szwemin and Niewinski¹⁰³. The last two columns are the values

ⁱAlthough Knudsen formula ($8/3 \cdot r_{pore}/L_{pore}$) is valid for very long pores, it is included to show the extent of error made when it is to be used as an approximation.

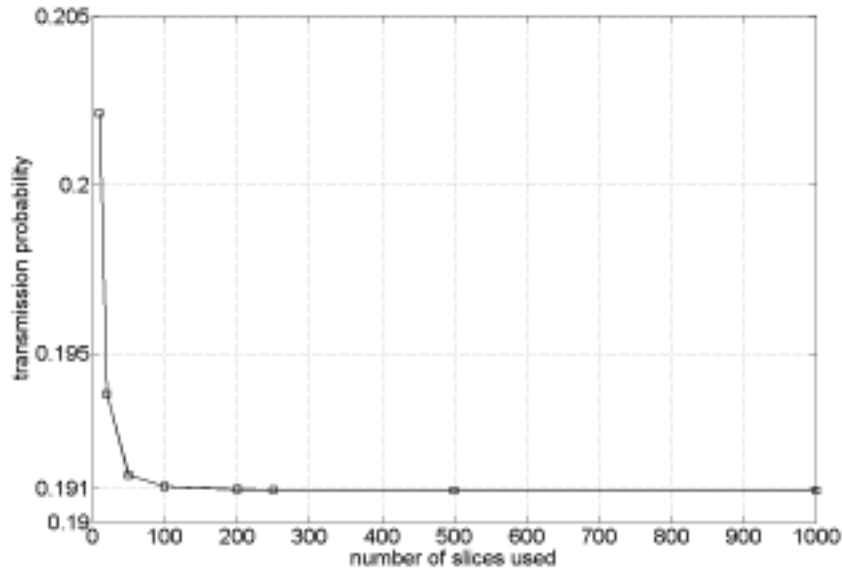


Figure 3.24: Effect of slice thickness on calculated transmission probability. A pore with length equal to $10 \cdot r_{pore}$ and $\delta \bar{z} = 2 \cdot 10^{-3}$ is used as an example. It can be seen that as the number of slices increase, i.e., the slice thickness decreases, the results converge.

calculated in this work. Two different slice thicknesses are used for the calculations in order to be able to estimate the last significant digit. A very good agreement of our results with the values given in the literature can be ascertained.

In order to check the effect of the slice thickness on the precision of the results, two more runs are made. For these runs, a $\delta \bar{z}$ of $2 \cdot 10^{-5}$ and $\Delta \bar{z}$ values of 0.005 and 0.002 are used. The results along with the other values are given in table 3.14. Although the precision of the coarser slice thicknesses are reasonable, the precision of the finer runs are at least one digit higher, as expected. Consequently, it can be concluded that the precision aimed at can be adjusted by proper choice of slice and sub-slice thicknesses.

For the impingement rate results, the table from Davies and Lucas¹¹³ is used for comparison (see table 3.15). They have compared the impingement rate at the entrance pore surface found by analytical approximations in the literature (first four columns) with their numerical solution (fifth column). The values using projection approach are found by fitting the calculated impingement rate values to a cubic spline curve and then extrapolating this

Table 3.13: Comparison between calculated transmission probabilities, w , (for $\delta\bar{z} = 2 \cdot 10^{-3}$) with various approaches from literature.

$\frac{L_{pore}}{r_{pore}}$	Knudsen $\left(\frac{8}{3} \frac{r_{pore}}{L_{pore}}\right)$	DeMarcus ⁺	Berman*	Monte Carlo Sim.*	This Work $\Delta\bar{z} = 0.04$	This Work $\Delta\bar{z} = 0.02$
10	0.2667	0.1909	0.19099	0.1909417	0.190961	0.190947
16	0.1667	0.1317	0.13175	—	0.131693	0.131684
20	0.1333	0.1093	0.10938	0.1093193	0.109331	0.109323
40	0.0667	0.05951	0.05949	—	0.059456	0.059452
50	0.0533	—	0.04851	0.0484807	0.0484813	0.0484776
100	0.0267	0.02529	0.02529	0.0252781	0.0252789	0.02527699

taken from ⁺Steckelmacher¹⁰⁶, ^{*}O'Hanlon⁹⁵, ^{*}Szwemin and Niewinski¹⁰³

Table 3.14: Comparison between calculated transmission probabilities with the literature for very short pores.

$\frac{L_{pore}}{r_{pore}}$	Berman ⁺	Monte Carlo Sim.*	This Work* $\Delta\bar{z} = 0.04$	This Work* $\Delta\bar{z} = 0.02$	This Work [‡] $\Delta\bar{z} = 0.005$	This Work [‡] $\Delta\bar{z} = 0.002$
0.05	—	0.97561375	—	—	0.97561222	0.97561218
0.1	0.95240	0.952398905	—	0.952400	0.952399004	0.952398922
0.2	—	0.90921539	0.909226	0.909217	0.90921521	0.90921506
0.5	—	0.8012699	—	0.801277	0.8012718	0.8012715
1	0.67198	0.6719856	0.672016	0.671991	0.6719844	0.6719839

⁺O'Hanlon⁹⁵, ^{*}Szwemin and Niewinski¹⁰³, ^{*} $\delta\bar{z} = 0.002$, [‡] $\delta\bar{z} = 2 \cdot 10^{-5}$

curve to the pore entrance.

The impingement rate distribution for the pore lengths used above is plotted in fig.3.25. As noted by Davies and Lucas¹¹³, the curves are nearly linear, especially for relative pore lengths less than two, and are symmetric around the mid-point of the pore. For relative pore lengths bigger than two, the curve is slightly convex from the entrance to the mid-point and slightly concave afterwards. The impingement rate distributions calculated can also be compared with the assumption of a linear pressure change between pressures at the two ends of the pore. In such a case, the distribution would correspond to a line starting from unity at the pore entrance and passing

Table 3.15: Comparison of pore entrance impingement rate at the pore entrance between various methods

$\frac{L_{pore}}{r_{pore}}$	values from Davies and Lucas ¹¹³					This Work ⁺
	Helmer	Clausing	NPS1	NPS2	Chebysev	
0.02	0.504950	0.504963	0.504963	0.504965	0.504963	0.5049627
0.2	0.545455	0.546381	0.546401	0.546381	0.546381	0.5463803
0.4	0.583333	0.586079	0.586209	0.586080	0.586080	0.5860796
1	0.666667	0.673762	0.674709	0.673820	0.673813	0.6738115
2	0.750000	0.757359	0.759123	0.757814	0.757623	0.7576215
8	0.900000	0.900924	0.896037	0.899853	0.899098	0.8990976
40	0.976190	0.976204	0.971362	0.972991	0.974038	0.9740373

⁺ $\delta\bar{z} = 0.002$ and $\Delta\bar{z} = 0.01$

through 0.5 at the half-length of the pore. Such an assumption does not correspond to the distribution found for the pore lengths investigated and it can be said that it will only become reasonable for very long pores.

All the above results indicate that the projection approach delivers accurate results. Here, it should be noted that the method and its principles are not only applicable to cylindrical pores but to any cross-sectional shape. The cylindrical pore is chosen as an example due to its symmetry, which highly simplifies the calculations, and its common application in modeling diffusion.

Although the transmission probability is of more common interest, the impingement rate distribution will be most valuable for the cases where the gas flow is accompanied by surface flow and/or by surface reaction. Since both of these phenomena are dependent on the surface concentrations, and the surface concentrations are dependent on the impingement rate, knowledge about the exact behavior of this rate would enable better modeling of such systems.

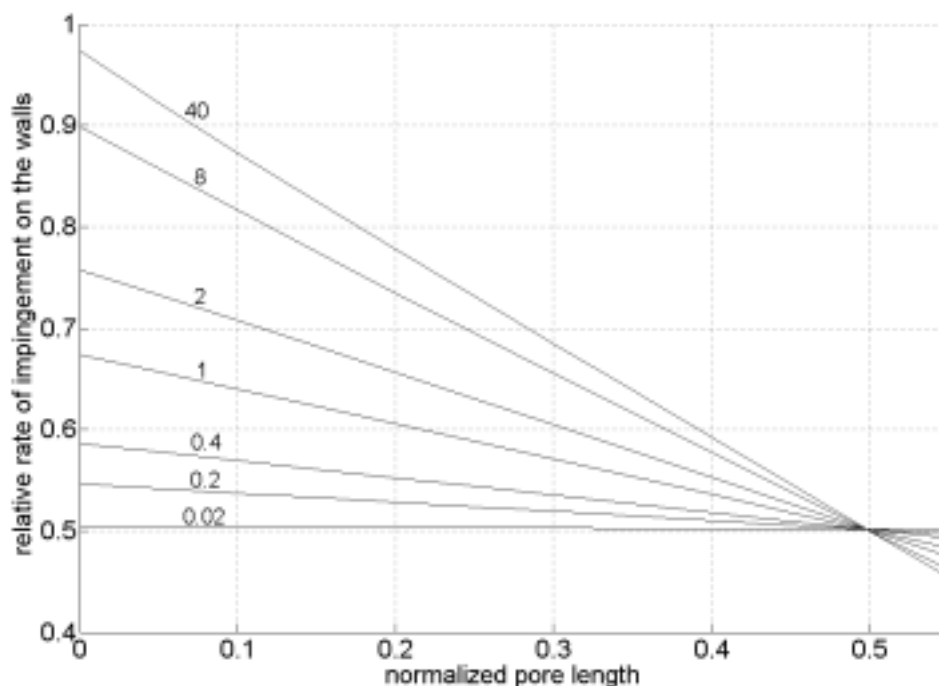


Figure 3.25: The relative impingement rate distribution inside a pore for various length to radius ratios. The numbers on the corresponding lines indicate the length to pore radius ratio.

Calculating Knudsen flow and surface flow using projection approach

Most of the time, when a porous system is modeled, the facial outer-surface area is not included in the model. Although for a purely gas phase diffusion system not important, for the case where there is surface diffusion, such a surface area becomes important to determine the boundary conditions for the surface flow. We have already developed such a model (see page 58) and it is going to be used here too.

A pictorial representation of the system, a cylindrical pore with both gas phase and surface flow, is given in fig.3.26. In the figure, C_A is the gas phase concentration of component A , G_A is the surface concentration, r_{ads} and r_{des} stand for adsorption and desorption rates and the F^{Surf} and F^{gas} represent the surface and the gas phase flow rates, respectively. In fig.3.26, the facial outer-surface area surrounding the pore entrance (see eq. 3.67 below) is the area on the left-end and right-end of the solid substance facing the bulk of

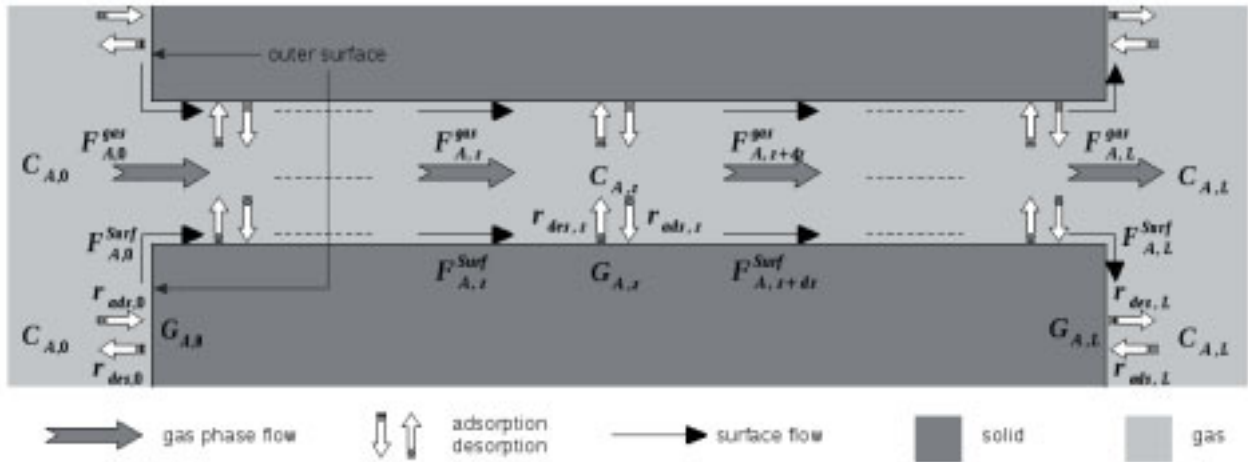


Figure 3.26: An overview of the pore and the outer-surfaces with the transport processes involved. Outer-surfaces are the solid surfaces facing the bulk of the gas on both sides of the figure ($G_{A,0}$ and $G_{A,L}$ are the surface concentrations on these surfaces). This figure is a repetition of fig.3.13.

the gas. Since F_0^{Surf} originates from the left outer-surface (*los*) and F_L^{Surf} terminates at the right outer-surface (*ros*), the boundary conditions for the surface flow are determined through the mass balances at the outer-surfaces.

The system is modeled under the following conditions:

- Steady-state flow
- No collisions between the molecules, i.e., pure Knudsen diffusion in gas phase
- The flux ($[mol/(area \cdot time)]$) of the incoming molecules at the pore entrance is homogeneously distributed over the entrance cross-sectional area, the velocities correspond to the average of the Maxwell distribution corresponding to a given temperature and the flow direction of the molecules follow the cosine-law.
- Diffuse scattering (with cosine-law) for the collisions with the walls
- Constant surface diffusion coefficient
- Langmuir type adsorption
- Monolayer surface diffusion, i.e., surface diffusion under the condition that the surface is covered below the monolayer adsorption capacity⁸⁰.

Under these conditions eq.3.36, given below for remembrance, is still valid.

$$(N_{imp})_{n \times 1} = \check{f}_{n \times n} \cdot (N_{scat})_{n \times 1} + N_{z=0}^{lr} \cdot (\check{g})_{n \times 1} + N_{z=L}^{rl} \cdot (\check{g}_{flipped})_{n \times 1}$$

A mass balance for slice i in the discretized pore (see figs.3.20 and 3.21) can be visualized as in fig.3.27, where $R_{ads,i}$ and $R_{des,i}$ are the adsorption and desorption rates [mol/s], and $N_{dir,i}$ represents the amount of molecules reflected directly [mol/s], i.e., without adsorbing.

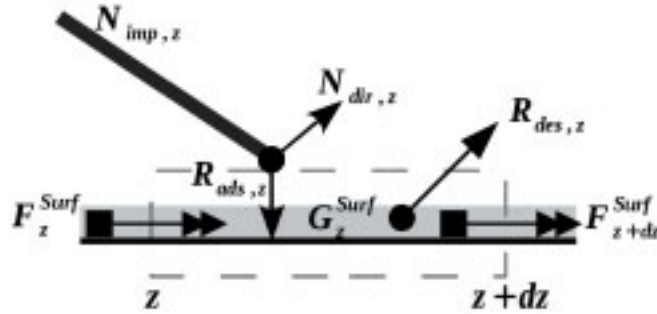


Figure 3.27: The pictorial representation of the mass balance for a control volume at the surface of the pore.

From fig.3.27, it can be seen that the total amount of molecules leaving the slice, i.e., scattered, is equal to the sum of molecules desorbed and molecules directly reflected:

$$N_{scat,i} = N_{dir,i} + R_{des,i} \quad (3.45)$$

additionally, the impinging molecules are either directly reflected or are adsorbed.

$$N_{imp,i} = N_{dir,i} + R_{ads,i} \quad (3.46)$$

Direct reflection of molecules can be due to three reasons; first, molecules impinging on a surface point that is not an adsorption site, second, molecules impinging on a surface piece that is appropriate for adsorption but already occupied by another adsorbed molecule and third, if the sticking coefficient, s_{coef} , is not unity, molecules impinging on free adsorption sites that are not adsorbed. If β_{ads} denotes the ratio of the surface area capable of adsorption (area of the adsorption sites) to the total surface area (obtained, for example, from BET measurements), and the adsorption is of Langmuir type, then the

rate of directly reflected molecules, N_{dir} , can be related to the above three points, respectively, as ($\theta_i \equiv$ surface coverage):

$$N_{dir,i} = N_{imp,i} \cdot (1 - \beta_{ads}) + N_{imp,i} \cdot \beta_{ads} \cdot \theta_i + N_{imp,i} \cdot \beta_{ads} \cdot (1 - \theta_i) \cdot (1 - s_{coef}) \quad (3.47)$$

In a simplified form eq.3.47 becomes:

$$N_{dir,i} = N_{imp,i} \cdot (1 - \beta_{ads} \cdot s_{coef} \cdot (1 - \theta_i)) \quad (3.48)$$

The β_{ads} can be estimated from the following formula

$$\beta_{ads} = \frac{\sigma_A \cdot q_{mono} \cdot N_{Av}}{S_{BET}} = \sigma_A \cdot G_{total} \cdot N_{Av} \quad (3.49)$$

where σ_A is the area of one adsorption site, which can be estimated to be equal to the area of the adsorbing species [$m^2/molecule$], q_{mono} is the monolayer coverage [mol/g_{cat}], N_{Av} is Avogadro's number [molecules/mole], S_{BET} is the B.E.T. surface area of the porous structure [m^2/g_{cat}] and G_{total} is the surface concentration of appropriate adsorption sites [mol/m^2].

According to Langmuir type isotherm, the desorption rate is proportional to the desorption rate constant, k_{des} [$mol/s/m^2$], and to the surface coverage.

$$R_{des,i} = k_{des} \cdot 2\pi r_{pore} \Delta z \cdot \theta_i = k'_{des} \cdot \theta_i \quad (3.50)$$

where k'_{des} , [mol/s], is the desorption rate constant based on the surface area of one slice. Thus, if eq.3.48 and 3.50 are inserted into eq. 3.45 and written in matrix form for the whole system, one ends up with:

$$(N_{scat})_{n \times 1} = (N_{imp})_{n \times 1} \cdot \times (1 - \beta_{ads} \cdot s_{coef} \cdot (1 - (\theta)_{n \times 1})) + k'_{des} \cdot (\theta)_{n \times 1} \quad (3.51)$$

where “ $\cdot \times$ ” represents element by element multiplication (Hadamard product).

Recalling the definition of N_{scat} , i.e., eq.3.45, and making a mass balance

for the surface element in fig.3.27, one can write that:

$$N_{imp,i} + F_{i-1}^{Surf} = N_{scat,i} + F_i^{Surf} \quad (3.52)$$

where the F^{Surf} represent the surface molar flow rates. Thus eq.3.52 can be written for the i^{th} slice, $1 < i < n$, conveniently as

$$N_{imp,i} = N_{scat,i} + (F_i^{Surf} - F_{i-1}^{Surf}) \quad (3.53)$$

For surface diffusion, Fick's first law combined with the finite difference approach reads as follows:

$$F_i^{Surf} = -D_A^{Surf} 2\pi r_{pore} G_{total} \frac{\theta(i+1) - \theta(i)}{\Delta z} \quad (3.54)$$

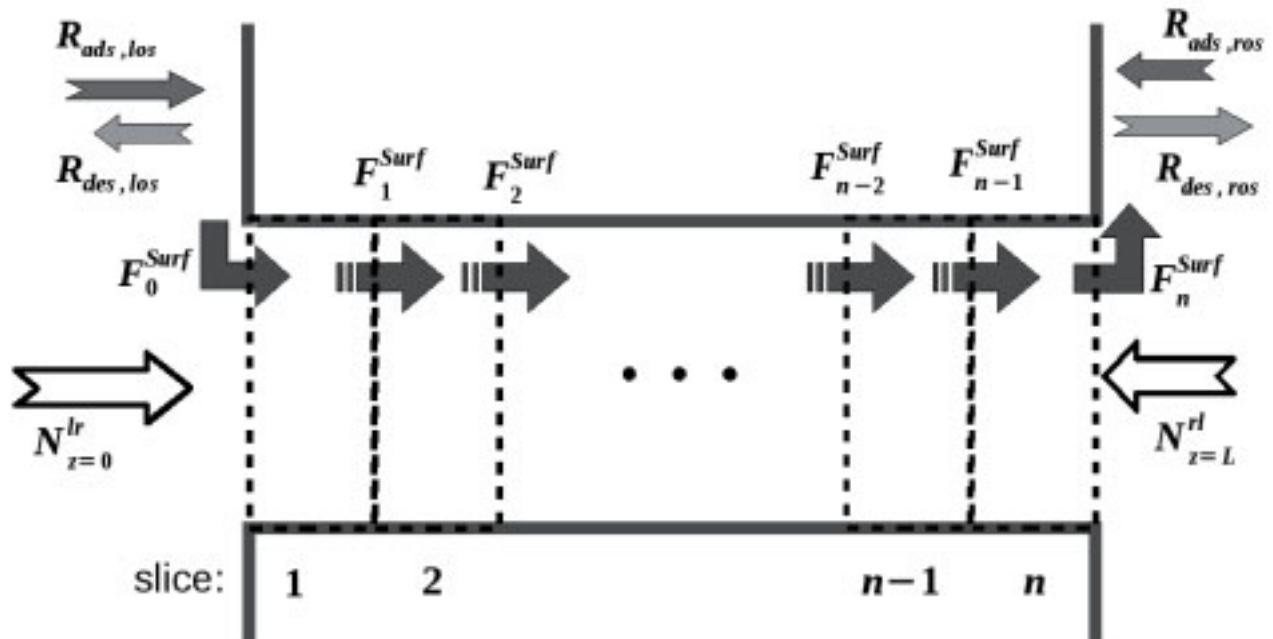


Figure 3.28: A plain representation of the surface flow in the porous substance that is divided into n slices.

From fig.3.28, it can be more clearly seen that the F_0^{Surf} and F_n^{Surf} are dependent on the left and right outer-surface (los , ros) coverages. If one takes the distance between los and the first slice, and between the last slice and ros as half of the slice thickness, i.e., $\Delta z/2$, then the corresponding surface

flow rates become:

$$F_0^{Surf} = -D_A^{Surf} 2\pi r_{pore} G_{total} \frac{\theta(1) - \theta_{los}}{\Delta z/2} \quad (3.55)$$

$$F_n^{Surf} = -D_A^{Surf} 2\pi r_{pore} G_{total} \frac{\theta_{ros} - \theta(n)}{\Delta z/2} \quad (3.56)$$

The mass balance for the first and the last slice then turn out to be:

$$N_{imp,1} = N_{scat,1} + (F_1^{Surf} - F_0^{Surf}) \quad (3.57)$$

$$N_{imp,n} = N_{scat,n} + (F_n^{Surf} - F_{n-1}^{Surf}) \quad (3.58)$$

In general, it can be written that

$$N_{imp} = N_{scat} + \Delta F^{Surf} \quad (3.59)$$

Consequently, eq.3.36 and 3.59 can be combined to give

$$(N_{scat})_{n \times 1} = \left(\check{f}_{n \times n} - I_{n \times n} \right)^{-1} \cdot \left(\Delta F^{Surf} - N_{z=0}^{lr} \cdot (\check{g})_{n \times 1} - N_{z=L}^{rl} \cdot (\check{g}_{flipped})_{n \times 1} \right) \quad (3.60)$$

which gives the dependence of N_{scat} on surface coverages (hidden in ΔF^{Surf}).

The gas phase flow rate inside the pore can be calculated based on the projection approach as follows (note that $\check{F}_{flipped}(i) = \check{F}(n - i + 1)$):

$$\begin{aligned} F_i^{gas} = & N_{z=0}^{lr} \cdot \check{G}(i \cdot \Delta z) - N_{z=L}^{rl} \cdot \check{G}((n - i) \cdot \Delta z) \\ & + \check{F}_{flipped}(1 : i) \cdot N_{scat}(1 : i) \\ & - \check{F}(1 : n - i) \cdot N_{scat}(i + 1 : n) \end{aligned} \quad (3.61)$$

In words that means: the molecules reaching the cross-section (at position $i \cdot \Delta z$) from the left entrance ($N_{z=0}^{lr} \cdot \check{G}(i \cdot \Delta z)$) minus the molecules coming from right entrance ($N_{z=L}^{rl} \cdot \check{G}((n - i) \cdot \Delta z)$) plus the molecules coming from slices on the left of the cross-section ($\check{F}(1 : i)_{flipped} \cdot N_{scat}(1 : i)$) minus the molecules coming from slices on the right ($\check{F}(1 : n - i) \cdot N_{scat}(i + 1 : n)$) gives

the net gas flow through that cross-section.

At steady state, the conservation of mass principle requires that the total flow rate should be constant throughout the whole pore. This requires the validity of the following equation at any cross-section:

$$F^{total} = F_i^{total} = F_i^{gas} + F_i^{Surf} = const. \quad (3.62)$$

Using the total flow rate at the left entrance (F_0^{total}) as basis, one can set up n independent equations describing the principle of constant total flow (eq.3.62)

$$0 = F_0^{total} - (F_i^{gas} + F_i^{Surf}) \quad , \quad i = 1, \dots, n \quad (3.63)$$

Eq.3.51 can be rewritten as follows:

$$0 = (N_{imp})_{n \times 1} \cdot \times (1 - \beta_{ads} \cdot s_{coef} \cdot (1 - (\theta)_{n \times 1})) + k_{des} \cdot 2\pi r_{pore} \Delta z \cdot (\theta)_{n \times 1} - (N_{scat})_{n \times 1} \quad (3.64)$$

The above two equations (3.63, 3.64) form the basis for the solution of the model. In addition to these, another equation can be set up which accounts for the fact that at steady-state there can be no accumulation of mass on the surface. This means that the net adsorption (i.e., the difference between adsorption rate and the desorption rate) over the whole surface should be zero. That covers both the facial outer-surfaces and surface inside the pore. It should be noted here that an overall adsorption-desorption equilibrium satisfies this condition but is a special case and is shown to be generally not possible (see chap.3.2.3). Thus,

$$0 = \sum_{\text{element}=1}^n ((N_{imp})_{n \times 1} - (N_{scat})_{n \times 1}) + R_{ads,los} - R_{des,los} + R_{ads,ros} - R_{ads,ros} \quad (3.65)$$

If the surface concentration on the *los* is assumed to be homogeneous, i.e., no concentration gradient on *los*, owing to mass balance, the rate of net adsorption on that surface would be equal to the surface flow rate (see

fig.3.26):

$$(r_{ads,0} - r_{des,0}) \cdot A_{solid/pore}^{face} = F_{A,0}^{Surf} \quad (3.66)$$

The $A_{solid/pore}^{face}$ is the facial solid outer-surface area per pore and can be calculated by making use of the porosity, ϵ , of the porous structure and the pore cross-sectional area as:

$$A_{solid/pore}^{face} = \frac{1 - \epsilon}{\epsilon} \cdot \pi r_{pore}^2 \quad (3.67)$$

The rate of adsorption and desorption at *los* according to Langmuir model are:

$$r_{ads,los} = k_{ads} P_{left} (1 - \theta_{los}) \quad (3.68)$$

$$r_{des,los} = k_{des} \theta_{los} \quad (3.69)$$

If one inserts eqs.3.68, 3.69 and 3.55 into eq.3.66 and rearranges, the final equation is:

$$\theta_{los} = \frac{k_{ads} P_{left} A_{solid/pore}^{face} + 2\alpha \theta(1)}{k_{des} A_{solid/pore}^{face} + k_{ads} P_{left} A_{solid/pore}^{face} + 2\alpha} \quad (3.70)$$

where $\alpha = D_A^{Surf} G_{total} 2\pi r_{pore} / \Delta z$. Similarly one can write for the right outer-surface (*ros*)

$$\theta_{ros} = \frac{k_{ads} P_{right} A_{solid/pore}^{face} + 2\alpha \theta(n)}{k_{des} A_{solid/pore}^{face} + k_{ads} P_{right} A_{solid/pore}^{face} + 2\alpha} \quad (3.71)$$

The adsorption rate is equal to the number of molecules impinging on the surface multiplied by the fraction of surface available for adsorption, times the fraction of free adsorption sites, times the sticking coefficient. Equating this to the known Langmuir adsorption rate would lead to the adsorption coefficient.

$$r_{ads} = \frac{P \cdot \langle \bar{v} \rangle}{4RT} \cdot \beta_{ads} \cdot s_{coef} \cdot (1 - \theta) = k_{ads} \cdot P \cdot (1 - \theta) \quad (3.72)$$

and consequently

$$k_{ads} = \frac{\beta_{ads} \cdot s_{coef} \cdot \langle \bar{v} \rangle}{4RT} \quad (3.73)$$

If one has the adsorption equilibrium constant, K_{ads} , then the calculation of k_{des} is straight forward

$$k_{des} = \frac{k_{ads}}{K_{ads}} \quad (3.74)$$

A short summary of the model

A single pore (or a simple parallel pore structure) under Knudsen flow accompanied by simultaneous surface flow with Langmuir type adsorption is modelled at steady-state. The model does not make the assumption of adsorption-desorption equilibrium, and it incorporates automatically the variation of flow rates with pore length and the so called entrance and exit effects. Any impinging molecule is taken to be either adsorbed or directly reflected. Scattered molecules are taken to be the sum of desorbed molecules and directly reflected molecules. The scattering is assumed to follow the cosine-law of reflection. For surface flow, Fick's law is assumed to be valid with a constant surface diffusion coefficient. Finite difference approach is followed and the pore length is discretized into n slices. Through mass balances, the necessary equations are set up.

The system of equations to be solved is eqs.3.63 and 3.64 with surface coverage (θ) as unknown. Required auxiliary equations are eqs.3.36, 3.54-3.56, 3.60, 3.61, 3.67-3.71 and 3.73-3.74. The solution should also satisfy eq.3.65, therefore this equation can be used to check the validity of the obtained solution. Physical constants used for the sample system chosen, description of the other simpler models used for comparison and also the details of the solution procedure are all given below.

Other models used for comparison

Two other models are used for comparison, and all the models are numbered with respect to increasing detail. The first one, i.e., *model I*, assumes

independent gas phase and surface flows accompanied with adsorption equilibrium, and additionally linear impingement rate distribution inside the pore between the reservoirs with different pressures at the two ends. It is equivalent to the simple Fick's law model with the common Knudsen diffusion coefficient with assumed adsorption-desorption equilibrium. All these assumptions are expected to be valid for long pores with relatively low surface flow case. The second model, i.e., *model II*, also assumes independent flows and adsorption equilibrium, but uses the projection approach for pure Knudsen flow to calculate the impingement rate distribution inside the pore. In that way, it does not use the common Knudsen diffusion coefficient and also does not assume linear impingement rate distribution. The model set up in this work is labeled as *model III*, and as explained in the previous sections it does not make any of the above assumptions. The gas phase and surface flows are related to each other through adsorption and desorption rates that are separately calculated.

Physical constants used for the sample case

A sample set of constants is taken from Chen and Yang¹¹⁴ where the values have been extracted from the experimental measurements of Gilliland *et al.*¹¹⁵. As an example, the system propylene (C₃H₆) in (Vycor-) glass is taken, which was found to exhibit monolayer adsorption, which corresponds to our model. The data is given in table 3.16, and other parameters used are shown in table 3.17.

Solution of equations

The equation system of *model III* is normalized by the theoretical gas phase flow rate calculated by the traditional Knudsen diffusion coefficient (i.e., $\Psi_{nrm} = -\frac{2}{3} \frac{r_{pore}}{L_{pore}} \cdot (P_{right} - P_{left}) \cdot \frac{\langle \bar{v} \rangle}{RT} \cdot \pi r_{pore}^2$). The normalized equation system is then solved using MATLAB (7.3.0, R2006b). The function 'fsolve' with 'LargeScale' function set to 'on' is used to solve the system of nonlinear equations. The equilibrium distribution of *model II* is used as an initial guess for the solution. To check the convergence behavior of the model, a

Table 3.16: Physical constants for the sample system propylene (C_3H_6) in (Vycor-) glass. The parameters are taken from Chen and Yang¹¹⁴.

Parameter	Value	Units
D^{Surf}	$13.32 \cdot 10^{-9}$	$[m^2/s]$
K_{ads}	$2.34 \cdot 10^{-5}$	$[1/Pa]$
q_{mono}	0.508	$[mol/kg]$
r_{pore}	$3.07 \cdot 10^{-9}$	$[m]$
S_{BET}	$143 \cdot 10^3$	$[m^2/kg]$
T	313.15	$[K]$
ϵ	0.31	$[-]$

sample system was simulated by modified initial guesses (which were taken to be very different from each other) and the system converged to the same solution for various runs made. Also as in the sole Knudsen flow case, subslices^{xix} are used to increase the precision. The flow diagram of the MATLAB program can be seen in fig.3.29.

Results and discussion

A pore length of $\frac{L}{r_{pore}} = 20$ has been chosen as an example. The pore is divided into slices of relative thickness of $\Delta\bar{z} = 0.05$. The pressure on the left-hand side of the pore was taken to be higher than the pressure on the right-hand side by 20 kPa, i.e., a constant pressure difference across the pore length, for all runs.

Total flow rate (Knudsen plus surface flow rate) and the flow enhancement with respect to the case of sole Knudsen flow are tabulated in table 3.18.

It should be noted that the flow enhancement is neither linearly dependent on the average pressure nor constant like the Knudsen flow rate.

The two extreme pressures can be analyzed as examples, since the behavior of the system in between can be deduced from these two extremes.

For the case $P_{left} = 30kPa$ the impingement/scattering rate distribution

^{xix}see page 78

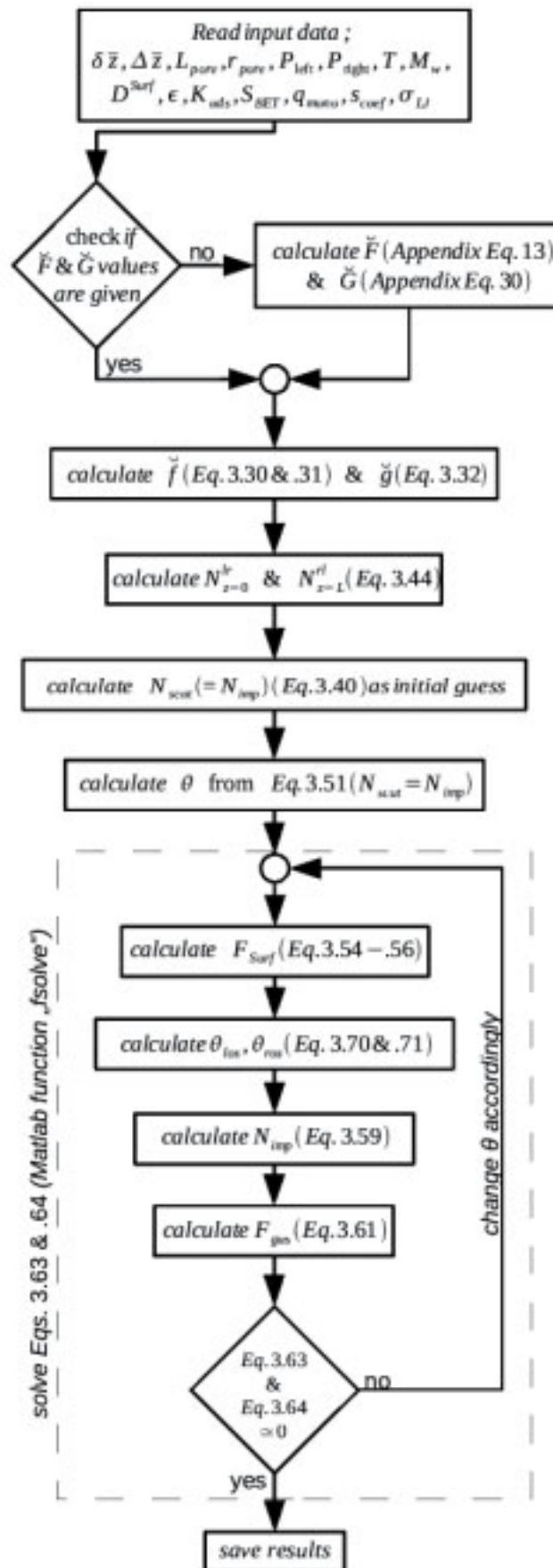


Figure 3.29: The flow diagram of the computer program for simultaneous surface and Knudsen flow case.

Table 3.17: Some other important parameters calculated and/or used for the sample system propylene (C_3H_6) in (Vycor-) glass.

Parameter	Value	Units
$A_{solid/pore}^{face} = \frac{1-\epsilon}{\epsilon} \cdot \pi r_{pore}^2$	$6.59 \cdot 10^{-17}$	$[m^2/pore]$
$G_{total} = \frac{q_{mono}}{S_{BET}}$	$3.55 \cdot 10^{-6}$	$[mol/m^2]$
$k_{ads} = \frac{\sigma_{area} \cdot N_{Av} \cdot G_{total} \cdot s_{coef}}{\sqrt{2\pi M_w RT}}$	$1.40 \cdot 10^{-2}$	$[mol/Pa/m^2/s]$
$k_{des} = \frac{k_{ads}}{K_{ads}}$	598.5	$[mol/m^2/s]$
M_w (propylene)*	$42.081 \cdot 10^{-3}$	$[kg/mol]$
s_{coef} (assumed value)	1	$[-]$
$\beta_{ads} = \frac{q_{mono} \cdot \sigma_{area} \cdot N_{Av}}{S_{BET}}$	0.3680	$[-]$
$\sigma_{area} = \frac{\pi \cdot \sigma_{LJ}^2}{4}$	$17.2 \cdot 10^{-20}$	$[m^2/molecule]$
σ_{LJ}^*	$4.678 \cdot 10^{-10}$	$[m]$

* pp. A.7, B.1. Poling *et al.*¹¹⁶

is shown in fig.3.30. The broken line with dots represents the linear pressure distribution inside the pore, i.e., *model I*. It starts from the left-hand side bulk pressure value and decreases linearly to the right-hand side bulk pressure value. The solid curve represents the pure Knudsen flow case and consequently the independent flow case (i.e., *model II*). The broken curve and dotted curve are the results of *model III* and represent the impingement rate and the scattering rate, respectively.

Apparently, the behavior of this particular system is different from the assumption of independent gas and surface flows in equilibrium. Although the calculated scattering and impingement rates seem to be close to each other, i.e., around equilibrium, *model III* allows the curves to shift away from the expected equilibrium curve, i.e., *model II*. It can be noted that although the *model I* and *model II* give symmetric curves, for *model III* the resulting distributions are not symmetric around the mid-point of the pore anymore. This shift and the unbalance are the results of the effect of the surface flow on the gas phase flow.

The relative difference between the adsorption and desorption rates can

Table 3.18: Total flow rate and flow enhancement with respect to sole Knudsen flow case for various pressures ($L/r_{pore} = 20$).

P_{left}^* [kPa]	F_{total} $10^{-15} \cdot [mol/s]$	Enhancement [%]
30	4.831	95.8
50	3.900	58.0
70	3.429	38.9
90	3.158	28.0
110	2.988	21.1
130	2.874	16.5
150	2.794	13.2

* $\Delta P = P_{left} - P_{right} = 20$ [kPa] in all cases.

be better seen in fig.3.31, where the adsorption-desorption rate difference (ADRD) is plotted, normalized by the adsorption rate versus pore length.

The triangles in the figure represent the values on the left and right outer-surfaces, where actually the biggest difference between adsorption and desorption is observed. It can be noticed that at *los* around 8.7% and at *ros* around 24.5% difference is created. This indicates that there is a considerable transfer of species between the gas-phase and the surface-phase at these regions. Inside the pore, the entrance and exit regions have non-equilibrium conditions, but the mid-region can be said to be at quasi-equilibrium. But as can be seen in fig.3.30, this quasi-equilibrium values cannot be calculated by simply assuming independent flows with equilibrium distribution. The system behaves close to equilibrium but far from the state found with independent gas flow and equilibrium assumption combination, and also behaves differently.

Nevertheless, the behavior in fig.3.31 has been expected^{xx}, the system is anticipated to have a net adsorption region first, then a local equilibrium point after that a net desorption region. Besides, the *los* has been expected to have net adsorption and the *ros* net desorption.

The adsorption and desorption rates are continuous inside the pore, but

^{xx}see page 61

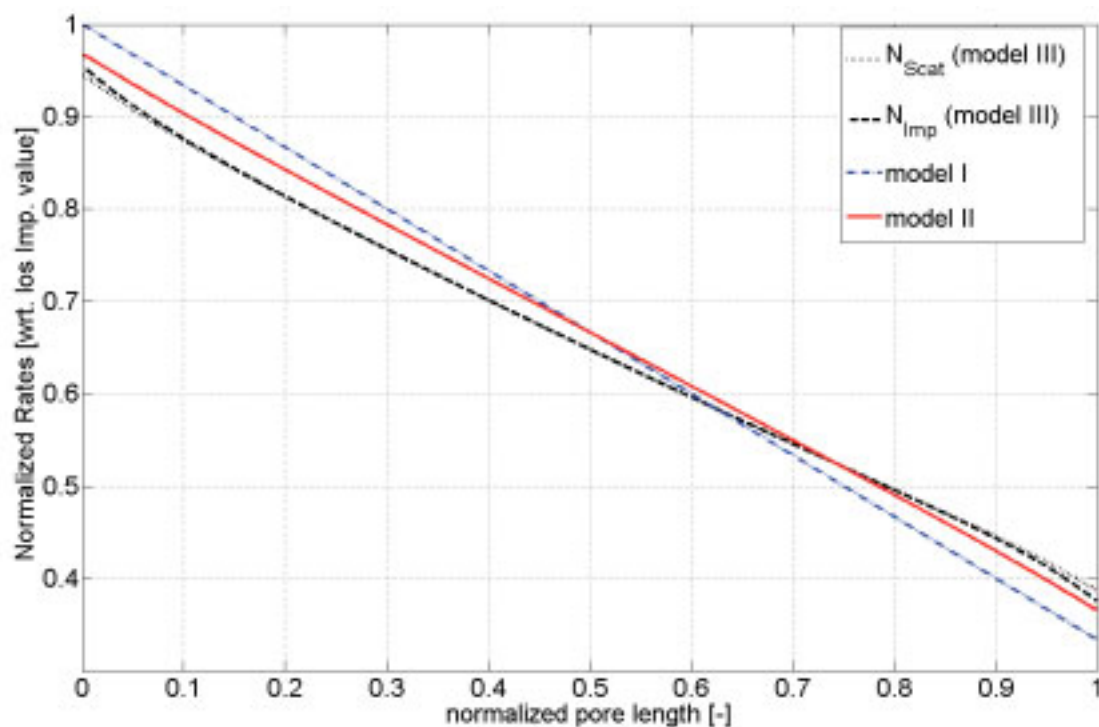


Figure 3.30: Comparison of impingement and scattering rates for the three models used for the case $P_{left} = 30kPa$. All the impingement and scattering rate values inside the pore are normalized by the impingement rate of the gas at the pressure of P_{left} .

there needs to be a jump between the values just at the entrance of the pore and the outer-surfaces due to the jump of the impingement rate (see fig.3.30, the *model III* curves do not start from 1 and end at $1/3$) at the same region. This is the reason for the discontinuity at fig.3.31 at two ends of the pore, between the curve inside the pore and the two end points at the outer-surfaces. Note also the asymmetry at the pore ends (fig.3.31) due to the different pressures in the reservoirs.

The surface coverage profiles for all three models are given in fig.3.32. Unlike the adsorption and desorption rates, the surface coverages and also the surface flow rate (fig.3.33a) are not discontinuous at the two ends.

As can plainly be seen in the fig.3.32, neither *model I*, nor *model II* are good estimates of the behavior of this particular system.

Fig.3.33 is maybe the most interesting graph for the system. As presented in the fig.3.33a, the surface flow rate originates from the left outer-surface and then increases along the pore length. This increase is most pronounced at

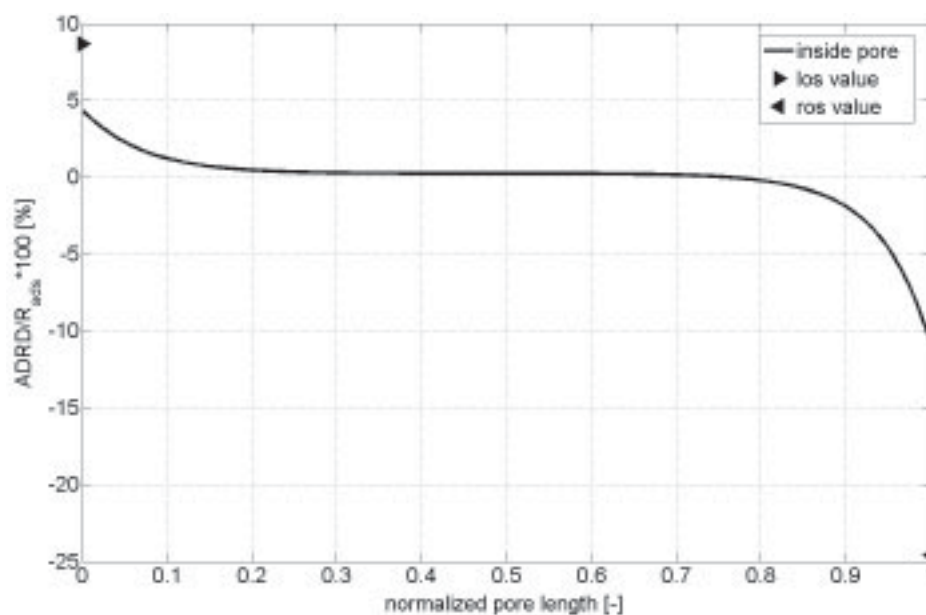


Figure 3.31: The adsorption-desorption rate difference for *model III* for the case $P_{left} = 30kPa$. The percentage difference between adsorption and desorption rates normalized by the adsorption rate. The left and right outer-surface values are also included in the figure.

the entrance region of the pore. In the deeper parts of the pore, the increase is small but still existent. These effects are due to net adsorption along this pore portion. Since the total flow rate is constant (steady-state flow), the gas phase flow rate decreases accordingly (see fig.3.33b). Close to the end of the pore, the surface starts to desorb more molecules than it adsorbs, and the surface flow rate begins to decrease after some point in the pore, and finally comes to the right outer-surface value. The amount of surface flow reaching the *ros* is given back to the bulk of the gas by net desorption from the outer-surface, which then causes the big difference between adsorption and desorption there.

It should be noted here that, for example for the other extreme case, i.e., $P_{left} = 150kPa$, the impingement rate and surface coverage are very close to the equilibrium distribution (see fig.3.34a-b). But the surface flow follows a similar behavior (fig.3.34c) as in the previous case. Here *model II* and *model III* behave similarly except for the entrance and exit regions of the pore. A notice should be made here concerning the surface flow rates. In the latter case the surface flow enhancement is only 13.17%, but for the

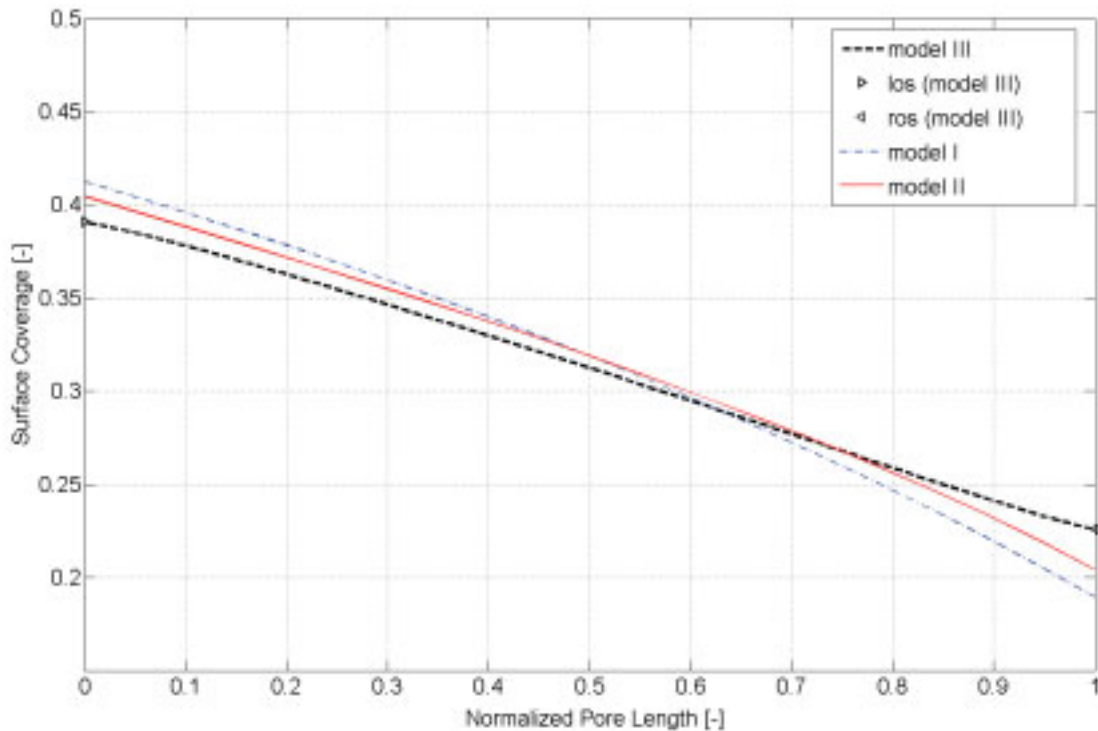


Figure 3.32: Surface coverage profiles for all the three models for the case $P_{left} = 30kPa$.

first case ($P_{left} = 30kPa$) it was 95.74%. That is due to the shape of the adsorption isotherm. Since the Langmuir adsorption isotherm is not linear, a constant pressure difference does not lead to a constant surface concentration gradient, thus leading to various surface flow rates.

Since the surface flow is low, the gas phase flow does not change much in magnitude along the pore (see fig.3.34d) even if it follows a similar behavior as in the previous case. Consequently, it may be said that if there is considerable surface flow, at least for the pore system investigated, the independent flow with adsorption equilibrium assumption is not representative anymore.

Back-calculation of the surface diffusion coefficient

It may be interesting to back-calculate the surface diffusion coefficient from the simulation results, assuming independent flows. Since independent flow with equilibrium assumption is commonly used in the literature, it may be useful to have an idea of the error involved employing it for such a system. The following common assumptions are made for such a calculation:

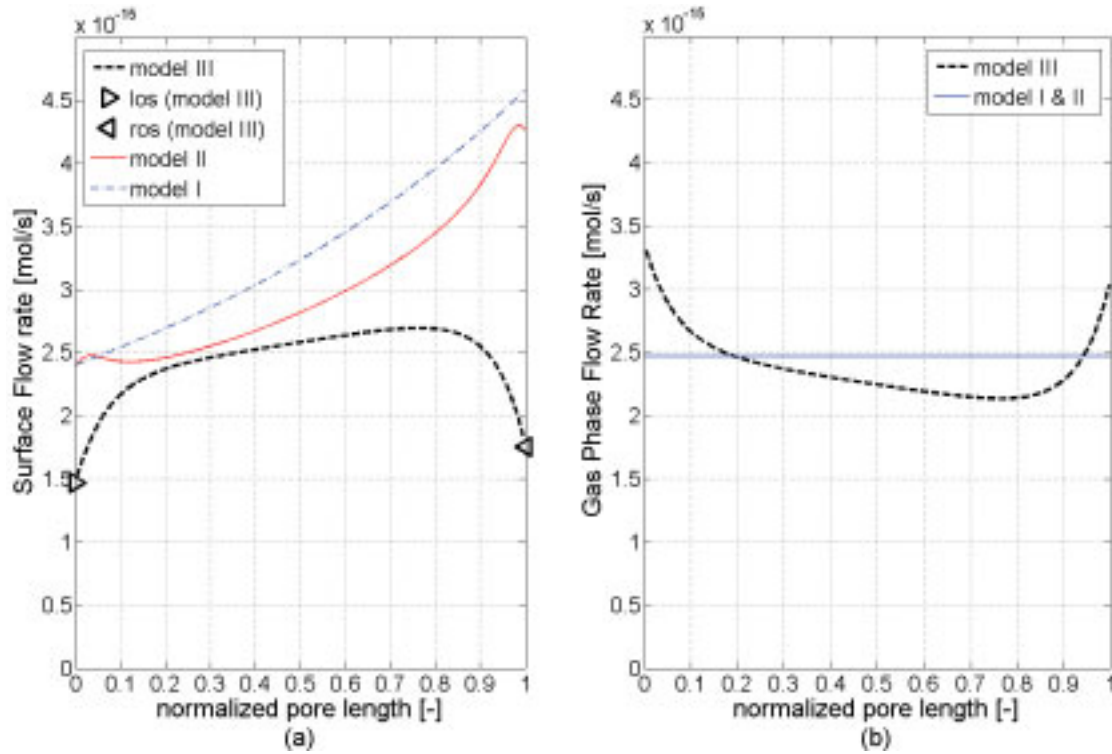


Figure 3.33: Comparison of flow rates for all the three models for the case $P_{left} = 30kPa$. (a) Surface flow rate profile. (b) Gas phase flow rate profile.

1. pure Knudsen flow in gas phase
2. surface flow and gas phase flow are independent and thus can be calculated independently
3. the pressure difference across the pore is small (20kPa)
4. the gas phase and the surface are in equilibrium

The flows are then simply

$$F^{total} = F^{gas} + F^{Surf} \quad (3.75)$$

where gas phase flow is constant due to constant pressure difference and has a value of $2.4678 \cdot 10^{-15} [mol/s]$ (based on *model II*) and the surface flow rate is defined by Fick's first law of diffusion as:

$$F^{Surf} = -D_A^{Surf} \cdot 2\pi r_{pore} \cdot \frac{dG_A}{dz} \quad (3.76)$$

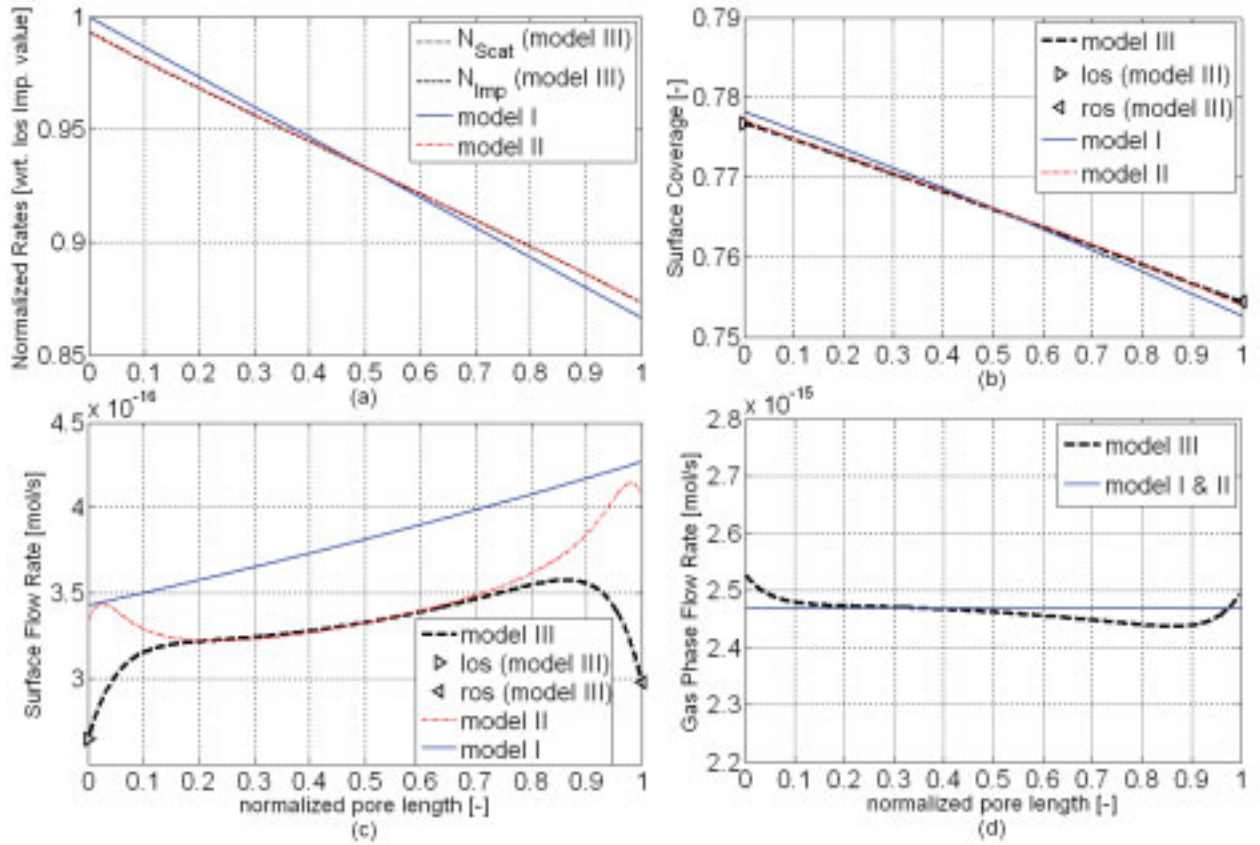


Figure 3.34: Various plots representing the behaviour of the $P_{left} = 150kPa$ case. (a) The impingement and scattering rate distribution (normalized by the impingement rate of the gas at a pressure of P_{left}) inside the pore. (b) Surface coverage profile. (c) Surface flow rate profile. (d) Gas phase flow rate profile.

Using the Langmuir adsorption isotherm, the dependence of surface concentration gradient on pressure gradient can then be calculated as:

$$\frac{dG_A}{dz} = G_{total} \cdot \frac{K_{eq}}{(1 + K_{eq}P)^2} \cdot \frac{dP}{dz} \quad (3.77)$$

since the pressure difference across the pore is small, the gradient can be replaced by the difference, and an average pressure can be used $P_{avg} = \frac{P_{left} + P_{right}}{2}$ in the denominator. Consequently, the surface diffusion coefficient can then be estimated by combining and rearranging Eqs. 3.76 and 3.77:

$$D_{est.}^{Surf} = \frac{-F^{Surf} \cdot (1 + K_{eq}P_{avg})^2}{2\pi r_{pore} \cdot G_{total} \cdot K_{eq} \cdot \frac{\Delta P}{L_{pore}}} \quad (3.78)$$

The relative value of the estimated surface diffusion coefficient in this way against the average pressure is plotted in fig.3.35.

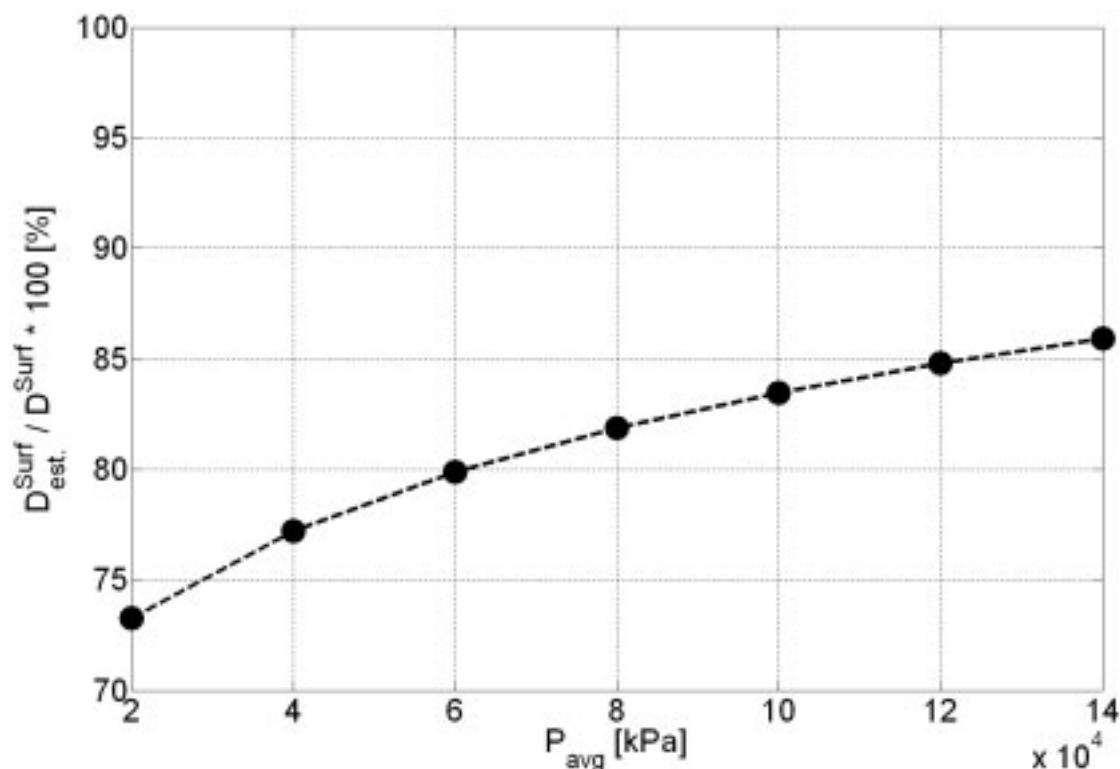


Figure 3.35: Back-calculated surface diffusion coefficient values. Estimated surface diffusion coefficients are normalized by the actually used surface diffusion coefficient and plotted against the average pressure inside the pore. The estimation involves the independent flow and adsorption equilibrium assumptions.

There are two important points that fig.3.35 leads to. First, the assumption of independent flows and adsorption equilibrium in this particular case leads to errors roughly between 15% and 25% in the surface diffusion coefficient. Second, the estimated surface diffusion coefficient values follow a definite path with respect to average pressure and may mislead to the rash conclusion that the surface diffusion coefficient is not constant but concentration dependent. It is already known that various experimental papers about surface diffusion conclude similarly, i.e., surface diffusion coefficients are concentration dependent. Now the question arises if such a conclusion is correct or it is merely a misconception being the result of the assumptions made. It should be noted that the system may behave differently for different values of parameters, such as surface diffusion coefficient, adsorption constant, mono-

layer loading, etc.. Thus, the results and discussion should not be taken to be describing the general behavior of all such systems. Therefore, it is not possible to give just one answer for such a question, instead one has to refer to the particular conditions.

3.2.5 Surface Diffusion as a Function of Surface Coverage

Another situation that may affect the behaviour of such a system, i.e., a pore under simultaneous Knudsen and surface flow, is the dependency of surface diffusion coefficient on the surface coverage. One of the most extensively discusses dependency is the Darken equation, which is identical to that of HIO model¹¹⁴:

$$D^{Surf} = \frac{D_0^{Surf}}{1 - \theta} \quad (3.79)$$

The system in the previous case (section 3.2.4) will now be simulated under surface coverage dependent surface diffusion coefficient. The equation system in such a case only needs to incorporate the non-constant surface diffusion coefficient into the finite difference calculations, namely into the surface flow rate calculation. A summary of the results from the simulations are tabulated in table 3.19.

Table 3.19, when compared with table 3.18, indicates that a (surface-) coverage dependent diffusion coefficient results in a higher enhancement of the total flow. This is due to the nature of the Darken equation (eq.3.79) where the D_0^{Surf} surface diffusion coefficient is divided by a value less than unity ($1 - \theta$). By that a higher value for the regional surface diffusion coefficient is achieved and consequently a higher surface diffusion flow appears.

The various plots for this system (fig.3.36) can also be compared with the previous case (figs.3.30-3.33)

In general, it can be noted that the behaviour shifted more away from the simpler models due to the increase in surface flow rate. The surface flow rate, surface coverage, gas flow rate, etc. profiles all show this slight shifting.

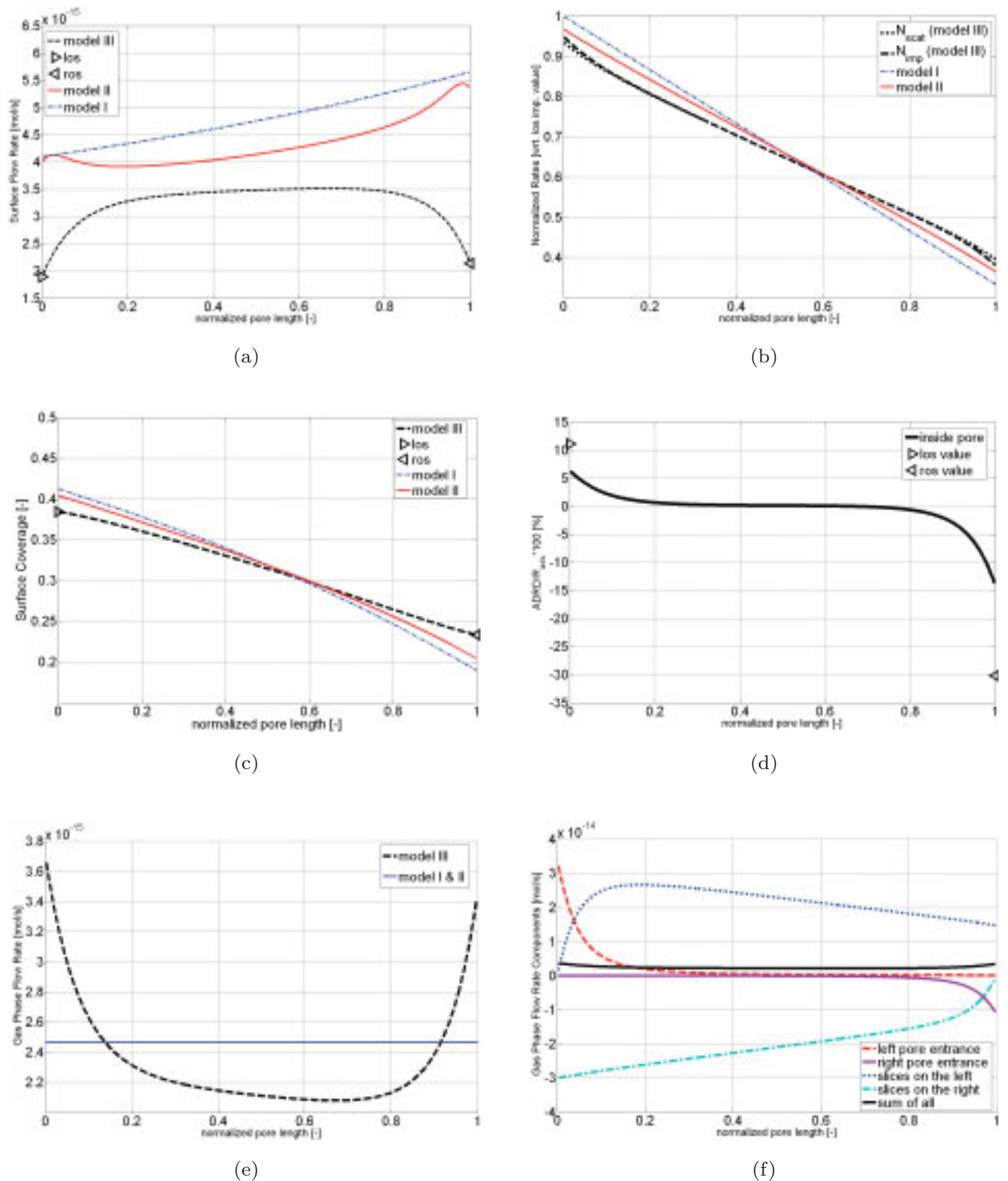


Figure 3.36: Various plots for the surface coverage dependent diffusion coefficient system, with $P_{left} = 30kPa$, $P_{right} = 10kPa$ and $D^{Surf} = \frac{D_0^{Surf}}{1-\theta}$. a) surface flow rate profile, b) impingement and scattering rates profiles, c) surface coverage profile, d) adsorption desorption rate difference profile, e) gas phase flow rate profile, f) profile for components that make up the gas phase flow.

Table 3.19: Total flow rate and flow enhancement with respect to sole Knudsen flow for a coverage dependent surface diffusion coefficient ($D^{Surf} = \frac{D_0^{Surf}}{1-\theta}$) case for $L/r_{pore} = 20$.

P_{left}^* [kPa]	F_{total} $10^{-15} \cdot [mol/s]$	Enhancement [%]
30	5.595	126.7
50	4.856	96.8
70	4.402	78.4
90	4.095	65.9
110	3.873	56.9
130	3.705	50.1
150	3.573	44.8

* $\Delta P = P_{left} - P_{right} = 20$ [kPa] in all cases.

Thus it can be said that a non-constant surface diffusion coefficient will also make the system more complicated.

The additional plot, provided in fig.3.36(f), shows the contributions of different regions of the system to the total gas flow in the pore. For example, it indicates for what length (into the pore) the molecules coming directly from entrances has effects on the total flow. It also gives an idea of the absolute flow of the molecules in the pore, that is to say how many molecules move from left to right and how many from right to left. One can say that molecules moving in the pore in one direction in this particular case is roughly ten times more than the net flow in the pore.

Back-calculation of the non-constant surface diffusion coefficient

The back-calculation of the diffusivity from these results may also help to give an idea of exactness of its estimation. Using similar assumptions as in the previous case (p.100), one can also estimate the D_0^{Surf} . But additionally one has to assume that surface coverage does not change appreciable and an average value of it can be used for the estimation.

A plot of actual surface diffusion coefficients and the estimated ones is

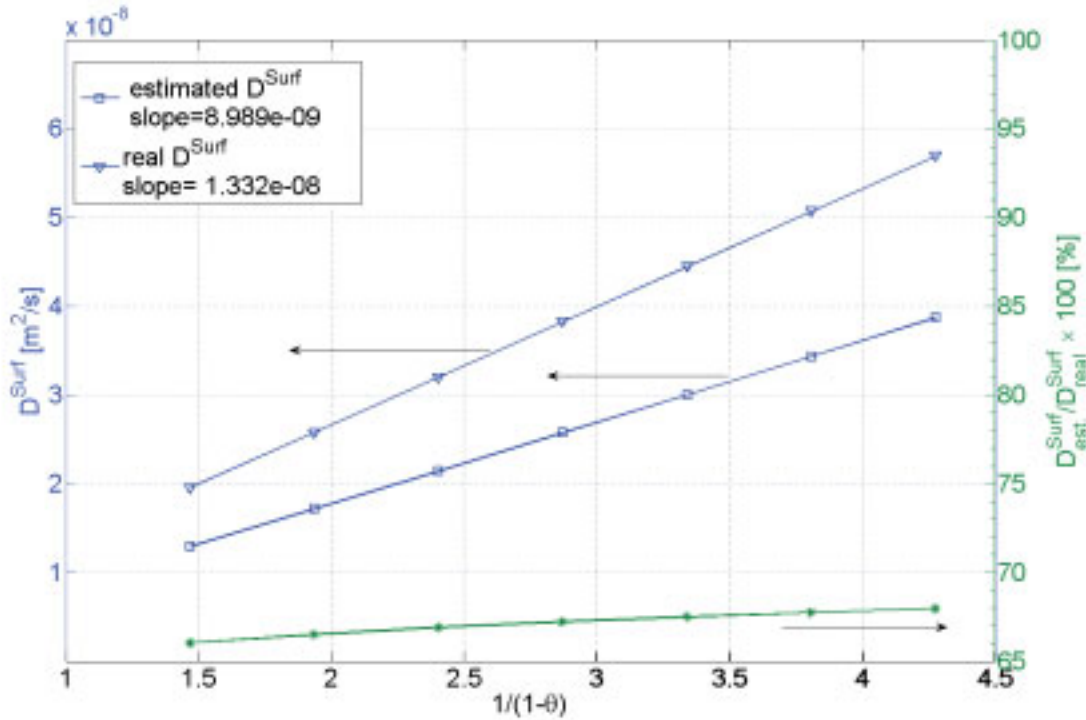


Figure 3.37: Back-calculated surface diffusion coefficient values along with the estimation errors for the non-constant surface diffusion coefficient case. The best linear fit to the estimated surface diffusion coefficient does not pass through the origin and results in slope and intercept of 9.189×10^{-9} and -6.346×10^{-10} , respectively (coefficient of determination $R^2 = 1$). Since it is known that the system behaves according to Darken equation, a linear fit passing through the origin is taken to be the representative fit, which also gives a very good fit to the data points (coefficient of determination $R^2 = 0.9995$).

given as a function of the $\frac{1}{1-\theta}$ in fig.3.37. On the same figure, the relative value of the estimated surface diffusion coefficient is also shown based on the second *y-axis*. Moreover, the data points are fitted to lines^{xxi} and the values for the slopes and the intercepts are given with the plot. Although an average of 35% error in estimation can be seen for individual points, the value of error in the estimation of D_0^{Surf} is more important. From the slope of fit for the estimated values, D_0^{Surf} is found to be 8.989×10^{-9} , which has a deviation of 32.5% from the actual value, 1.332×10^{-8} . This deviation is more than the case one achieves in a constant surface diffusivity case.

^{xxi}According to Darken equation (eq.3.79) a plot of $\frac{1}{1-\theta}$ vs. D^{Surf} should be a straight line passing through the origin.

It may be worth noting that for the constant diffusivity case, a linear fit passing through the origin to the estimated surface diffusion coefficients was not possible. The data obviously followed another nearly linear path^{xxii} with respect to $\frac{1}{1-\theta}$, which is not passing through the origin. If valid in general, such a behaviour could be taken as an indicator for the identification of systems with constant surface diffusion coefficient. For the moment, such a conclusion would be speculative and such systems should be studied more thoroughly.

Nevertheless, these results indicate that systems having surface flow and the behaviours therein are interesting and worth investigating.

3.2.6 Results for Other Pore Lengths and Pressures

To have a more general idea about the behaviour of the system at hand, two other pore lengths, $L/r_{pore} = 50$ and $= 80$, are simulated under same conditions (for both constant and non-constant surface diffusion coefficient cases). Additionally, another pressure difference ($\Delta P = 10kPa$) across all the pore lengths are investigated for the constant surface diffusion coefficient case. The results are tabulated and discussed below.

The results for new pore lengths using the previously investigated conditions (with constant surface diffusion coefficient) are given in table 3.20.

From table 3.20 (along with table 3.18) it can be seen that the enhancement rate follows a similar pattern for various pore lengths. For to the surface coverage and surface flow rate, the system gets more close to the simplified cases for longer pores. The molecules get a larger surface area to get onto the surface and thus can distribute themselves more homogeneously over the entire surface, not required to adsorb onto the surface in short distances. Nevertheless, as in the $L/r_{pore} = 20$ case, these two pore lengths show higher deviations from the simplified cases as the surface flow rate percentage gets higher.

The plot of the two extreme cases for the longest pore ($L/r_{pore} = 80$) can

^{xxii}The best linear-fit to the data points in that case was a line with the equation $D_{est.} = 6.454 \times 10^{-10} \frac{1}{1-\theta} + 8.824 \times 10^{-9}$, with a coefficient of determination $R^2 = 0.94$.

Table 3.20: Total flow rate and flow enhancement with respect to sole Knudsen flow case for $L/r_{pore} = 50$ and $= 80$ (with $D^{Surf} = const.$).

P_{left}^* [kPa]	$L/r_{pore} = 50$		$L/r_{pore} = 80$	
	F_{total} $10^{-15} \times$ [mol/s]	Enhancement [%]	F_{total} $10^{-15} \times$ [mol/s]	Enhancement [%]
30	2.239	104.7	1.460	107.0
50	1.764	61.2	1.142	62.0
70	1.534	40.2	0.991	40.4
90	1.405	28.4	0.906	28.5
110	1.326	21.2	0.854	21.1
130	1.274	16.4	0.820	16.3
150	1.237	13.1	0.797	13.0

* $\Delta P = P_{left} - P_{right} = 20$ [kPa] in all cases.

be seen in fig.3.38. For highest pressure (13% enhancement), the system behaves according to the simplifying assumptions, but again for lowest pressure (107% enhancement) deviations are seen.

For to the back-calculation of the (actually constant) surface diffusion coefficient, both longer pores behave similar to the previous case ($L/r_{pore} = 20$). The back-calculated surface diffusion coefficients are, respectively for $L/r_{pore} = 50$ and 80 , roughly between $88 - 94\%$ and $94 - 96\%$ of the actual one. But in this case, it can be seen that the error made in such an estimation becomes less and the estimated values get close to the real value as the pore length increases. But on the other hand, an apparent coverage dependency is still observed. The back-calculated values actually becomes better fits to Darken type dependency (i.e., $D^{est.} = f(\frac{1}{1-\theta})$) as the pore length increases ($R^2 = 0.950, 0.959$ and 0.978 , respectively, for $L/r_{pore} = 20, 50$ and 80). But an intercept at least one order of magnitude greater than the slope appears for all cases. This is actually an indication that the values do not follow Darken type relation, which is supposed to have no intercept value. In fact, it should be reminded once again that a constant surface diffusion coefficient was used and the assumptions in the back-calculation results in

this apparent coverage dependency.

Now, the simulations with the coverage dependent (according to Darken equation) surface diffusion coefficient for the the same conditions can be interesting for comparison. The results in question can be seen in table 3.21 (along with table 3.19).

Table 3.21: Total flow rate and flow enhancement with respect to sole Knudsen flow case for $L/r_{pore} = 50$ and 80 (with $D^{Surf} = \frac{D_0^{Surf}}{1-\theta}$).

P_{left}^* [kPa]	$L/r_{pore} = 50$		$L/r_{pore} = 80$	
	F_{total} $10^{-15} \times$ [mol/s]	Enhancement [%]	F_{total} $10^{-15} \times$ [mol/s]	Enhancement [%]
30	2.684	145.25	1.767	150.51
50	2.302	110.36	1.510	114.14
70	2.069	89.08	1.354	92.01
90	1.912	74.72	1.249	77.09
110	1.799	64.36	1.173	66.35
130	1.713	56.54	1.116	58.25
150	1.646	50.42	1.072	51.92

* $\Delta P = P_{left} - P_{right} = 20$ [kPa] in all cases.

The general behaviour is similar to the constant D^{Surf} case, the enhancement increases as the pore length increases and as the pressure decreases. The enhancement rates in this case is higher than the constant D^{Surf} case, since Darken equation serves to increase the regional value of the surface diffusion coefficient.

On the other hand, the fit to the back-calculation of the D^{Surf} values delivers a different behaviour. The error made in the estimation decreases as the pore length increases (back-calculated values are 66 – 68%, 84 – 85% and 89 – 90% of the actual ones for $L/r_{pore} = 20, 50, 80$). The degrees of fit to Darken type dependency are very good ($R^2 \approx 1$) and intercept values are at least one order of magnitude smaller than the slope. In these cases, one can also force to have the fits pass through the origin and get very good fit (with $R^2 \approx 1$ and slopes $8.99 \cdot 10^{-9}$, $1.13 \cdot 10^{-8}$ and $1.20 \cdot 10^{-8}$ that are approximately

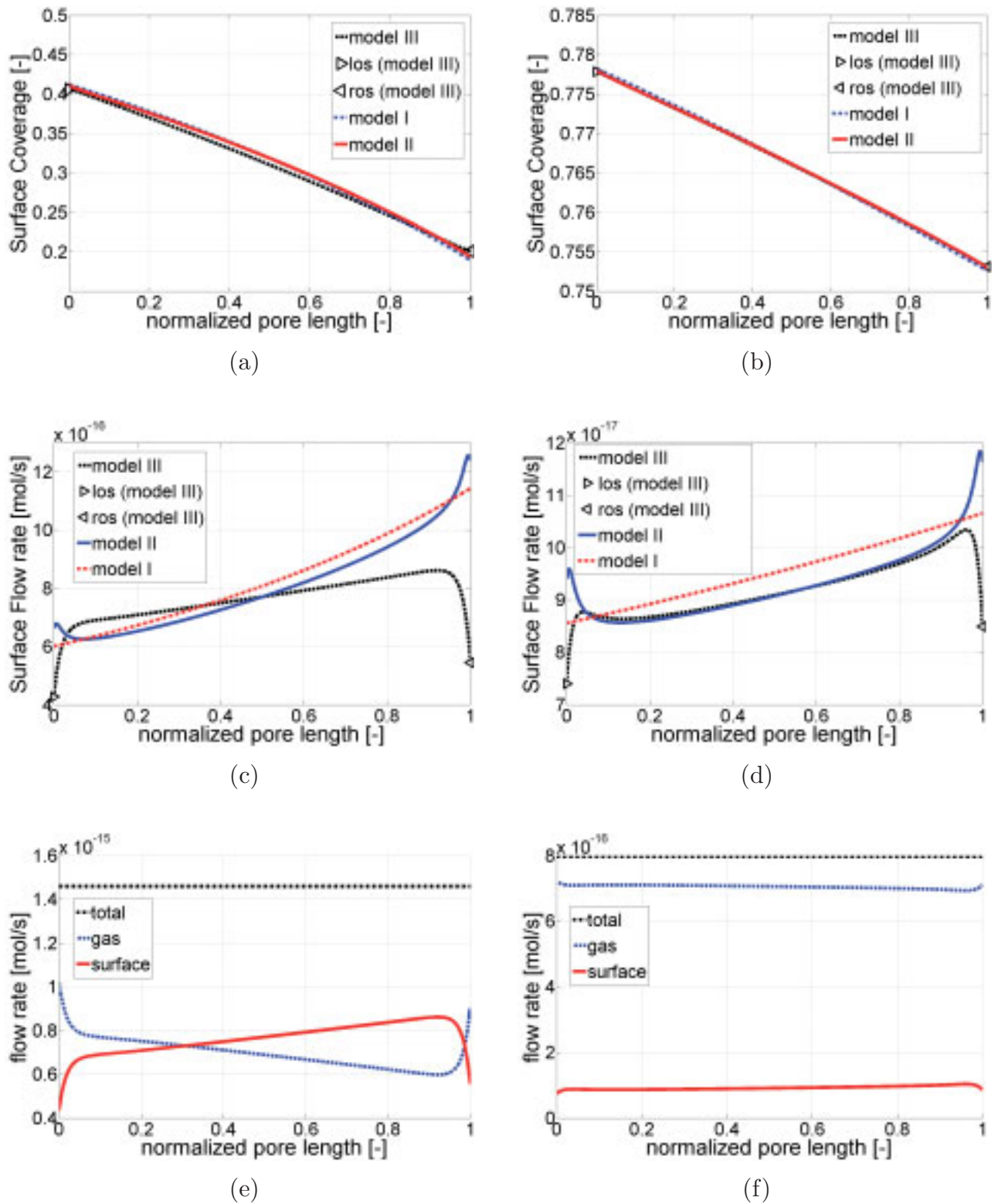


Figure 3.38: Various plots for the case $L/r_{pore} = 80$ with a constant surface diffusion coefficient. The left column is for the case $P_{left} = 30[kPa]$ and the right column is for $P_{left} = 150[kPa]$. a-b) comparison of surface coverage profiles with simpler models, c-d) comparison of surface flow rate profile with simpler models, e-f) flow rates profiles for *model III*. (P_{right} taken to be $20[kPa]$ lower than P_{left} .)

68, 85 and 90% of the actual value, respectively, for $L/r_{pore} = 20, 50$ and 80).

A smaller pressure difference across the pore ($\Delta P = P_{left} - P_{right} = 10$ [kPa]) for the same system ($D^{Surf} = const.$) also leads to similar results (see table 3.22).

Table 3.22: Total flow rate and flow enhancement with respect to sole Knudsen flow case for $L/r_{pore} = 20, 50, 80$ for $\Delta P = P_{left} - P_{right} = 10$ [kPa], with a constant D^{Surf} .

P_{left}^* [kPa]	$L/r_{pore} = 20$		$L/r_{pore} = 50$		$L/r_{pore} = 80$	
	F_{total} $10^{-15} \times$ [mol/s]	Enhancement [%]	F_{total} $10^{-15} \times$ [mol/s]	Enhancement [%]	F_{total} $10^{-15} \times$ [mol/s]	Enhancement [%]
20	2.586	109.6	1.207	120.6	0.788	123.5
40	2.030	64.5	0.921	68.4	0.597	69.3
60	1.758	42.5	0.788	44.0	0.509	44.3
80	1.606	30.1	0.715	30.7	0.461	30.7
100	1.511	22.5	0.671	22.6	0.432	22.6
120	1.449	17.4	0.642	17.4	0.414	17.3
140	1.406	13.9	0.622	13.8	0.401	13.7

The general behaviour of flow enhancement with respect to length to radius ratio and to pressure is kept. Respectively for $L/r_{pore} = 20, 50,$ and $80,$ the back-calculated D^{Surf} are 71 – 86%, 87 – 94% and 92 – 96% accurate and fit to Darken type equation gives again nearly linear results ($R^2 = 0.939, 0.932,$ and 0.934) with intercept values being at least one order of magnitude larger than slopes.

If we summarize the results from above, we can conclude that

1. Although the pressure difference, not the absolute values of the pressures on both sides, determines the gas flow rate for Knudsen flow conditions, addition of surface flow results in another behaviour. Under a constant pressure difference, the resulting total flow rate (Knudsen + surface flow rate) is neither constant nor has a simple linear dependency with pressure. Here, the nonlinear nature of the adsorption isotherm, namely the Langmuir adsorption isotherm, has the greatest influence.

2. The results indicate that if there exists appreciable surface flow rate, especially for shorter pores, the modeling using simplifying assumptions, such as adsorption-desorption equilibrium and the commonly used simple Knudsen diffusion coefficient, are not enough to mimic the behaviour of the system.
3. The back-calculation of the surface diffusion coefficient, D^{Surf} , using simplifying assumptions leads not to the actually used value. More importantly, for different pore lengths, different estimated values are achieved, this may lead to false predictions about the behaviour of the system.
 - Depending on the L/r_{pore} ratio, i.e., the geometry, one achieves different levels of accuracy at the estimation of the surface diffusion coefficient. This may lead to the false prediction that these systems have different surface diffusion coefficients although the same species, same surface at same conditions are investigated and in reality they enclose the same D^{Surf} .
 - A constant D^{Surf} may be estimated to be coverage dependent with such assumptions.
 - Both the results from the constant and coverage dependent (with Darken eq.) D^{Surf} are found to give good fits to $y = a \cdot \frac{1}{1-\theta} + b$. But only in the case of coverage dependent D^{Surf} , the b (intercept) value was found to be negligible. This difference in behaviours can possibly be used to differentiate between systems with constant and non-constant D^{Surf} , if similar assumptions were used for estimation.

Again, it should be noted that the results and the discussion presented here are based on a particular sample system and for a relatively small amount of conditions. For that reason, any general conclusion that could be drawn can only be speculative at the moment and the conclusions should not be thought to be the universal behaviour of all similar systems.

3.2.7 More General Case: Multi-Component Diffusion and Reaction in a Pore

A more general case, Knudsen diffusion and multi-component surface diffusion accompanied with surface reaction is also modelled similarly. Since the gas phase diffusion is of Knudsen type, each species can be handled separately in the gas phase. For the surface phase four different diffusion models are chosen:

1. each species diffuses independently with a constant D^{Surf}
2. each species diffuses independently with a D^{Surf} following Darken relation
3. species interact on the surface according to Maxwell-Stefan equations with a combined diffusion coefficient of $D_{ij}^{Surf} = \sqrt{D_i^{Surf} \cdot D_j^{Surf}}$
4. species interact on the surface according to Maxwell-Stefan equations with a combined diffusion coefficient of $D_{ij}^{Surf} = \left(D_i^{Surf}\right)^{\frac{\theta_i+\theta_j}{\theta_j}} \cdot \left(D_j^{Surf}\right)^{\frac{\theta_i+\theta_j}{\theta_i}}$

The four species; ethylene, hydrogen, ethane and nitrogen are taken as the diffusing species, and the hydrogenation of ethylene to ethane was the reaction on the surface. The hydrogenation is assumed to take place by reaction of adsorbed molecular ethylene and two adsorbed hydrogen atoms^{xxiii} on the surface.

Again, the data from table 3.16 is used for the porous structure properties. Other data concerning the four species and the system can be found in table 3.23.

The equation system for a reacting system can be deduced from the previous one by the addition of the reaction term into surface mass balance. That means, eq. 3.59 turns into the following equation:

$$N_{imp} = N_{scat} + \Delta F^{Surf} - R_{rxn} \cdot \vartheta \quad (3.80)$$

^{xxiii}Hydrogen is assumed to adsorb dissociatively. Care should be taken for dissociatively adsorbing species since the surface reaction rate and surface flow rate for them would be based on the atoms but the gas phase flow rate, impingement and scattering rates would be based on molecules of these species. Thus, one has to either multiply the F^{gas} , N_{imp} and N_{scat} with *two* or divide the F^{Surf} and R_{rxn} by *two* for consistency in equations using these rates simultaneously.

Table 3.23: Constants and parameters used for the simulation of the case multi-component diffusion and reaction.

	C_2H_4	C_2H_6	$H_2/H-$	N_2	
P_{left}	23	6	18	53	[kPa]
P_{right}	16	13	14	57	[kPa]
M_w	28.05	30.07	2.01	28.01	10^{-3} ·[kg/mol]
σ_{LJ}	4.163	4.443	2.827	0	10^{-10} ·[m]
K_{eq}	$2 \cdot 10^{-5}$	$2 \cdot 10^{-7}$	$3 \cdot 10^{-6}$	0	[1/Pa]
s_{coef}	1	1	1	0	[-]
λ_{ads}	1	1	2	0	[-]
D_j^{Surf}	15	1	23	0	10^{-10} ·[m^2/s]
δ_j	1	0	2	0	[-]
ϑ_j	-1	+1	-2	0	[-]

where s_{coef} is the sticking coefficient, λ_{ads} indicates the type of adsorption (1 : molecular, 2 : dissociative), δ_j is the reaction orders for the surface reaction (wrt. surface species) and ϑ_j is the stoichiometric coefficients of the surface species in the surface reaction.

where

$$R_{rxn} = 2\pi r_{pore} \Delta z \cdot k_{rxn} \prod_{j=1}^n (G_{total} \cdot \theta(j))^{\delta_j} \quad (3.81)$$

The reaction rate defined in eq.3.81 is based on a Langmuir-Hinshelwood type model, i.e., reaction between adsorbed species, but the idea of Eley-Rideal mechanism is also easily integrable into the modeling. It should be noted that only surface reaction step should be considered in the reaction rate equation here. The adsorption and desorption equilibrium constants, which are normally used to estimate the surface coverages in a Langmuir-Hinshelwood model, are not needed for this calculation directly.

Since the eq.3.59 is now turned into eq.3.80, eq.3.60 should also be modified:

$$(N_{scat})_{n \times j} = \left(\check{f}_{n \times n} - I_{n \times n} \right)^{-1}. \quad (3.82)$$

$$\left(\Delta F^{Surf} - (R_{rxn})_{n \times 1} \cdot \vartheta_{1 \times j} - (\check{g})_{n \times 1} \cdot (N_{z=0}^{lr})_{1 \times j} - (\check{g}_{flipped})_{n \times 1} \cdot (N_{z=L}^{rl})_{1 \times j} \right)$$

Moreover, the eq.3.62 is no more valid for reacting species and has to be modified accordingly:

$$F^{total} \neq const., \quad F_i^{total} = F_i^{gas} + F_i^{Surf} = F_0^{gas} + F_0^{Surf} - \vartheta \sum_{k=1}^i R_{rxn}(k) \quad (3.83)$$

Note that the index i in eq.3.83 does not denote the species but the corresponding position (right-boundary of the slice) in the pore.

The following equations are also to be modified: eq.3.65 into eq.3.84 and eq.3.66 into eq.3.85.

$$0 = \sum_{row=1}^n \left((N_{imp})_{n \times j} - (N_{scat})_{n \times j} + (R_{rxn})_{n \times 1} \cdot \vartheta_{1 \times j} \right) \quad (3.84)$$

$$+ R_{ads,los} - R_{des,los} + R_{ads,ros} - R_{des,ros} + R_{rxn}(los) + R_{rxn}(ros)$$

$$(r_{ads,0} - r_{des,0}) \cdot A_{solid/pore}^{face} + R_{rxn}(los) = F_{A,0}^{Surf} \quad (3.85)$$

Although for constant and Darken type D^{Sru} the calculation of surface flow is already straight-forward, it has to be calculated differently in the case of Maxwell-Stefan equations. The Maxwell-Stefan F^{Surf} is calculated as:

$$F^{Surf} = -G_{total} \cdot 2\pi r_{pore} \cdot [B^{Surf}]^{-1} \cdot [\Gamma] \cdot \frac{\Delta\theta}{\Delta z} \quad (3.86)$$

where

$$B_{ij}^{Surf} = \begin{cases} \frac{1}{D_i^{Surf}} + \sum_{\substack{j=1 \\ j \neq i}}^n \frac{\theta_j}{D_{ij}^{Surf}} & , \text{ for } i = j \\ -\frac{\theta_i}{D_{ij}^{Surf}} & , \text{ for } i \neq j \end{cases} \quad (3.87)$$

and

$$\Gamma_{i,j} = \delta_{ij} + \frac{\theta_i}{\theta_{free}} \quad (3.88)$$

with

$$\delta_{i,j} = \begin{cases} 1 & : i = j \\ 0 & : i \neq j \end{cases} \quad (3.89)$$

Using the above equations, the equation system is set up and programmed by Matlab similar to the previous case. Before-hand, it should be noted that the equation system with its new multi-component, reacting and, as the case maybe, coupled surface flow nature has become much more different than previous one. The equation system is much more complex and larger, and also the parameters values are more dependent on each other. Furthermore, the interdependence of the parameters is much more sensitive to minor changes. These properties make the system instable and harder to solve. Actually, for various conditions (i.e., pore lengths, pressures, physical constants, etc.) used, only a sample system with $L/r_{pore} = 2$ and $k_{rxn} = 100 [m^2/mol^2/s]$ (see also table 3.23) is found to converge to a solution with the solution method. The system obviously requires special solvers and methods.

Some results from the sample solution are chosen and given here starting with fig.3.39. The four different species, because of different physical constants, show different behaviour. Nitrogen is assumed not to adsorb, so it is under sole Knudsen diffusion. Ethane is assumed to adsorb weakly and also is given a small surface diffusion coefficient, thus it has less tendency to play a big role on the surface. The low adsorption constant assures that it is released into the gas phase easily as it is produced on the surface. Ethylene

adsorbs most strongly, and also can diffuse on the surface relatively good. Hydrogen, on the other hand, adsorbs dissociatively and has the highest surface diffusion coefficient. Therefore, one gets a glimpse of various possible situations.

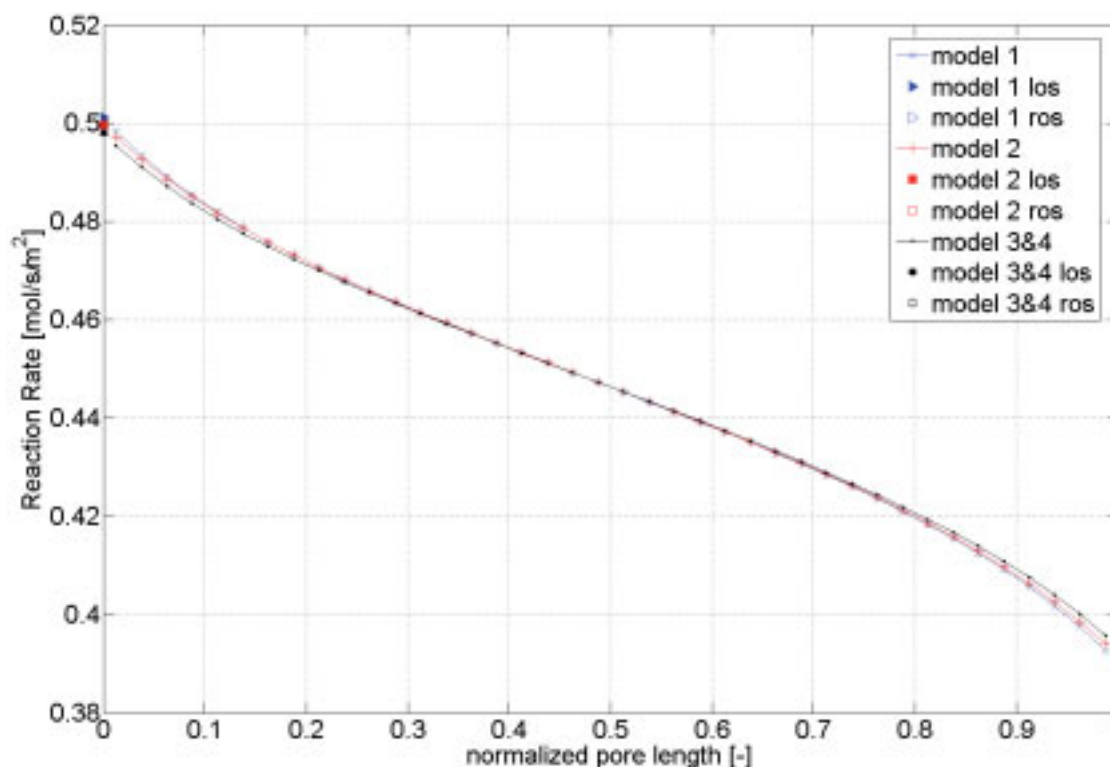


Figure 3.39: Reaction rate profile inside the pore for the case Knudsen diffusion and multi-component surface diffusion accompanied with surface reaction.

For example, the reaction rate profile in the pore is given in fig. 3.39. In general, *model 3* and *model 4* gave very similar results and thus are indicated together in the following figures. As can be seen in the figure, the reaction rates for all the models follow only a slightly different path.

Looking at the shape of the H_2 coverage (fig. 3.40) and its reaction rate order, the shape of the reaction rate profile can be better understood. Although the percentage deviation from the equilibrium curve is small, the behaviour of deviation (i.e., the shape of the resulting curve) is most interesting. When compared with the other surface species, this behaviour can be attributed to hydrogens relatively higher surface diffusion coefficient. The C_2H_4 profile, on the other hand, is nearly linear, changing between 0.26 to

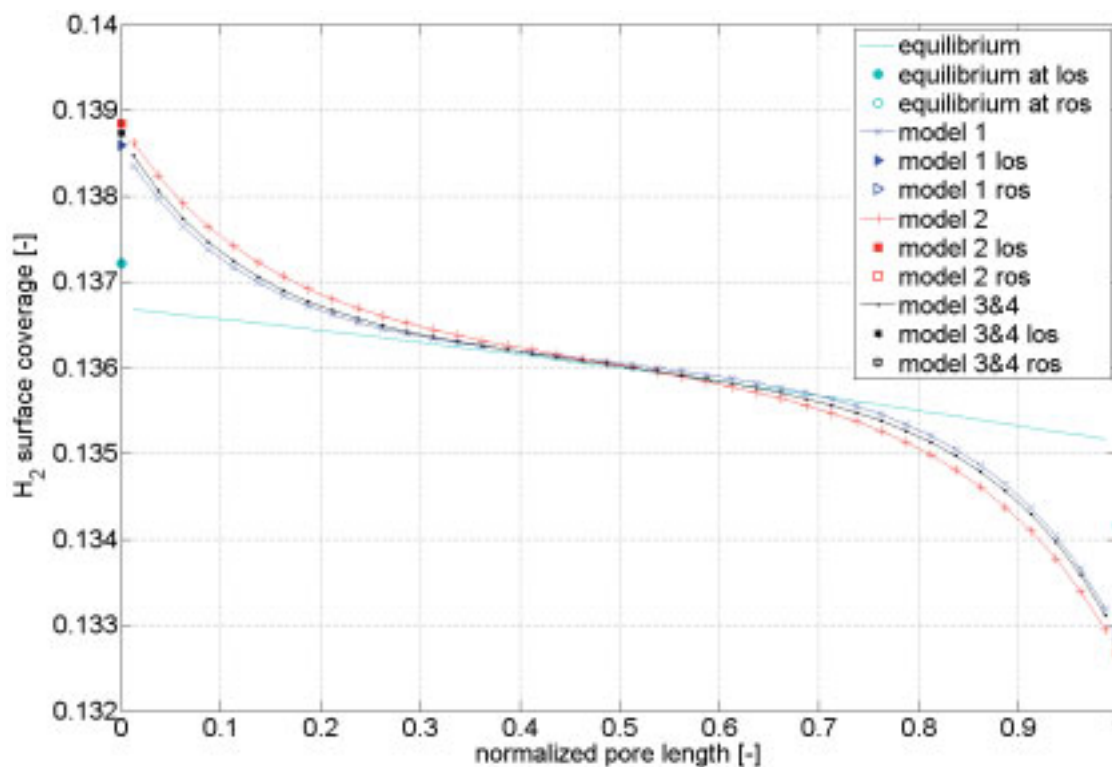


Figure 3.40: H_2 surface coverage profile for the case Knudsen diffusion and multi-component surface diffusion accompanied with surface reaction.

0.22. And as expected, C_2H_6 hardly adsorbs and has an average of 0.0012 surface coverage with again nearly a linear distribution with the exception of the two last slices at both ends of the pore.

Figure 3.41 indicates that the surface flow rate of ethylene is comparable with its gas phase flow rate. Roughly 13% of the total flow in the pore is due to the surface flow (it was around 2% for H_2 and roughly less than 1% for ethane). It can also be noticed that although the gas phase flow rates for *models 2* and *3* are similar, their total flow rates are different due to their different surface flow rate models. Since the reaction rate profiles for all models are similar (see fig. 3.39) and their gas phase flow rates are also close to each other, the only reason for the change in the surface flow rate (and consequently in the total flow rate) can be the various surface diffusion models. The surface flow rate of *model 3* is higher than the other two models, which assume independent surface flows. Therefore, it can be said that the surface flow of *hydrogen* serves to enhance the surface flow of *ethylene* in this particular case (and also vice versa).

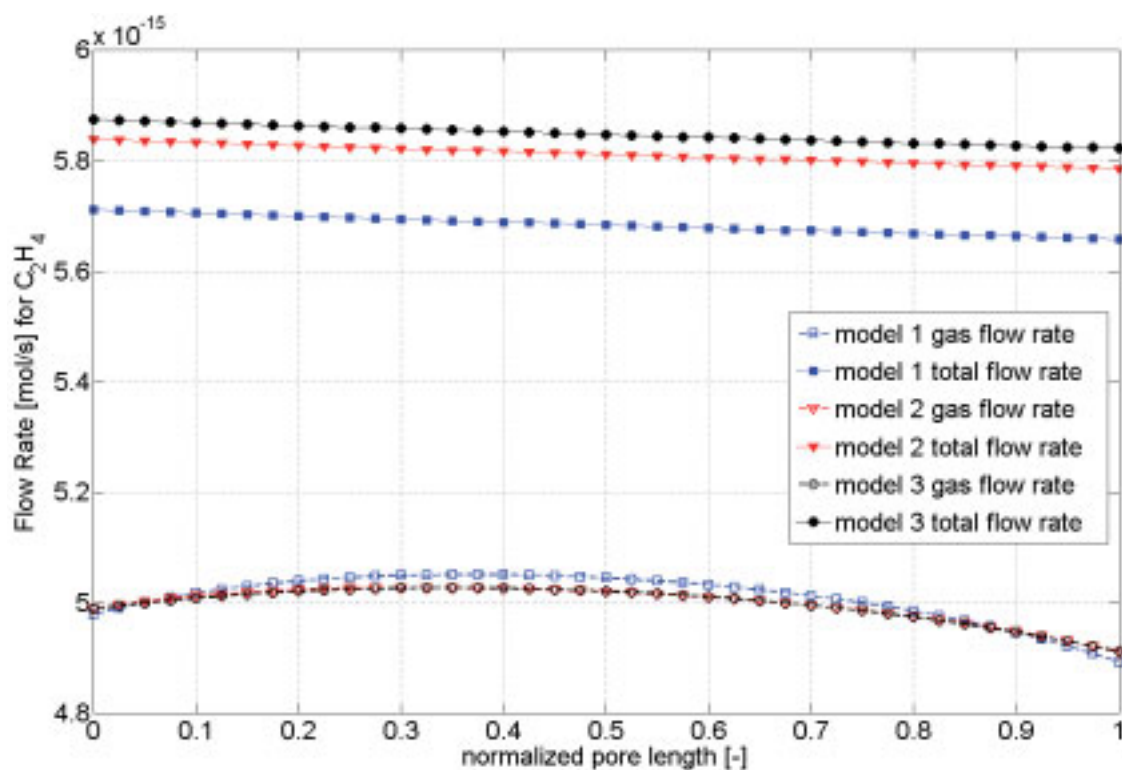


Figure 3.41: C_2H_4 gas and total flow rate profile for the case Knudsen diffusion and multi-component surface diffusion accompanied with surface reaction. *Model 4* results are nearly indistinguishable from *model 3* and thus are not shown.

Another interesting plot, figure 3.42, shows the ADRD profiles of different species for *model 1*^{xxiv}. At first glance, it can be noticed that different species behave very differently as far as the ADRD is concerned. The product of the reaction, C_2H_6 , has nearly throughout negative ADRD. This indicates that it is desorbed, which could already be expected. Only at the entrance of the pore it is adsorbed, from where the adsorbed and produced ethane are transported deeper into the pore with surface diffusion, and then desorbed. The reactants, on the other hand, have net desorption on the entrance (*left*-) side of the pore. Although the reaction rate is higher on this part of the pore and they are consumed, they still have a surplus of supply and consequently desorb. This supply comes from the outer-surface of the pore. As can be seen in the figure, the outer-surface has a positive ADRD, indicating a net adsorption of the reactants. Since, the surface area of the outer-surface is larger (when compared to the pore slices), the adsorbed amount on this

^{xxiv}*Model 1* is chosen as an example, but all the other models behave also very similarly.

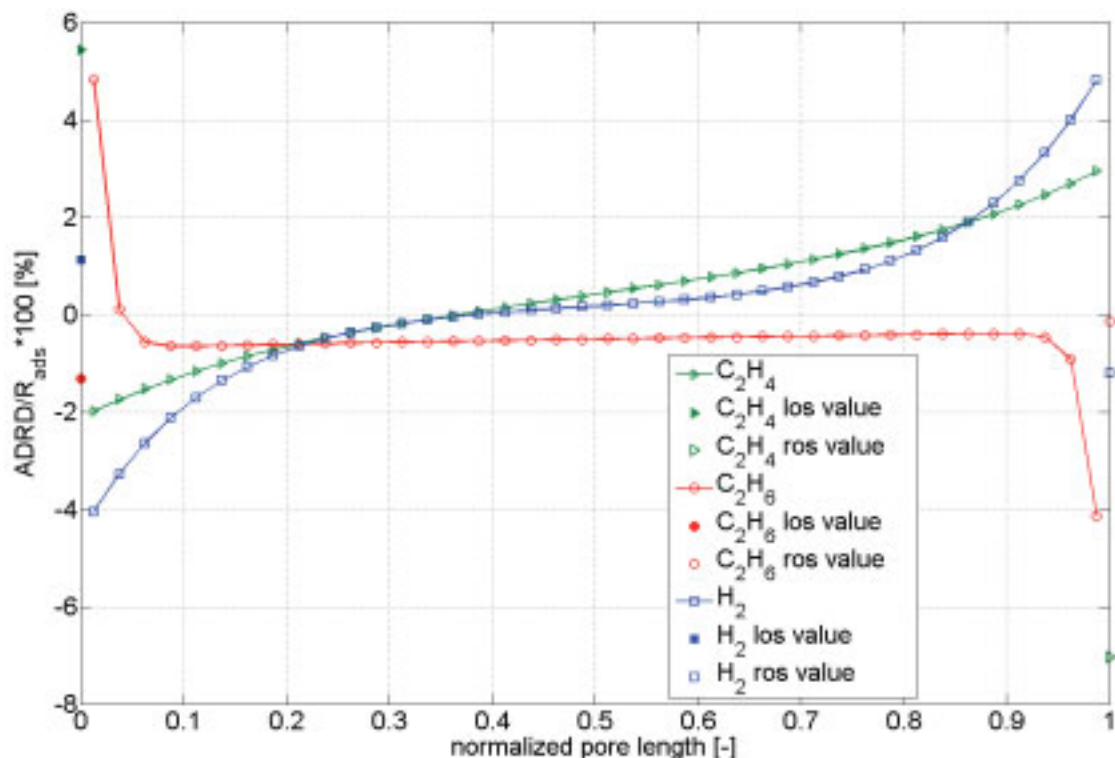


Figure 3.42: ADRD profiles for C_2H_4 , C_2H_6 and H_2 from *model 1* for the case Knudsen diffusion and multi-component surface diffusion accompanied with surface reaction.

surface is enough to keep a net desorption for a certain distance into the pore. It should be noted that the rate of reaction is very small relative to the total supply of reactants (i.e., the flow rate). For example for *model 1*, the conversion of ethylene through the pore (excluding outer-surfaces) is around 1% (see fig.3.41). This may also be the reason of such a behaviour. Nonetheless, the system is very interesting as it is very complicated with its various physical constants and simultaneously occurring phenomena.

Shortly, it can be said that such systems where many phenomena simultaneously occur, have diverse and interesting behaviour. Therefore, this part of this study, where only some sample systems are investigated, should not be considered to lead to concrete conclusions about such systems. On the contrary, it serves to create many more questions about the modeling of these systems and about the complex behaviour that can be exhibited. The only conclusion one can derive from these results is that the modeling with these novel approaches: using *outer-surfaces*, *projection approach* and mod-

eling *without adsorption-desorption equilibrium*, leads to reasonable results that can be theoretically and logically supported. Moreover, these results and some phenomena cannot be achieved with conventional modeling, where some of the assumptions used are suspected to shade them off. Consequently, it can be said that extensive research should be made to exploit the diverse behaviours of such systems, and the novel approaches developed here could be used as an aid for this purpose.

Part IV

Epilogue

“Yeri geldimi, az ve öz konuşmak, destanlar yazmaktan daha etkilidir...”

“At the right moment, talking succinctly is more powerful than writing an epic...”

4

Summary

In short; a realistic diffusion system, multi-component diffusion, accompanied by a relatively simple reaction, a single reaction with simple molecules, is investigated using commercial pellets at mild conditions. The motivation was to elucidate the effect of pore structure for simultaneous diffusion/reaction systems in general. Modeling of such systems was first reviewed using simple and complicated pore models, and their results have led to the development and introduction of a novel approach, the *projection approach*. It is novel basically in two aspects: first, due to its architecture some commonly used assumptions can be avoided, and second, it makes use of new concepts and incorporates them by a new calculation procedure. It can be concluded that the results from both experimental studies and modeling stimulate the thirst for further research.

The kinetic studies with the turbo-reactor points out that even a reaction with simple molecules and stoichiometry can have versatile behavior

when it comes to heterogeneous catalysis, that is when the surface comes into play. The probe reaction, hydrogenation of ethylene, showed various phenomena: such as dependence of reaction orders on concentration and operating conditions, and decrease of reaction rate with increasing temperature. Additionally, in the single-pellet reactor, some oscillatory behavior has also been observed. In fact, this behavior can be and was avoided by changing the operating conditions. But then the following questions should eventually be answered: “would one really want to avoid this behavior?” or “how can one incorporate such phenomena in the modeling and understand them, and then perhaps make use of them in real reactors?”. Answering these questions is not in the scope of this work, and thus it is left open for further research. Moreover, elucidating the real reaction mechanism and determining all the kinetic phenomena were not the reason behind these experiments. A satisfactory representation of the reaction kinetics by fitting a mathematical model-equation to the acquired data was the main objective. Therefore, various models are tried and the best fitting one has been chosen. It is interesting to note that the best model showed a dependence of reaction rate also on the amount of product.

To collect information about the concentration profile inside pellets, a single-pellet reactor was used. Valuable information has been collected from these experiments. Similar pellets with different pore-size distribution have shown different distribution of concentrations, as expected. An optimum pore-size distribution, e.g., based on reaction rate, can therefore be determined from the results. The response of the center-chamber concentration to the change of the conditions are also found to be different for different pellets. As a result, one cannot talk about a globally optimum-pellet, but an optimum depending on the particular operating conditions. The results from the experiments can also be used to find whether the whole surface area of the pellet is utilized for the reaction. A step-wise approach to the state where one of the reactant's concentration diminish in the center-chamber designate the point of “just” total utilization of catalyst. Beyond that point lies the undesirable case, where some of the precious catalyst material does not catalyze the reaction due to lack of reactants. A note should be made

here also about nitrogen, the inert component. In such a system, the common expectation for nitrogen would most probably be that it had to have a constant concentration throughout the pellet. Contrary to that expectation, in all the experiments nitrogen was observed to build a concentration gradient as a result of the multi-component interactions. All of these pieces of information are vital for testing the efficiency of utilization of catalytic pellet and the accuracy of one's modeling. In general, a realistic model should be able to mimic these findings from such experiments. Noting that the gathering of such information about reaction-diffusion systems is peculiar to the single-pellet reactor, it follows that this reactor type deserves its respectable place among experimental reactors.

On the other hand, emphasis is given to theoretical modeling. Initial work in modeling has shown that a 3-D pore model is not superior to a much simpler 2-D model, both having similar deficiencies in representing experimental data. This has led to question the completeness of the modeling and of the validity of the general assumptions used. As a result, the addition of surface diffusion and consequently the utilization of the adsorption-desorption equilibrium assumption utilized with it (in other words, the independent flow assumption) are reviewed. Also the Knudsen flow is discussed in more depth than common approach. It has been shown that a throughout adsorption-desorption equilibrium is theoretically not possible. Mass balance between the gas phase and the surface face requires a net exchange between these two phases, only then a surface flow can be sustained. Consequently, overall equilibrium between gas and surface cannot be the reality for these systems, it may only be used as a simplification and/or approximation of the actual non-equilibrium case. Moreover, the extensive review of the Knudsen flow has also shown that the chemical engineering version of Knudsen flow is oversimplified. The commonly used formula is valid only for very long pores, and does not incorporate many characteristics of this type of flow. Knowing that the pores in catalyst pellets are short and their spatial distribution has an effect on the transport/reaction in pellets, one needs to reformulate the incorporation of Knudsen flow to the modeling.

Based on the above points, a novel approach for modeling and calculating

Knudsen flow in pores is developed and introduced. This approach, called the *projection approach*, makes use of the geometrical properties of the Knudsen's cosine-law of reflection. It is then combined with the finite difference approach, and the pure Knudsen flow in pores and its characteristics are reproduced accurately with controllable precision. Later, various pore lengths and pressures were investigated with this model under simultaneous surface diffusion and Knudsen flow. Another new concept introduced here was the use of the so named *outer surface area*, which was then used to determine the boundary conditions for surface flow. The results emphasize that if there is appreciable surface flow, the equilibrium assumption is not a satisfactory simplification any more. The case, non-constant surface diffusion coefficient, has also been investigated under similar conditions.

From the results of the surface and Knudsen diffusion modeling, surface diffusion coefficient was back-calculated using commonly used assumptions. The back-calculated value and the used (actual) value were then compared to have an estimate of the error associated in using these assumptions. It is shown that for the investigated conditions this had led to seemingly concentration dependent surface diffusion coefficients although a constant value was used. For smaller pores the error was found to be larger. A fit to the back-calculated values has shown that for an actually constant diffusion coefficient a Darken type fit had been achieved, but it did not lead to a line passing through the origin. This was not the case for an actually concentration dependent coefficient, which can possibly be used to differentiate between these two systems when analyzing data from experimental systems. Nevertheless, extensive research is required for reaching concrete conclusions about these points.

Finally, a surface reaction was added to the model, and a sample system was simulated. In this case, a multi-component system was simulated, and various models for multi-component surface diffusion were also tried. The resulting system of equations for the this multi-component reacting case turned out to be much more sensitive to parameter values, and seemed to require utilization of special solvers or algorithms. On the other hand, as the system became more and more complex, the behavior of different species became

more and more diverse and different from each other, making such systems and their appropriate modeling more attractive from scientific point of view.

Shortly, it can be claimed that the developed approach and modeling is convincing about its accuracy and potential. It allows for otherwise suppressed phenomena to take force and affect the behavior of the system. Moreover, it can be used to estimate the errors made in using common assumptions. In either case, only extensive research can help to identify its ultimate limits of application.

“Sonraki adımları planlamak, amaca ulaşmanın en kısa ve emin yoludur...”

“Planing your next steps, is the shortest and safest way of reaching the target...”

5

Future Aspects

From the experimental point of view, selection of another simple reaction is advisable. Although the hydrogenation of ethylene is the most basic hydrogenation reaction involving very simple molecules, its kinetics is very complicated. In order to see a more pronounced effect of the pore structure on diffusion/reaction, one needs to investigate using a less versatile kinetic behaviour. On the other hand, investigation of these interesting properties of the ethylene hydrogenation and its modeling can itself be the subject of another study.

In this study, different pore structures are compared under the same operating conditions and flow composition, changing only the temperature. Another interesting approach can be alternating the reactant compositions under the same operating conditions for various pellets, and observing their response.

Additional adsorption experiments can be performed to determine the

adsorption constants for the various species involved. This may be valuable if the kinetics for the reaction represents the actual mechanism. If so, the adsorption coefficients from kinetic measurements and from the adsorption measurements can be used to cross-check each other.

In general, the utilization of an inert gas is a good idea both from practical and theoretical points of view. Not only it helps to control the reaction rate by diluting the mixture and thus preventing possible temperature gradients inside the pellet, but also its concentration profile serves for the understanding of the interaction between diffusing species and a check for the accuracy of modeling.

From a theoretical point of view, the new approach and modeling has to be used for various systems. Various pore lengths, different species under different conditions should be simulated. Also it should be accompanied with traditional modeling of the same system, and thus serve to indicate the differences inbetween. Only then one can make generalizations about the use of these common assumptions: under which circumstances one may use these assumptions, and under which one may not.

A special solver is required for the projection approach with surface reaction. If such an algorithm is found, then the experimental data acquired in this work can be compared with the simulations from this approach and the traditional modeling.

The first trial should be the simple parallel pore model for the reacting case. If one can find a bi-disperse pore structure, where the large pores have ordinary diffusion and the small pores have Knudsen diffusion, it will be most easy to incorporate the projection approach for the smaller pores. In such a case, the smaller pores will be under symmetric pressure on both sides. The guidelines for calculating a pore under symmetric pressure, and also a closed-end pore, using projection approach are given in the appendix. The modeling of large pores can be made with traditional flow equations but again without making the assumption of equilibrium and be compared with the case having the assumption.

The projection approach can also be adopted to 3-D pore networks. As

a starting point, the nodes where the individual pores are connected to each other, can be assumed to have ordinary distribution of molecules, i.e., back to cosine distribution. That will be a good estimation if these nodes have a larger diameter than the pore, where the Knudsen number corresponds to the ordinary diffusion value. On the other hand, if a definite shape (say spherical) can be assigned to these nodes, one can easily discretize the surface and use the projection approach to calculate for the distribution of incoming molecules into the spatially distributed pores.

Actually, one can start with a much simpler case, that is, two pores under Knudsen flow conditions connected by a spherical node (also under Knudsen flow conditions). One can then alter the relative position of the pores with respect to each other and calculate the corresponding transmission probability for each configuration and compare these results, e.g., with Monte-Carlo simulations from the literature.

One can also try to apply the idea of projection approach to, for example, an elbow or other shapes. In such cases, the elbow for example can be divided into finite elements and the interaction of finite elements with each other can be modeled. The bottle neck for such a geometry will be the computational power one will have in his service.

Part V

Supplementary Part



Appendix

A.1 Calculation procedure for \check{F}

A sketch of the coordinate system, sphere and cone are given in fig.A.1a.

The equations describing, respectively, the sphere and the cone are:

$$x^2 + y^2 + (z - r_s)^2 = r_s^2 \quad (\text{A.1})$$

$$y^2 + \left(z - \frac{r_c}{h} \cdot x\right)^2 = \left(\frac{r_c}{h} \cdot x\right)^2 \quad (\text{A.2})$$

The intersection curve between the sphere and the cone can then be found by equating the above two equations. The resulting formula for z is then:

$$z_{int} = \frac{x_{int}^2}{2r_s - 2 \cdot \frac{r_c}{h} \cdot x_{int}} \quad (\text{A.3})$$

The above equation is defined only for $0 \leq x_{int} \leq x_{max}$, and the y_{int} equation

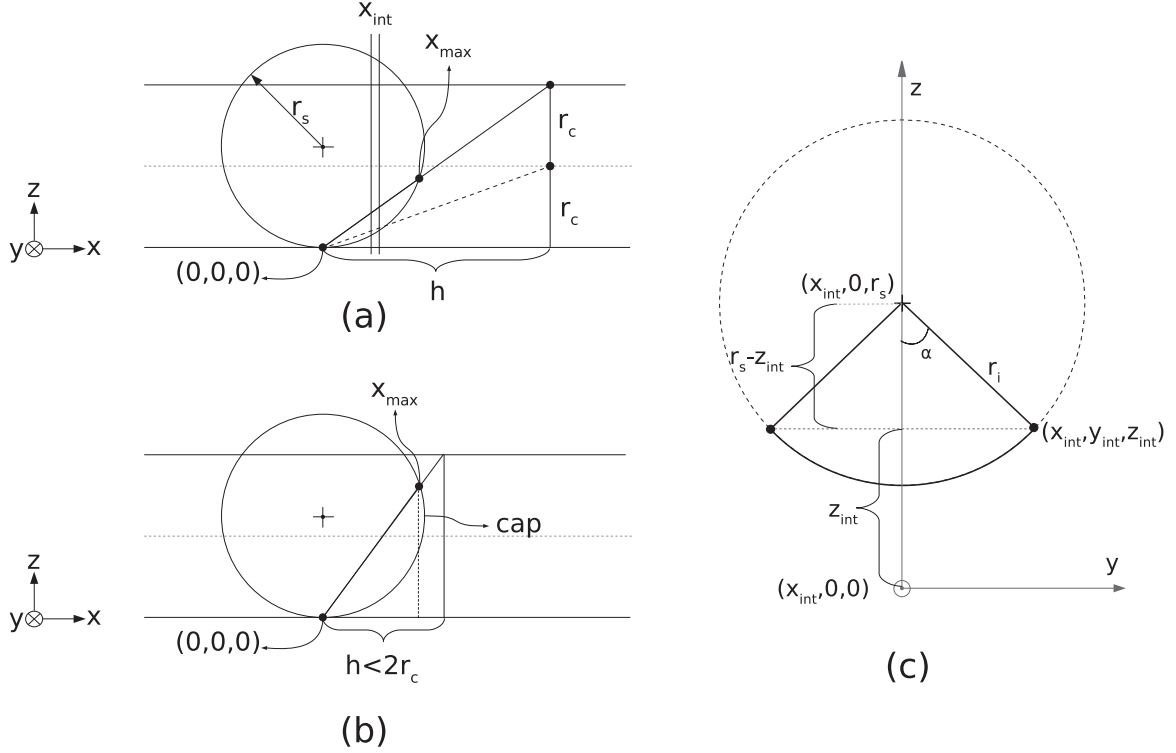


Figure A.1: Auxiliary figures for the calculation of the projection area in \check{F} calculation. (a) Sphere, cone and the origin of the coordinate system used, (b) the cap built on the right of the x_{max} if $h < 2r_c$, (c) the arc built on the sphere at the plane x_{int} .

(parameterized with respect to x) can be found by inserting the above equation into eq.A.1. The value for x_{max} can be found by using similar triangles in fig.A.1a as:

$$x_{max} = \frac{h}{2r_c} z_{int} \quad (\text{A.4})$$

after inserting eq.A.3 and rearranging, one gets:

$$x_{max} = \frac{4r_c r_s}{h + \frac{4r_c^2}{h}} \quad (\text{A.5})$$

If one takes a slice at an x_{int} , as seen in fig.A.1a, one gets an arc on the sphere on the y-z plane (fig.A.1c). The r_i in the figure is the radius of the circle cut from the sphere at x_{int} . It is defined as (from the equation for the sphere, i.e., eq.A.1):

$$r_i = \sqrt{r_s^2 - x_{int}^2} \quad (\text{A.6})$$

The cosine of the angle α that subtends the half of the arc is then:

$$\cos(\alpha) = \frac{r_s - z_{int}}{r_i} = \frac{r_s - z_{int}}{\sqrt{r_s^2 - x_{int}^2}} \quad (\text{A.7})$$

If one recalls Archimedes' rule that the surface area of a slice of a sphere and of a cylinder (whose radii are the same) are the same; instead of calculating the surface area on the sphere, one can calculate the surface area on the cylinder. The surface area on the cylinder can be calculated by adding up (i.e., integrating) the lengths of the arcs on the cylinder. The length of an arc is the radius times the angle it subtends. Since the angle calculated above (for the sphere) is also the same for the cylinder, it follows then that the length of the arc on the cylinder is:

$$L_{arc} = r_s \cdot 2\alpha = r_s \cdot 2 \cdot \arccos\left(\frac{r_s - z_{int}}{\sqrt{r_s^2 - x_{int}^2}}\right) \quad (\text{A.8})$$

Then the integral required to find the surface area is straight forwardly:

$$A_{OS} = \int_0^{x_{max}} L_{arc} dx \quad (\text{A.9})$$

A special case would appear if the distance between the base of the cone and the sphere center (i.e., h) is less than twice the radius of the cone (i.e. r_c). In that case, a cap of the sphere comes additionally to the above calculated area as being part of the sought area (see fig.A.1b). The area of a cap of a sphere can easily be calculated if the height is known. In this case, the height of the cap is:

$$h_{cap} = r_s - x_{max} \quad (\text{A.10})$$

and then the area of the cap:

$$A_{cap} = 2\pi r_s h_{cap} = 2\pi r_s (r_s - x_{max}) \quad (\text{A.11})$$

Thus the total area enclosed on the surface of the sphere can be generalized

as:

$$\begin{aligned} \text{for } h < 2r_c, \quad A_{total} &= A_{OS} + A_{cap} \\ \text{for } h \geq 2r_c, \quad A_{total} &= A_{OS} \end{aligned} \quad (\text{A.12})$$

finally

$$\check{F} = \frac{A_{total}}{4\pi r_s^2} \quad (\text{A.13})$$

A.2 Calculation procedure for \check{G}

The molecules enter the pore from the left pore entrance and reach the cross-section at a distance h (see fig.A.2a). The vertical line at this distance is the base of the cylinder.

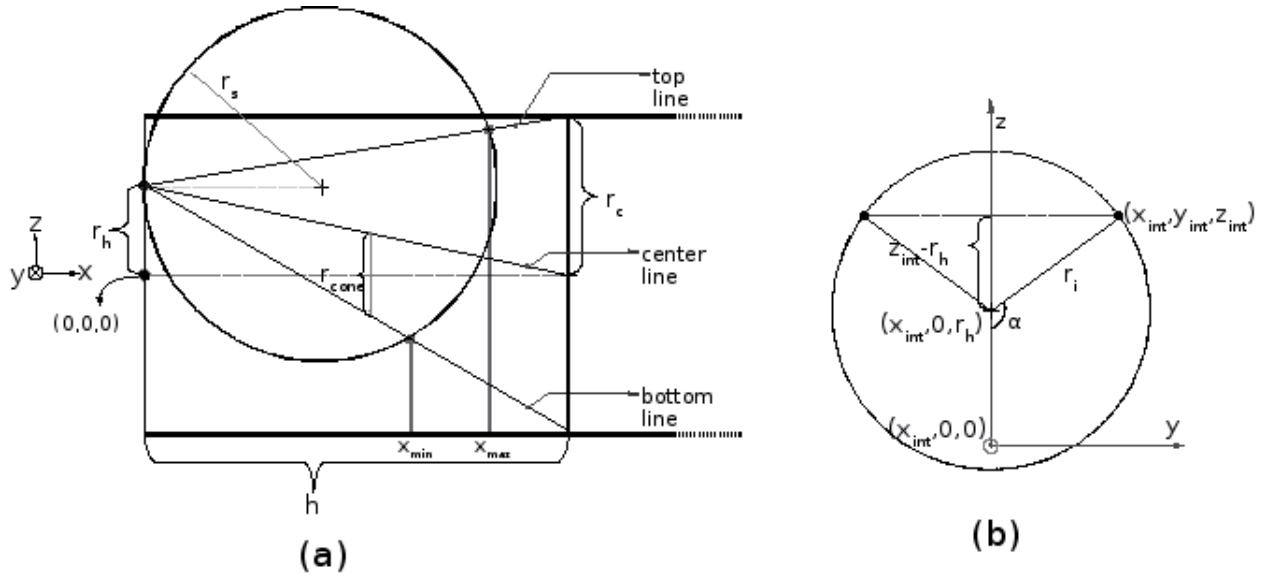


Figure A.2: Auxiliary figures for the calculation of the projection area in \check{G} calculation. (a) The sphere tangent to the entrance at position r_h and its relation to the cone whose base is at a distance h from the entrance, (b) a sample arc built between x_{min} and x_{max} .

The equations describing the sphere and the cone are, respectively:

$$(x - r_s)^2 + y^2 + (z - r_h)^2 = r_s^2 \quad (\text{A.14})$$

$$y^2 + \left(z - \left(\frac{-r_h}{h}x + r_h \right) \right)^2 = \left(\frac{r_c}{h}x \right)^2 \quad (\text{A.15})$$

For the determination of the cone equation, the center line equation

$$z_{centerline} = \frac{-r_h}{h}x + r_h \quad (\text{A.16})$$

and the radius of the cross-section of the cone at an arbitrary x (found by using similar triangles)

$$r_{cone} = \frac{r_c}{h}x \quad (\text{A.17})$$

is used. The intersection curve between the sphere and the cone (found by equating eq.A.14 and A.15) is:

$$z_{int} = \frac{h}{2r_h}x_{int} \left(\left(\frac{r_c}{h} \right)^2 - \left(\frac{r_h}{h} \right)^2 + 1 \right) + r_h \quad (\text{A.18})$$

It should be noted that eq.A.18 is only valid for $x_{int} \neq 0$ and $x_{min} \leq x_{int} \leq x_{max}$. In order to find x_{min} and x_{max} , one needs the equations for the top-line and for the bottom-line, which are:

$$z_{top} = \frac{r_c - r_h}{h}x + r_h \quad (\text{A.19})$$

$$z_{bottom} = \frac{-r_c - r_h}{h}x + r_h \quad (\text{A.20})$$

Inserting these two equations into the sphere equation, one finds the intersection points of the sphere and the two lines. The x-coordinates of the intersection points are zero and:

$$x_{max} = \frac{2r_s}{1 + \left(\frac{r_c - r_h}{h} \right)^2} \quad (\text{A.21})$$

$$x_{min} = \frac{2r_s}{1 + \left(-\frac{r_c + r_h}{h} \right)^2} \quad (\text{A.22})$$

From fig.A.2b, it can be seen that the cosine of the angle α is:

$$\cos\alpha = \frac{-(z_{int} - r_h)}{r_i} \quad (\text{A.23})$$

Note: The minus sign in the above equation is due to its position with respect to the origin used to define the angle. The origin for the angle is $(x_{int}, 0, r_h)$ and the negative z direction is defined to be the positive direction for the corresponding axis. Since in this case the angle turned out to be greater than $\pi/2$, the cosine of this angle is supposed to be a negative value. Therefore, the length $(z_{int} - r_h)$ has to be multiplied with minus one. The length of the arc that would be built on a surface of a similar cylinder would then be (see Appendix - Calculation procedure for \check{F}):

$$L_{arc} = 2r_s \cdot arccos\left(\frac{r_h - z_{int}}{r_i}\right) \quad (\text{A.24})$$

The radius of the arc can be found by utilizing the equation of the sphere (eq.A.14):

$$r_i = \sqrt{r_s^2 - (x - r_s)^2} \quad (\text{A.25})$$

Consequently, the area of the piece of the sphere bounded by the intersection curve between x_{min} and x_{max} is then:

$$A_{OS} = \int_{x_{min}}^{x_{max}} L_{arc} dx \quad (\text{A.26})$$

and if exists, the area of the cap left behind to the right of the x_{max} is:

$$A_{cap} = 2\pi r_s \cdot (2r_s - x_{max}) \quad (\text{A.27})$$

Thus the total area enclosed on the surface of the sphere for this case also is:

$$A_{total} = A_{OS} + A_{cap} \quad (\text{A.28})$$

The fraction of this area to the total sphere area can then be easily calculated:

$$\check{G}_h = \frac{A_{total}}{4\pi r_s^2} \quad (\text{A.29})$$

\check{G}_h is the fraction only at the circle with radius r_h at the entrance. The

overall fraction can then be calculated by the following formula:

$$\check{G} = \frac{\int_0^{r_c} 2\pi r_h \cdot \check{G}_h \cdot dr_h}{\pi r_c^2} \quad (\text{A.30})$$

A.3 Pores with closed-end and symmetric pressures modeled with projection approach

A.3.1 Pores with closed-end

Pores with closed-end, i.e., dead-end pores or sacks, can also be easily modelled with projection approach. Assuming that the pore is taken to be cylindrical, the end of the pore will be circular. For a normal pore cross-section the total amount of molecules passing through it is important. For the end of the pore, beside that, the radial (wrt. center of the closed-end) distribution of these molecules would be important. This radial distribution can be found by taking the difference between flows through subsequent discs to be built on the closed-end surface.

If one defines the origin to be at the entrance of the pore, a pore having a length of L_{pore} , a radius of r_{pore} , and n slices: one can take slice i which is at a distance of k , $k < L_{pore}$, from the closed-end. The center of the end of the pore would then correspond to $\{0, L_{pore}, r_{pore}\}$. Due to the symmetry, for any surface element on the i^{th} slice, the fraction of flow through any disc (its center being at $\{0, L_{pore}, r_{pore}\}$) at the closed-end would be identical. Thus calculation of this (fraction) value can be done for a single surface element of slice i .

The calculation procedure for this fraction, say \check{H} , would then be similar to the \check{F} calculation with a slight change in formulation. In this case, beside the radius of hypothetical sphere and the pore radius, the radius of the disc should be inserted into the formulation. The pore radius in this case would determine the center of the disc, and its size would be determined by its own radius. But the general procedure, the calculation of the sphere, cone and

the projection area will all be very similar to the \check{F} case.

If one takes small enough radius steps for these discs, one can then get a good distribution of flow on the closed-end. The difference between these fractions (\check{H}) would again give the fraction corresponding the ring, i.e. $\check{h}_j = \check{H}_j - \check{H}_{j-1} = \Delta\check{H}$. One can assume that $\check{H}_0 = 0$ which corresponds to the center-point (having no area) of the closed-end. In this way, the radial distribution of the impingement rate on the closed-end can be determined.

The scattering rate calculation for the dead-end will be then similar to the calculation of \check{G} (for an open-end) with a slight change. This time every ring has to be assigned the corresponding scattering value instead of the homogeneous distribution, and the integration should be made accordingly.

A.3.2 Pores with symmetric pressures

Pores with symmetric pressures at the two ends would correspond to the small pores in the parallel pore model for bi-disperse systems. In such a case, only the half of the pore should be calculated, since the other half, due to symmetry, would be a mirror image of this half. That means, e.g., the surface concentration, the impingement rate, etc. corresponding to the i^{th} slice would be identical with the $(n - i + 1)^{th}$ slice, assuming one has divided the pore into even number of slices. In such a case, the solution of the equations for the whole pore length will require unnecessary computational work. Instead, one can modify the \check{f} and \check{g} matrices, and the unknowns accordingly and shrink them into half in each dimension (for $\check{f}_{n \times n}$ that means one quarter of size, i.e., $\check{f}_{\frac{n}{2} \times \frac{n}{2}}$).

For example if one considers eq.3.36 for this symmetric pressures case, one should notice first that $N_{z=0}^{lr} = N_{z=L}^{rl}$ and thus one can write

$$(N_{imp})_{\frac{n}{2} \times 1} = \dots + N_{z=0}^{lr} \cdot \left((\check{g})_{\frac{n}{2} \times 1} + (\check{g}_{flipped})_{\frac{n}{2} \times 1} \right) \quad (\text{A.31})$$

for the part missing in the equation (the place indicated by \dots), one needs to divide the $\check{f}_{n \times n}$ into four equal parts, named *Upper-Left*, *Upper-Right*, *Lower-Left* and *Lower-Right* parts.

$$\check{f}_{n \times n} \equiv \begin{bmatrix} \check{f}_{UL} & \check{f}_{UR} \\ \check{f}_{LL} & \check{f}_{LR} \end{bmatrix} \quad (\text{A.32})$$

then one needs to left-right flipp the \check{f}_{UR} :

$$(\check{f}_{UR})_{lr-flipped}(i, j) = (\check{f}_{UR})(i, \frac{n}{2} - j + 1) \quad (\text{A.33})$$

note that \check{f}_{UR} is an $\frac{n}{2} \times \frac{n}{2}$ matrix.

As a result, the impingement rate only for the half of the pore (but including the effect of the other symmetric half) can be calculated using only the half of the pore unknowns as:

$$\begin{aligned} (N_{imp})_{\frac{n}{2} \times 1} = & \left((\check{f}_{UL})_{\frac{n}{2} \times \frac{n}{2}} + ((\check{f}_{UR})_{lr-flipped})_{\frac{n}{2} \times \frac{n}{2}} \right) \cdot (N_{scat})_{\frac{n}{2} \times 1} \\ & + N_{z=0}^{lr} \cdot \left((\check{g})_{\frac{n}{2} \times 1} + (\check{g}_{flipped})_{\frac{n}{2} \times 1} \right) \end{aligned} \quad (\text{A.34})$$

In words, the \check{f}_{UL} gives the fractions corresponding to the first-half of the pore, the $(\check{f}_{UR})_{lr-flipped}$ accounts for the other-half of the pore, which is due to symmetry the mirror image of this half. Because of this mirror image relation, the matrix has to be flipped, and so the interaction between, the first-half and the second-half slices are accounted for just taking the first-half of the slices into consideration.

The rest of the necessary equations for the solution of the system at hand (as the case may be: sole Knudsen, Knudsen plus surface flow or Knudsen plus surface flow with reaction) should also be modified in this logic accordingly.

A.4 Experimental Procedure

A.4.1 Single-pellet reactor

Catalyst activation

The used pellets lose their activity when kept in open atmosphere. This can happen due to the adsorption of water vapour or any other gases (e.g., O_2) on to the catalytic surface. In order to activate the catalyst and make sure that the catalyst surface was free of any contaminant particles, they are heated in a H_2 atmosphere in the reactor at a pressure of 5-bar and a temperature of 100°C for 2 hours (according to the manufacturer specifications). The oven was turned on and adjusted to 100°C . Then a vacuum was created in the reactor by opening valves V22, V16, V9, V6, V10 and closing V17 while turning on the vacuum pump. Once vacuum was created valves V22, V16 were closed and V3 opened to allow hydrogen flow into the reactor. The pressure was allowed to build up until it was 5 bars and then V3 was closed and the reactor was allowed to stand at this temperature and pressure for 2 hours so as to activate the catalyst.

Starting the reaction

Once activation was complete valves V16, V22 and V17 were opened in this order and the gas was vented out until the pressure indicator shows 1.1 bars. Now valve V17 was closed and V10 opened and the vacuum pump was turned on to create a vacuum in the reactor. Valves V22, V16 and V10 were closed and the vacuum pump was switched off. The reactor is first filled with pure N_2 . Then the appropriate values for the reactant were set on, and valves V1, V2 and V3 opened and the flow controller was turned on. When the pressure reached the set pressure of 1.1 bars valve 6 was closed. The reaction was allowed to run with samples taken periodically until the reaction got to steady state.

Sample taking

The sample taking was done via 6-way valve (to which the sample loop is connected) and analysed with gas chromatography. There were four types of samples: the calibration gas, exit (reactor chamber), center chamber and inlet. The samples were periodically taken so as to check the steady state condition of the reaction as well as to know the extent of reaction that took place inside the reactor.

Calibration gas

Valve V10 was closed, V8 and V17 was opened for a few seconds between 5-10 seconds for the GC column to be filled with the sample. Once the GC sample loop column was filled, V8 was closed and after 10-15 seconds the 6 port valve V11 was opened and simultaneously the *RUN* button on the GC was pressed for the sample analysis after which V17 was closed and V10 was opened to create a vacuum in the loop for the next sample.

Exit gas

Valve V21 was opened for 5 seconds (for the GC sample loop column to be filled) and closed, V17 was opened to ensure that the pressure of the sample equilibrated to atmospheric pressure. Then V11 was opened and simultaneously the *RUN* button on the GC was pressed for the sample analysis after which V17 was closed and V10 was opened to create a vacuum in the loop for the next sample.

Center gas

Valve V22 was opened for 5 seconds (for the GC sample loop column to be filled) and closed and V17 was opened to ensure that the pressure of the sample equilibrated to atmospheric pressure. Then V11 was opened and simultaneously the *RUN* button on the GC was pressed for the sample analysis after which V17 was closed and V10 was opened to create a vacuum in the loop for the next sample.

Inlet gas

Valve V16 was opened for 5 seconds (for the GC sample loop column to be filled) and closed and V17 was opened to ensure that the pressure of the sample equilibrated to atmospheric pressure. Then V11 was opened and simultaneously the *RUN* button on the GC is pressed for the sample analysis after which V17 was closed and V10 was opened to create a vacuum in the loop for the next sample.

Ending the reaction

Closing the valves V2, V3, V1 which were used for allowing the ethylene, hydrogen and nitrogen respectively stops the reaction. V6 was opened and then V17 to vent out the reacting gases. Once the reactor reached atmospheric pressure then V17 was closed and V10 was opened and consequently the vacuum pump was switched on and all gases were pumped out from the reactor. Finally the reactor was kept under nitrogen pressure till the next experiment started or reactivation.

A.4.2 Turbo-reactor

Catalyst activation

In order to activate the catalyst it is kept in a H_2 atmosphere in the reactor at a pressure of 5 bars and a temperature of 100°C for 2 hours. The oven was turned on and adjusted to 100°C. Then a vacuum was created in the reactor by opening valves V13, V18, V15, V10 and closing V17 and the vacuum pump was turned on. Once vacuum was created valves V15 was closed and V13 opened to let hydrogen flow into the turbo-reactor. The pressure was allowed to build up until it was 5 bars and then V13 was closed and the reactor was allowed to stand at this temperature and pressure for 2 hours so as to activate the catalyst.

Starting the reaction

Once activation was complete valves V15 and V17 were opened in this order and the gas was vented out until the pressure indicator showed atmospheric pressure. Now valve V17 was closed and V10 was opened and vacuum pump turned on to create a vacuum in the reactor. Valves V15 and V10 were closed and the vacuum pump was switched off. The appropriate values for the reactant and the diluent were set on the flow controllers and valves V23, V24 and V25 were opened and the flow controller was turned on and the pressure controller was set to required value. The reaction was allowed to run with samples taken periodically until the reaction got to steady state.

Sample taking

As in the single-pellet reactor the sample taking was done and analysed with gas chromatography. There were three types of samples taken at the end of every reaction: calibration gas, exit and inlet. The samples were periodically taken so as to check the steady state condition of the reaction as well as to know the extent of reaction taking place inside the reactor.

Check gas

Valve V10 was closed; V8 and V17 were opened for a few seconds between 5-10 seconds for the GC column to be filled with the sample. Once the GC sample loop column was filled, V8 was closed and after 10-15 seconds the 6 port valve V11 was opened and simultaneously the *RUN* button on the GC was pressed for the sample analysis after which V17 was closed and V10 was opened to create a vacuum in the loop for the next sample.

Exit gas

Valve V14 was opened for 5 seconds (for the GC sample loop column to be filled) and closed, V17 was opened to ensure that the pressure of the sample equilibrated to atmospheric pressure. Then V11 was opened and simultaneously the *RUN* button on the GC was pressed for the sample analysis after

which V17 was closed and V10 was opened to create a vacuum in the loop for the next sample

Inlet gas

Valve V15 was opened for 5 seconds (for the GC sample loop column to be filled) and closed and V17 was opened to ensure that the pressure of the sample equilibrated to atmospheric pressure. Then V11 was opened and simultaneously the *RUN* button on the GC was pressed for the sample analysis after which V17 was closed and V10 was opened to create a vacuum in the loop for the next sample

A.4.3 Gas chromatography sample analysis

The different samples from the reactors were analysed with Perkin-Elmer gas chromatograph (GC), model 1022 GC combined with a 2m, 1mm 1D Hayesep Q Micro packed column and thermal conductivity detector (TCD). The carrier gas *He* (purity 5.0), supplied by Messer Griesheim GmbH, was filtered by two Messer Griesheim Oxisorb-W filter cartridges for the removal of oxygen and hydrocarbon traces. Helium gas inlet pressure is set to 6.2 bars so that the gas flow is continuous on the GC column. The calibration gas from Messer with a known composition is used for the calibration of the GC. The calibration gas consists of 79.4% N_2 , 10.3% C_2H_4 , and 10.3% C_2H_6 , from Air Liquid GmbH.

The GC employs a method named *ethy2* with detector and oven temperature 120°C and 60°C respectively. The carrier gas *He* flow rate is set to 14 ml/min in the chromatograph. At the end of every sample analysis the sample loop of the GC is purged to remove any old sample from the GC column. The analysis time for the samples was 2.5 min.

A.5 List of Suppliers

Table A.1: List of suppliers for the gases and equipment used.

Equipment/Gas	Model/Purity	Supplier
Nitrogen	5.0 (99.999 vol.%)	Westfalen AG
Hydrogen	5.0 (99.999 vol.%)	Westfalen AG
Ethylene	3.5 (99.95 vol.%)	Westfalen AG
Calibration gas	Ethylene(3.0) 10.3 vol.%, Ethane(2.5) 10.3 vol.%, Nitrogen(5.0) 79.4 vol.%	Messer Griesheim
Helium	5.0 (99.999 vol.%)	Air Liquid GmbH
for SPR		
Ethylene MFC	Type 1259C	MKS Instruments Inc.
Nitrogen MFC	Type 1259C	MKS Instruments Inc.
Hydrogen MFC	Type 1259C	MKS Instruments Inc.
Pressure controller	Type P-702C-FA-33P	Bronkhorst high tech.
for TR		
Ethylene MFC	Type 1179B	MKS Inst. GmbH
Nitrogen MFC	Model No: 5850S	Brooks Inst. B.V.
Hydrogen MFC	Type 1179B	MKS Inst. GmbH
Pressure controller	Model No: 5866	Brooks Inst. B.V.

MFC: mass flow controller

A.6 Mercury-Porosimetry plots for relevant catalyst pellets

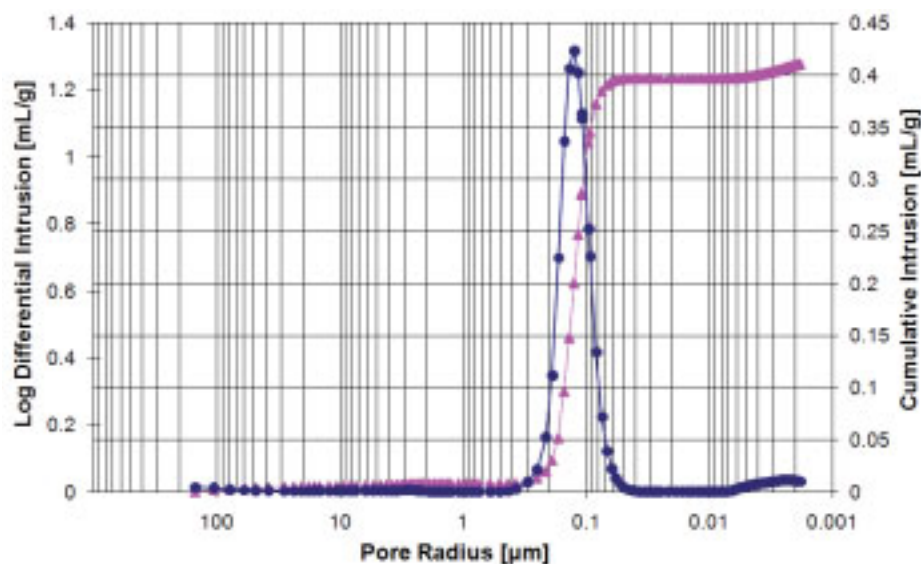


Figure A.3: Pore size distribution plot of Y41573, based on mercury-porosimetry analysis.

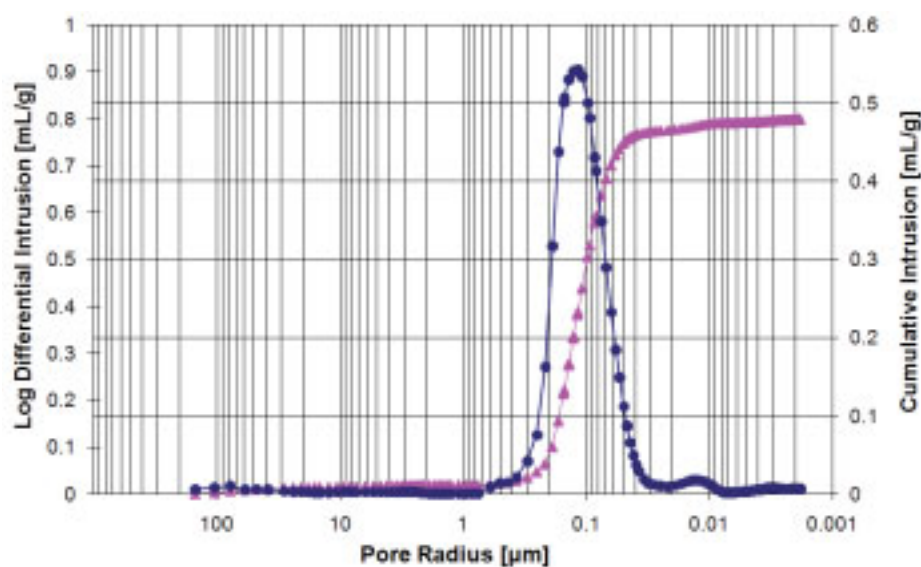


Figure A.4: Pore size distribution plot of Y41574, based on mercury-porosimetry analysis.

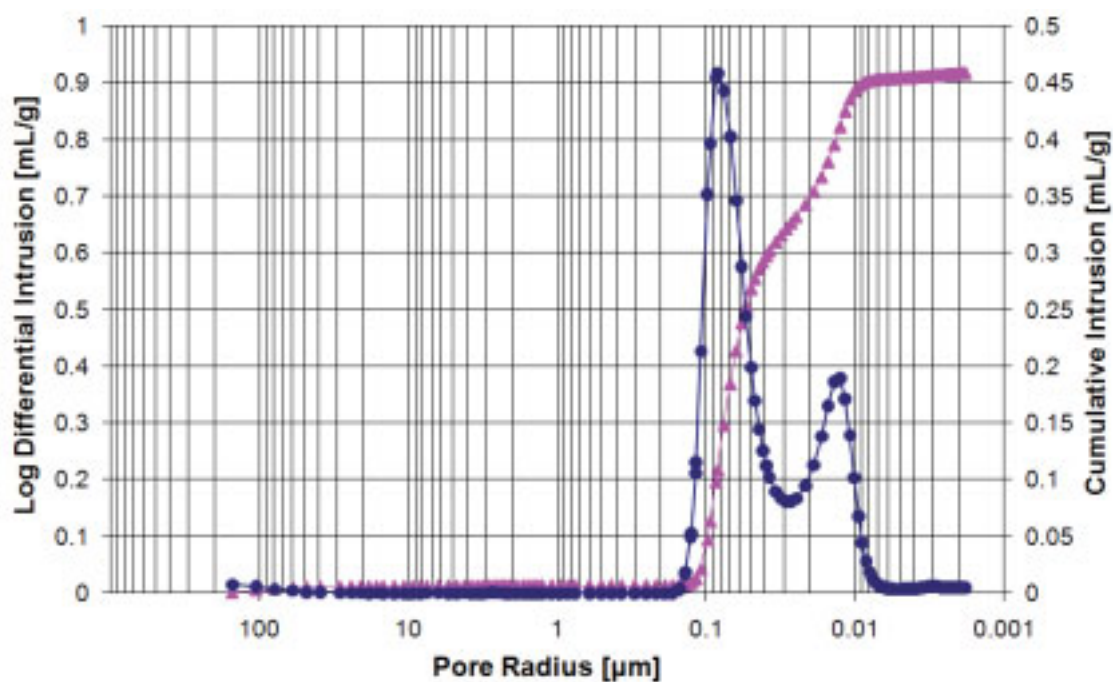


Figure A.5: Pore size distribution plot of Y41575, based on mercury-porosimetry analysis.

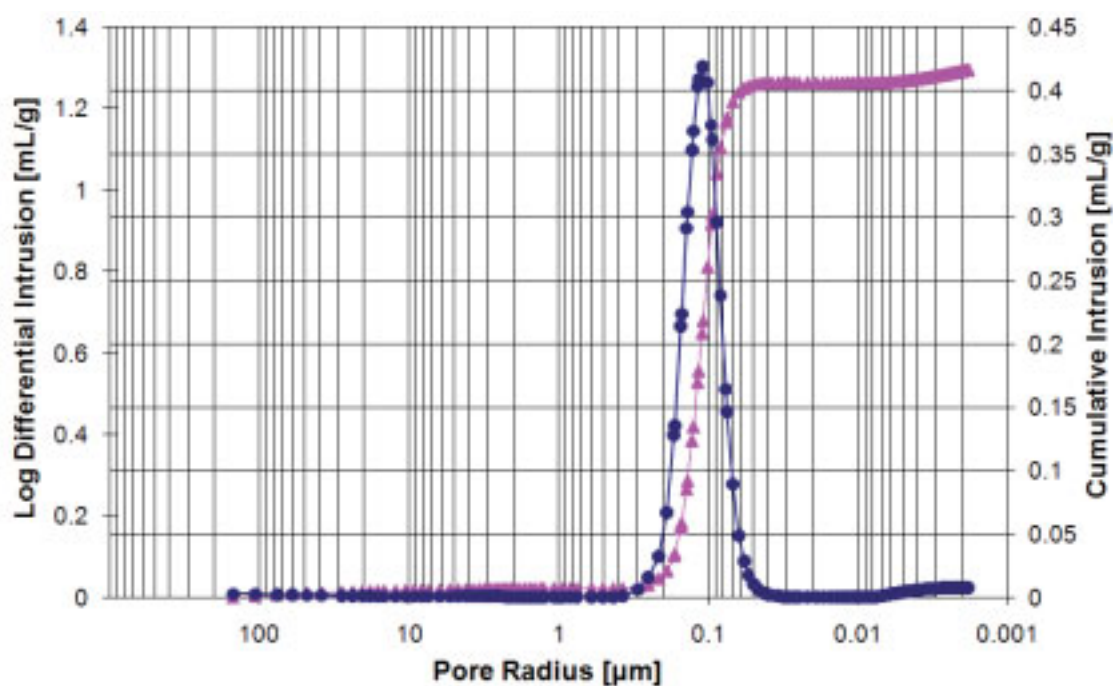


Figure A.6: Pore size distribution plot of Y42099, based on mercury-porosimetry analysis.

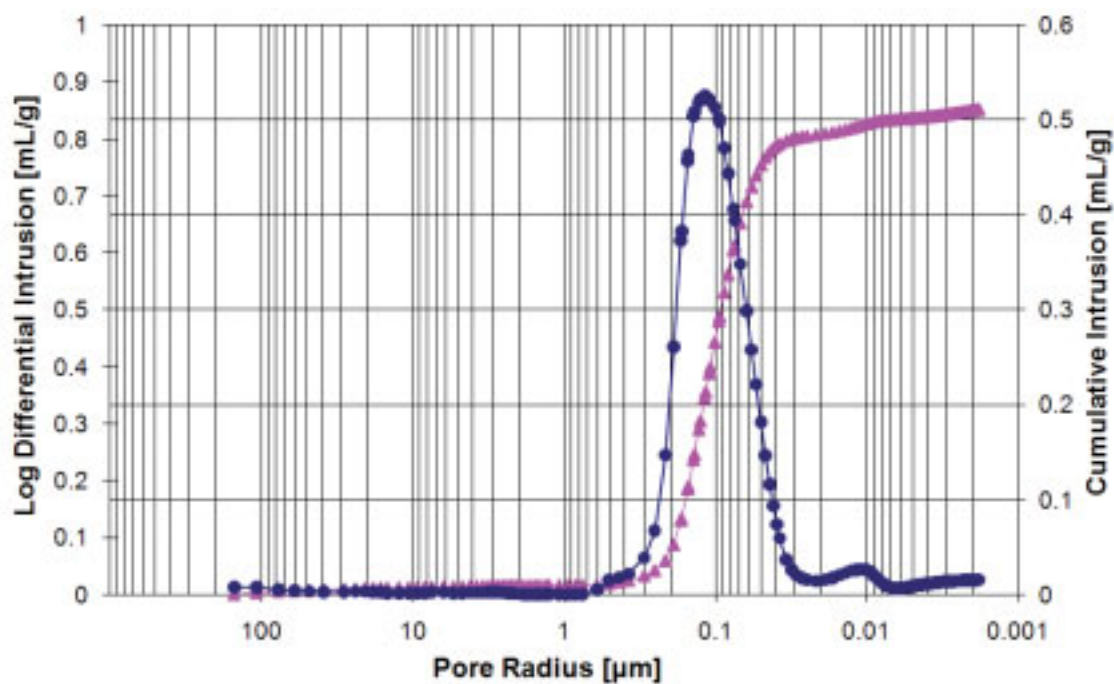


Figure A.7: Pore size distribution plot of Y42100, based on mercury-porosimetry analysis.

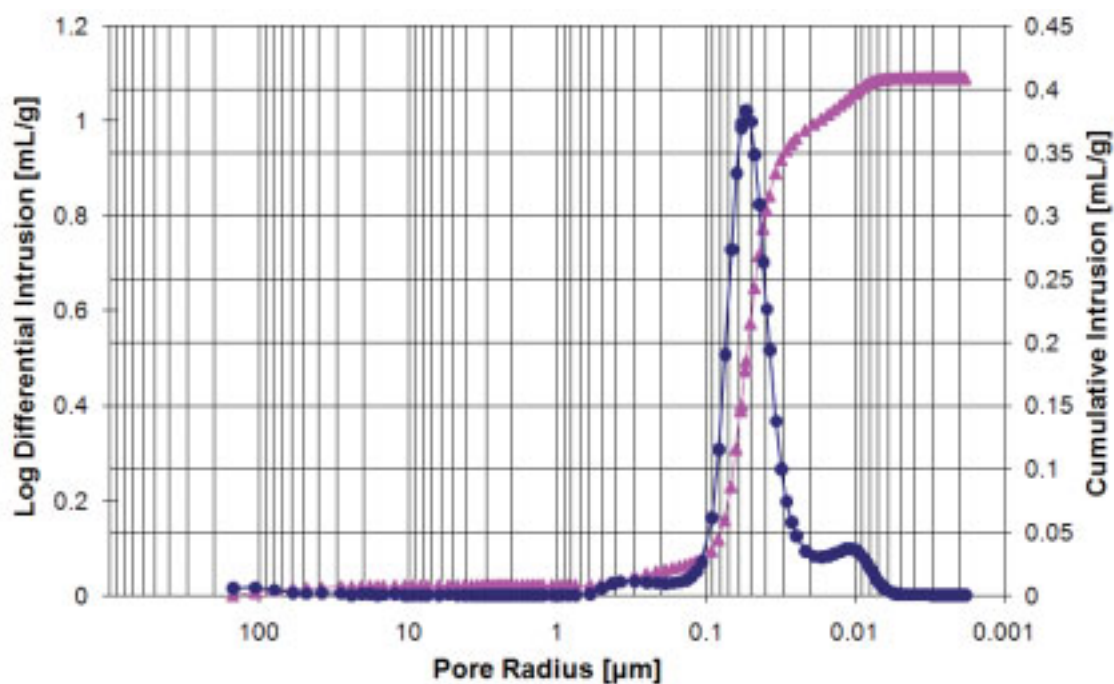


Figure A.8: Pore size distribution plot of Y42218, based on mercury-porosimetry analysis.

A.7 Kinetic experiments data

Because of their large sizes, the tables are given in the following pages.

Table A.2: Data from kinetic experiments, *TR1*. A pressure of 3 [bar], total inlet flow rate of 2000 [mL/min], 0.0213 [g] of catalyst Y41573 (0.3 wt% loading) from the fraction $0.5 < \bar{x} < 0.8$ mm was used in the experiments, and the original turbo-reactor with a rotation speed of 1500 rpm was utilized.

T [°C]	Inlet [mol %]			Exit Composition [mol %]				$R_{\text{rxn}}^{\text{E}^*}$	$R_{\text{rxn}}^{\text{A}^\circ}$
	N_2	C_2H_4	H_2	N_2	C_2H_4	C_2H_6	H_2	[mol/s/g _{cat}]	[mol/s/g _{cat}]
30°C	0.203	0.154	0.643	0.153	0.113	0.674	0.06	3.771E-03	3.616E-03
	0.16	0.199	0.64	0.119	0.163	0.67	0.048	2.973E-03	2.926E-03
	0.2	0.198	0.603	0.151	0.153	0.636	0.061	3.687E-03	3.672E-03
	0.1	0.198	0.701	0.074	0.181	0.717	0.028	1.793E-03	1.740E-03
	0.2	0.099	0.701	0.164	0.062	0.73	0.043	2.751E-03	2.633E-03
	0.199	0.162	0.64	0.164	0.124	0.667	0.045	2.699E-03	2.777E-03
	0.162	0.192	0.646	0.124	0.168	0.665	0.044	2.797E-03	2.717E-03
	0.199	0.198	0.603	0.158	0.158	0.633	0.051	3.140E-03	3.129E-03
	0.101	0.199	0.7	0.076	0.18	0.717	0.028	1.745E-03	1.756E-03
	0.201	0.098	0.701	0.168	0.068	0.723	0.04	2.557E-03	2.480E-03
	0.2	0.161	0.64	0.154	0.121	0.669	0.055	3.489E-03	3.346E-03
	0.16	0.2	0.64	0.119	0.166	0.668	0.048	2.987E-03	2.939E-03
	0.201	0.198	0.601	0.152	0.157	0.631	0.06	3.708E-03	3.633E-03
	0.101	0.197	0.702	0.074	0.177	0.719	0.03	1.871E-03	1.869E-03
0.201	0.097	0.702	0.162	0.058	0.732	0.048	2.987E-03	2.939E-03	
60°C	0.205	0.147	0.648	0.163	0.12	0.667	0.05	3.205E-03	3.042E-03
	0.161	0.199	0.64	0.125	0.169	0.664	0.042	2.628E-03	2.575E-03
	0.199	0.199	0.602	0.159	0.16	0.63	0.051	3.038E-03	3.100E-03
	0.1	0.204	0.696	0.076	0.183	0.714	0.027	1.659E-03	1.679E-03
	0.2	0.1	0.701	0.171	0.066	0.726	0.036	2.234E-03	2.220E-03
	0.2	0.16	0.64	0.165	0.125	0.666	0.044	2.703E-03	2.717E-03
	0.158	0.205	0.637	0.128	0.178	0.658	0.036	2.218E-03	2.241E-03
	0.199	0.198	0.603	0.16	0.161	0.63	0.048	2.994E-03	2.953E-03
	0.101	0.199	0.7	0.078	0.185	0.712	0.025	1.608E-03	1.573E-03
	0.207	0.095	0.698	0.175	0.069	0.72	0.035	2.501E-03	2.180E-03
	0.201	0.177	0.622	0.157	0.125	0.664	0.053	3.350E-03	3.230E-03
	0.159	0.199	0.642	0.119	0.166	0.668	0.047	2.914E-03	2.881E-03
	0.198	0.206	0.596	0.15	0.172	0.621	0.056	3.624E-03	3.403E-03
	0.099	0.204	0.697	0.072	0.182	0.716	0.03	1.867E-03	1.869E-03
0.198	0.102	0.7	0.163	0.07	0.725	0.042	2.684E-03	2.587E-03	
100°C	0.2	0.178	0.622	0.163	0.127	0.663	0.047	2.824E-03	2.867E-03
	0.161	0.195	0.643	0.132	0.173	0.661	0.035	2.134E-03	2.160E-03
	0.201	0.188	0.61	0.16	0.162	0.629	0.049	3.118E-03	2.984E-03
	0.1	0.201	0.699	0.076	0.181	0.717	0.026	1.659E-03	1.619E-03
	0.207	0.095	0.698	0.18	0.073	0.714	0.033	2.103E-03	2.041E-03
	0.201	0.157	0.642	0.169	0.128	0.663	0.039	2.483E-03	2.420E-03
	0.161	0.199	0.64	0.132	0.173	0.661	0.035	2.154E-03	2.180E-03
	0.202	0.177	0.621	0.168	0.141	0.647	0.044	2.635E-03	2.717E-03
	0.101	0.203	0.697	0.08	0.184	0.713	0.023	1.472E-03	1.450E-03
	0.2	0.104	0.696	0.174	0.078	0.716	0.032	2.030E-03	1.999E-03
	0.201	0.155	0.644	0.16	0.122	0.669	0.049	3.132E-03	2.998E-03
	0.16	0.195	0.645	0.122	0.168	0.667	0.043	2.777E-03	2.646E-03
	0.2	0.198	0.602	0.156	0.158	0.632	0.053	3.346E-03	3.230E-03
	0.101	0.2	0.7	0.074	0.178	0.719	0.028	1.871E-03	1.748E-03
0.2	0.101	0.699	0.167	0.072	0.722	0.039	2.542E-03	2.409E-03	

* the reaction rate is based on the consumption rate of ethylene.

° the reaction rate is based on the production rate of ethane.

Table A.3: Data from kinetic experiments, *TR2*. A pressure of 1.1 [bar], total inlet flow rate of 200 [mL/min], 0.9336 [g] of catalyst Y42099 (0.001 wt% loading) from the fraction $0.5 < \bar{x} < 0.8$ mm was used in the experiments and the new turbo-reactor with a rotation speed of 3000 rpm was utilized.

T [°C]	Inlet [mol %]			Exit Composition [mol %]				R_{rxn}^* [mol/s/g _{cat}]
	N_2	C_2H_4	H_2	N_2	C_2H_4	C_2H_6	H_2	
30°C	39.15	41.22	19.63	39.29	40.81	0.00	19.89	1.005E-06
	39.14	20.76	40.10	39.16	20.45	0.00	40.40	5.881E-07
	49.23	42.25	8.52	49.02	41.14	0.00	9.83	2.789E-06
	50.08	10.87	39.05	49.16	10.52	0.00	40.32	5.903E-07
	58.13	20.75	21.12	57.02	20.07	0.00	22.91	1.257E-06
	58.40	30.95	10.65	58.45	30.57	0.00	10.98	8.033E-07
	58.54	10.69	30.77	58.47	10.51	0.00	31.02	3.028E-07
	78.36	10.55	11.09	78.39	10.44	0.00	11.17	1.778E-07
	72.25	21.36	6.39	69.63	20.36	0.00	10.00	1.847E-06
	68.94	10.41	20.65	68.88	10.25	0.00	20.87	2.681E-07
80.49	10.83	8.67	79.51	10.52	0.00	9.96	4.981E-07	
50°C	38.79	43.34	17.87	38.97	42.80	0.00	18.23	1.393E-06
	39.38	20.65	39.96	38.91	20.16	0.00	40.92	9.100E-07
	49.59	41.83	8.58	49.24	41.09	0.00	9.67	1.878E-06
	49.61	10.38	40.01	49.73	10.15	0.00	40.12	3.858E-07
	58.86	20.59	20.55	58.96	20.42	0.00	20.62	3.208E-07
	59.07	30.72	10.21	59.20	30.48	0.00	10.33	5.282E-07
	57.93	10.84	31.23	57.63	10.62	0.00	31.75	3.684E-07
	77.85	10.59	11.56	77.85	10.43	0.00	11.72	2.782E-07
	68.14	21.21	10.66	67.52	20.68	0.00	11.80	9.841E-07
	68.51	10.71	20.79	68.15	10.51	0.00	21.34	3.365E-07
100°C	39.57	42.13	18.30	39.50	41.47	0.14	18.90	1.687E-06
	40.06	20.85	39.09	39.85	20.66	0.15	39.34	3.551E-07
	49.85	41.53	8.62	49.47	40.66	0.00	9.87	2.163E-06
	49.13	10.72	40.14	49.20	10.56	0.10	40.13	2.706E-07
	58.55	20.87	20.58	58.61	20.50	0.00	20.89	6.876E-07
	59.14	30.95	9.91	59.36	30.76	0.00	9.87	4.030E-07
	58.66	10.59	30.74	58.72	10.45	0.00	30.83	2.460E-07
	78.05	10.66	11.29	78.07	10.54	0.00	11.38	1.873E-07
	68.60	21.02	10.38	68.55	20.81	0.00	10.64	3.940E-07
	68.81	10.48	20.71	68.89	10.35	0.00	20.77	2.256E-07

* the reaction rate is based on the consumption rate of ethylene.

Nomenclature, Index and Bibliography

Nomenclature

A	:	in subscript denotes a property of species A
A	:	denotes a small surface element
$A_{solid/pore}^{face}$:	outer surface area available per pore, [$m^2/pore$]
$ADRD$:	abbr. for Adsorption Desorption Rate Difference
c, c_i	:	concentration
C_A	:	concentration of A in gas phase, [mol/m^3]
C^d	:	conductance
D_{ij}	:	(ordinary) binary diffusion coefficient, [m^2/s]
D_i^{Kn}	:	Knudsen diffusion coefficient, [m^2/s]
D_{pellet}	:	diameter of pellet, [mm]
D_A^{Surf}	:	surface diffusion coefficient, [m^2/s]
$D_{est.}^{Surf}$:	back-calculated surface diffusion coefficient using the adsorption-desorption equilibrium assumption, [m^2/s]
$\check{f}(h)$:	function giving the fraction of molecules scattered from pore surface and impinging onto a pore slice at a distance h
$\check{\check{F}}(h)$:	function giving the fraction of molecules scattered from pore surface and reaching pore cross-section at a distance h
$\check{\check{F}}_{flipped}$:	the flipped version of the vector $\check{\check{F}}$, i.e., $\check{\check{F}}_{flipped}(i) = \check{\check{F}}(n - i + 1)$
F^{gas}	:	gas phase flow rate, [mol/s]
F^{Surf}	:	surface flow rate, [mol/s]
F^{total}	:	total flow rate, i.e., $F^{gas} + F^{Surf}$, [mol/s]

$\check{g}(h)$:	function giving the fraction of molecules entering from the pore entrance and impinging onto a pore slice at a distance h
$\check{G}(h)$:	function giving the fraction of molecules entering from the pore entrance and reaching pore cross-section at a distance h
$\check{g}_{flipped}$:	the flipped version of the vector \check{g} , i.e., $\check{g}_{flipped}(i) = \check{g}(n - i + 1)$
G_{total}	:	total concentration of adsorption sites on the surface, $[mol/m^2]$
G_A	:	concentration of A on the surface, $[mol/m^2]$
$I_{n \times n}$:	identity matrix of size n
J	:	flux, $[mol/s/m^2]$
k_{ads}	:	adsorption rate constant, $[mol/s/m^2/Pa]$
$K_{ads}, K_{eq.}$:	adsorption equilibrium constant, $[1/Pa]$
k_{des}	:	desorption rate constant, $[mol/s/m^2]$
k'_{des}	:	desorption rate constant for a slice, $[mol/s/slice]$
k_{rxn}	:	reaction rate constant, $[mol/s/g_{cat}]$
los	:	abbr. for left outer surface, in subscript it denotes the value on the los
L_{pellet}	:	length of pellet, $[mm]$
L, L_{pore}	:	length of pore, $[m]$
M_w	:	molecular weight, $[kg/mol]$
n	:	total number of slices
$N_{z=0}^{lr}$:	rate of molecules entering from the left pore entrance, $[mol/s]$
$N_{z=L}^{rl}$:	rate of molecules entering from the right pore entrance, $[mol/s]$
N_{Av}	:	Avogadro's number
N_{dir}	:	rate of directly reflected molecules, $[mol/s]$
N_{imp}	:	impingement rate, $[mol/s]$
N_{right}^{out}	:	rate of molecules leaving from the right pore entrance, $[mol/s]$

N_{scat}	:	scattering rate, [mol/s]
P	:	pressure, [Pa]
P_{left}	:	pressure at the left entrance of the pore, [Pa]
P_{right}	:	pressure at the right entrance of the pore, [Pa]
q_{mono}	:	monolayer coverage, [mol/kg]
R	:	universal gas constant, [$J/mol/K$]
R_{ads}	:	rate of adsorption, [mol/s]
r_{ads}	:	rate of adsorption, [$mol/s/m^2$]
R_{des}	:	rate of desorption, [mol/s]
r_{des}	:	rate of desorption, [$mol/s/m^2$]
r, r_{pore}	:	radius of the pore, [m]
\bar{r}_{pore}	:	mean pore radius, [nm]
ros	:	abbr. for right outer surface, in subscript it denotes the value on the ros
R_{rxn}	:	reaction rate, [$mol/s/g_{cat}$]
S_{BET}	:	B.E.T. surface area, [m^2/g_{cat}]
s_{coef}	:	sticking coefficient
T	:	absolute temperature, [K]
\bar{V}_{pore}	:	average pore volume, [cm^3/g]
w	:	transmission probability
x	:	mole fraction
$\langle \bar{v} \rangle$:	mean average velocity, [m]
δz	:	sub-slice thickness, [m]
$\delta \bar{z}$:	relative sub-slice thickness, $\frac{\delta z}{r_{pore}}$
Δz	:	slice thickness, [m]
$\Delta \bar{z}$:	slice thickness with respect to pore radius, $\frac{\Delta z}{r_{pore}}$
β_{ads}	:	ratio of the surface area capable of adsorption (area of the adsorption sites) to the total surface area
ϵ	:	porosity
σ_A	:	collision cross-section for the molecules, [$m^2/molecule$]
σ_{LJ}	:	Lennard-Jones diameter of the molecule, [m]
θ	:	angle with the surface normal, [radians]
θ_i	:	surface coverage at slice i or for component i

Index

- adsorption-desorption rate difference,
 ADRD, 61, 62, 97, 120
- beaming effect, **65**, 68
- conductance, 62, **63**, 64, 66, 67
- cosine
 distribution, 65, 67, 68, **68**, 133
 law, 49, 68, 69, **69**, 70, 75, 85, 92,
 128
- Darken
 equation, 104, **104**, 110, 113, 114
 type, 109, 110, 112, 116, 128
- equilibrium assumption, 57–60, 97, 100,
 127, 128
- Horiuti-Polanyi mechanism, 17
- Knudsen
 diffusion, 5, **13**, 14, 15, 56, 62, 63,
 75, 85, 114, 117
 diffusion coefficient, 64, **64**, 68,
 93, 113
 flow, 49, 65, 68, 74, 76–78, 84, 92–
 94, 96, 101, 104, 106, 112
 formula, **80**
 number, 63, **63**
- Langmuir
 -Hinshelwood, 44, 115
 adsorption, **15**, 16, 57, 85–87, 91,
 92, 100, 102, 112
 model, **91**
- mercury-porosimetry, 11, **11**, 33, 52
- nitrogen-sorption, 11, **11**, 33, 52
- Oatley's formula, **66**
- outer-surface, 49, 59, **59**, 61, 84, **84**,
 85, 88, 90, 91, 97–99, 120, 121
- projection approach, 71, **71**, 74, 80,
 81, 83, 84, 89, 93, 121, 125,
 128, 132, 133
- single-pellet reactor, 19, **21**, 22, 26,
 31, 35, 38, 54, 55, 126, 127
- sticking coefficient, 86, 91
- sub-slices, 78, **78**, 80, 81, 94
- surface diffusion, 5, **13**, 16, **16**, 49,
 56, 57, 60, 62, 68, 84, 88, 103,
 104, 114, 120, 127, 128

- coefficient, 5, 49, 57, 62, 85, 92,
100, 102–104, 106–110, 113,
117, 118, 128
- flow, 104, 128
- flux, 56, 57
- model, **114**, 119
- monolayer, **85**
- transmission probability, 62, **63**, 65,
77, 80, 83
- turbo-reactor, 19, 20, 28, **28**, 31, 41,
43, 44, 46, 125
- van't Hoff equation, **47**

Bibliography

- [1] K. I. Zamaraev, Catalysis and New Technologies for Sustainable Development, *Chemistry for sustainable Development* **1993**, 1, 133–145.
- [2] R. J. Farrauto, *Fundamentals of Industrial Catalytic Processes*, Blackie Academic & Professional **1997**.
- [3] R. J. Wijngaarden, A. Kronberg, K. R. Westerterp, *Industrial Catalysis, Optimizing Catalysts and Processes*, WILEY-VCH, Weinheim **1998**.
- [4] P. Schneder, G. Emig, H. Hofmann, *Chem. Ing. Tech.* **1985**, 57, 728.
- [5] M. V. Twigg, *Catalyst Handbook*, Wolfe Publishing Ltd, second ed. **1989**.
- [6] J. Hagen, *Industrial Catalysis*, WILEY-VCH Verlag GmbH & Co, Weinheim, Germany, second ed. **2006**.
- [7] M. Morbidelli, A. Gavriilidis, A. Varma, *Catalyst Design: optimal distribution of catalyst in pellets, reactors, and membranes*, Cambridge university Press, New York **2001**.
- [8] I. Chorkendorff, J. W. Niemantsverdriet, *Concepts of Modern Catalysis and Kinetics*, WILEY-VCH, second ed. **2007**.
- [9] M. G. White, *Heterogeneous Catalysis*, Prentice-Hall, second ed. **1990**.
- [10] R. J. Farrauto, C. H. Bartholomew, *Fundamentals of Industrial Catalytic Processes*, Chapman & Hall **1997**.
- [11] A. B. Stiles, T. A. Koch, *Catalyst Manufacture*, Dekker, second ed. **1995**.
- [12] R. J. Masel, *Chemical Kinetics and Catalysis*, John Wiley and Sons Publications **2001**.
- [13] J. M. Thomas, W. J. Thomas, *Principles and Practice of Heterogeneous*

- Catalysis*, VCH **1997**.
- [14] A. Baiker, M. A. Kohler, Characterization of Catalysts, in *Catalysis, Kinetics, and Reactor Engineering*, N. P. Cheremisinoff, ed., *Handbook of Heat and Mass Transfer*, vol. 3, Gulf Publishing Company, Houston, Texas **1989**, pp. 3–62.
- [15] S. Lowell, *Characterization of porous solids and powders: surface area, pore size and density*, Springer, forth ed. **2006**.
- [16] D. D. Do, *Adsorption Analysis: Equilibria and Kinetics*, Imperial College Press **1998**.
- [17] J. Rouquerol, D. Avnir, C. W. Fairbridge, D. H. Everett, J. H. Haynes, N. Pernicone, J. D. F. Ramsay, K. S. W. Sing, K. K. Unger, Recommendations for the Characterization of Porous Solids, *Pure and Appl. Chem.* **1994**, 66, 1739–1758.
- [18] F. Rouquerol, K. Sing, *Adsorption by Powders and Porous Solids, Principles, Methodology and Applications*, Academic Press **1999**.
- [19] J. Haber, J. H. Block, B. Delmon, Manual of methods and procedures for catalyst characterization, *Pure and Appl. Chem.* **1995**, 67, 1257–1306.
- [20] G. P. Celata, Single-Phase Heat Transfer and Fluid Flow in Micropipes, *Heat Transfer Engineering* **2004**, 3, 25.
- [21] J. A. Wesselingh, R. Krishna, *Mass Transfer in Multicomponent Mixtures*, VSSD **2000**.
- [22] R. Krishna, J. Weselingh, The Maxwell-Stefan Approach to Mass transfer, *Chemical Engineering Science* **1997**, 52, 861–911.
- [23] E. L. Cussler, *Diffusion Mass Transfer in Fluid Systems*, Cambridge University Press, second ed. **1997**.
- [24] H. F. Rase, *Handbook of Commercial Catalysts, Heterogeneous Catalysis*, CrC Pr. Inc. **2000**.
- [25] S. Nishimura, *Handbook of Heterogeneous Catalytic Hydrogenation from Organic Synthesis*, Wiley Inter-Science, New York **2001**.
- [26] T. P. Beebe, J. T. Yates, An in Situ Infrared Spectroscopic Investigation of the role of Ethylidyne in the Ethylene Hydrogenation Reaction on Pd/Al₂O₃, *J. Am. Chem. Soc.* **1986**, 108, 663–671.

- [27] P. S. Cremer, G. A. Somorjai, Surface Science and Catalysis of Ethylene Hydrogenation, *J. Chem. Soc. Faraday Trans.* **1995**, 91, 3671–3677.
- [28] E. W. Hansen, M. Neurock, First-Principles-Based Monte Carlo Simulation of Ethylene Hydrogenation Kinetics on Pd, *Journal of Catalysis* **2000**, 196, 241–252.
- [29] A. Anderson, S. Choe, Ethylene Hydrogenation Mechanism on the Pt (111) Surface., *J. Phys. Chem.* **1989**, 93, 6145–6149.
- [30] R. Cortright, S. Goddard, Kinetic Study of Ethylene Hydrogenation, *J. Catal.* **1991**, 127, 342–353.
- [31] H. Ofner, F. Zaera, Isothermal Kinetic Measurements for the Hydrogenation of Ethylene on Pt(111) under Vacuum: Significance of Weakly-Bound Species in the reaction Mechanism, *J. Phys. Chem. B* **1997**, 101, 396–408.
- [32] F. Zaera, On the Mechanism for the Hydrogenation of Olefins on Translational-Metal Surfaces: The Chemistry of Ethylene on Pt(111), *Langmuir* **1996**, 12, 88.
- [33] J. E. Rekoske, R. D. C. and, Microkinetic Analysis of Diverse Experimental Data for Ethylene Hydrogenation on Platinum, *Journal of Physical Chemistry* **1992**, 96.
- [34] F. Zaera, G. A. Somorjai, Hydrogenation of Ethylene over Pt(111) Single-Crystal Surfaces, *J. Am. Chem. Soc.* **1984**, 106, 2288–2293.
- [35] S. B. Mohsin, M. Trenary, H. J. Robota, Infrared Identification of the Low-Temperature forms of Ethylene Adsorbed on Pt/ Al_2O_3 , *J. Phys. Chem.* **1988**, 92, 5229–5233.
- [36] U. Heese, *Experimentelle Untersuchung des Umsatzverhaltens der Ethylenhydrierung an einem gepulverten Platin-Traegerkatalysator*, Diplomarbeit, Wesfaelische Wilhelms-Universitaet Muenster **1981**.
- [37] U. Heese, *Zur Bedeutung von Adsorbatstrukturen bei der Ethylen-Hydrierung an Platin-Tragerkatalysatoren*, Dissertation, Wesfaelische Wilhelms-Universitaet Muenster **1985**.
- [38] A. Farkas, L. Farkas, The Catalytic Interaction of Ethylene and Heavy Hydrogen on Platinum, *J. Am. Chem. Soc.* **1938**, 60, 22–28.
- [39] R. D. Cortright, S. A. Goddard, J. E. Rekoske, J. A. Dumesic, Kinetic

- Study of Ethylene Hydrogenation, *Journal of Catalysis* **1991**, 127, 342–353.
- [40] H. Molero, D. Stacchiola, W. T. Tysoe, The Kinetics of Ethylene Hydrogenation Catalyzed by Metallic Palladium, *Catalysis Letters* **2005**, 101, 145–149.
- [41] A. N. R. Bos, E. S. Bootsma, F. Foeth, H. W. J. Sleyster, K. R. Westerterp, A Kinetic Study of the Hydrogenation of Ethyne and Ethene on a commercial Pd/ Al_2O_3 Catalyst, *Chemical Engineering and Processing* **1993**, 32, 53–63.
- [42] D. Duca, G. Barone, Z. Varga, Hydrogenation of Acetylene-Ethylene Mixtures on Pd Catalysts: Computational Study on the Surface Mechanism and on the Influence of the Carbonaceous Deposits, *Catalysis Letters* **2001**, 72.
- [43] Y. Takasu, T. Sauma, Hydrogenation of Ethylene on small Palladium Particles, *Chem. Lett.* **1985**, 48, 1179.
- [44] T. Sekitani, T. Takaoka, Interaction of Ethylene with H-Preadsorbed Pd(110) Surface: Hydrogenation and H-D Exchange Reactions, *J. Phys. Chem.* **1992**, 96, 8462–8468.
- [45] A. V. Zeigarnik, R. E. Valdes-Perez, O. N. Temkin, Metal-Catalyzed Ethylene Hydrogenation: The Method of Interactive Search for Multiple Working Hypotheses, *Langmuir* **1998**, 14, 4510–4516.
- [46] M. Neurock, R. A. van Santen, A First Principle Analysis of C-H Bond Formation in Ethylene Hydrogenation, *J. Phys. Chem. B* **2000**, 104, 11127–11145.
- [47] A. Borodzinski, The Effect of Palladium Particle Size on the Kinetics of Hydrogenation of Acetylene-Ethylene Mixtures over Pd/ SiO_2 Catalysts, *Catalysis Letters* **2001**, 71, 169–175.
- [48] N. Mostoufi, A. Ghoorchian, R. Sotudeh-Gharebagh, Hydrogenation of Acetylene: Kinetic Studies and Reactor Modeling, in *International Journal of Chemical Reactor Engineering*, Article A14, vol. 3, Berkeley Electronic Press **2005**.
- [49] E. W. Hansen, M. Neurock, Modeling surface kinetics with first-principles-based molecular simulation, *Chemical Engineering Science*

- 1999**, 54, 3411–3421.
- [50] D. H. Mei, E. W. Hansen, M. Neurock, Ethylene Hydrogenation over bimetallic Pd/Au(111) Surfaces: Application of Quantum Chemical Results and Dynamic Monte Carlo Simulation, *Journal of Physical Chemistry B* **2003**, 107, 798–810.
- [51] A. N. R. Bos, K. R. Westerterp, Mechanism and Kinetics of the selective Hydrogenation of Ethyne and Ethene, *Chemical Engineering and Processing* **1993**, 32, 1–7.
- [52] H. Zea, K. Lester, A. K. Datye, E. Rightor, R. Gulotty, W. Waterman, M. Smith, The Influence of Pd-Ag Catalyst Restructuring on the Activation Energy for Ethylene Hydrogenation in Ethylene-Acetylene Mixtures, *Applied Catalysis A* **2005**, 282, 237–245.
- [53] J. Horiuti, M. Polanyi, Exchange Reactions of Hydrogen on Metallic Catalysts, *J. Chem. Soc. Faraday Trans.* **1934**, 30, 1164–1172.
- [54] R. L. Augustine, F. Yaghmaie, J. F. V. Peppen, Heterogeneous Catalysis in Organic Chemistry 2. A Mechanistic Comparison of Noble-Metal Catalysts in Olefin Hydrogenation., *J. Org. Chem.* **1984**, 49, 1865–1870.
- [55] C. N. Satterfield, *Heterogeneous Catalysis in Practice*, McGraw Hill, New York **1980**.
- [56] J. T. Richardson, *Principles of Catalyst Development*, Plenum Press, New York **1989**.
- [57] AutoclaveEngineers, *Catalytic Reactor Selection Guide*, bulletin CR-SR, Autoclave Engineers, 2930 West 22nd Street Erie, Pennsylvania 16506-2302 USA Ph: 814-838-5700 Fax: 814-838-5855, www.autoclaveengineers.com, 06-0047pe-0102 ed.
- [58] L. Forni, Laboratory Reactors, *Catalysis* **1997**, 34, 353–367.
- [59] R. Adler, F. Schroeder, B. Platzer, DE 101 04 849 A 1 **2001**.
- [60] B. Hesselbarth, *Studien zum realen Verhalten von Differenzialkreislaufreaktoren für reaktionskinetische Untersuchungen heterogen-gaskatalytischer Reaktionen an körnigen Partikeln*, Habilitationsschrift, Martin-Luther-Universitaet Halle-Wittenberg **2005**.
- [61] V. A. Roiter, G. P. Korneichuk, M. G. Leperson, N. A. Stukanowskaia,

- B. I. Tolchina, *Zh. Fiz. Khim.* **1950**, 24, 459.
- [62] J. R. Balder, E. E. Petersen, Application of the single pellet reactor for direct mass transfer studies, *J. Catalysis* **1968**, 11, 202–210.
- [63] L. L. Hegedus, E. E. Petersen, *Ind. Eng. Chem. Funda.* **1972**, 11, 579.
- [64] L. L. Hegedus, E. E. Petersen, The Single Pellet Diffusion Reactor: Theory and Applications, *Cat. Rev. - Sci. Eng.* **1974**, 9, 245–266.
- [65] T. Dogu, A. Keskin, G. Dogu, J. M. Smith, Single-Pellet, Moment Method for Analysis of Gas-Solid Reactions, *AIChE Journal* **1986**, 33, 743–750.
- [66] S. S. Au, J. Dranoff, J. B. Butt, Nonuniform activity distribution in catalyst particles: benzene hydrogenation on supported nickel in a single pellet diffusion reactor, *Chemical Engineering Science* **1995**, 50, 3801–3812.
- [67] C. Cabbar, G. Dogu, T. Dogu, B. J. McCoy, Single-Pellet Dynamics for the Soil Organic Matter Effect on Dichloromethane Sorption, *AIChE Journal* **1996**, 42, 2090–2093.
- [68] T. Dogu, N. Yasyerli, G. Dogu, B. J. McCoy, J. M. Smith, One-Sided Single-Pellet Technique for Adsorption and Intraparticle Diffusion, *AIChE Journal* **1996**, 42, 516–523.
- [69] L. C. Nett-Carrington, R. K. Herz, Spatiotemporal patterns within a porous catalyst: dynamic carbon monoxide oxidation in a single-pellet reactor, *Chemical Engineering Science* **2002**, 57, 1459–1474.
- [70] C. Rieckmann, *Lösung des Problems der Diffusion und Reaktion in dreidimensionalen Porenetzwerken für allgemeine Kinetiken*, PhD Thesis, Technische Universität Hamburg-Harburg **1997**.
- [71] S. Chilamkurthi, *Investigation of the effects of Catalyst Pore Structure on Simultaneous Diffusion and Reaction*, Master Thesis, Department of Chemical Reaction Engineering, Technische Universität Hamburg Harburg (TUHH) **2005**.
- [72] O. Bonaventure, *Experimental Study of Multicomponent Diffusion and Reaction in Porous Catalysts: The Effect of Pore Structure*, Master Thesis, Department of Chemical Reaction Engineering, Technische Universität Hamburg Harburg (TUHH) **2006**.

- [73] V. Omaynikova, *Experimentelle Untersuchung des Effekts der Porenstruktur von katalytischen Pellets auf die Reaktion und Mehrkomponentendiffusion in einem Einzelpellet-Diffusions-Reaktor*, Bachelorarbeit, Institut für Chemische Reaktionstechnik, Technische Universität Hamburg Harburg (TUHH) **2007**.
- [74] N. G. Marinova, *Influence of the catalyst support and pore structure on diffusion phenomena under reactive conditions: An experiental study in a single-pellet reactor*, Master Thesis, Institut für Chemische Reaktionstechnik, Technische Universität Hamburg Harburg (TUHH) **2008**.
- [75] C. Bojkova, *Einfluss der Porenstruktur der katalytischen Pellets auf die Reaktion in einem Einzelpellet-Diffusions-Reaktor*, Bachelorarbeit, Institut für Chemische Reaktionstechnik, Technische Universität Hamburg Harburg (TUHH) **2007**.
- [76] J. M. Berty, *Experiments in Catalytic Reaction Engineering*, Elsevier, Amsterdam **1999**.
- [77] H. Lynggaard, A. Andreasen, C. Stegelmann, P. Stoltze, Analysis of simple kinetic models in heterogeneous catalysis., *Progress in Surface Science* **2004**, 77, 71–137.
- [78] Z. Jovanov, *Untersuchung der optimalen Reaktionsbedingungen in einem kinetischen Turbo-Reaktor*, Bachelorarbeit, Technische Universität Hamburg-Harburg **2008**.
- [79] K. A. Günbulut, *Analysis of Reactive Flow Through a Catalyst Pellet Using Dusty-Gas Model*, Masters Thesis, Hamburg University of Technology **2005**.
- [80] J. Choi, D. D. Do, H. D. Do, Surface Diffusion of Adsorbed Molecules in Porous Media: Monolayer, Multilayer and Capillary Condensation Regimes, *Ind. Eng. Chem. Res.* **2001**, 40, 4005–4031.
- [81] S. P. Rigby, A Model for the Surface Diffusion of Molecules on a Heterogeneous Surface, *Langmuir* **2003**, 19, 364–376.
- [82] L. K. Doraiswamy, M. M. Sharma, *Heterogeneous reactions: Analysis, Examples, and Reactor Design. Volumen 1: Gas-Solid and Solid-Solid Reactions*, John Wiley and Sons, New York **1984**.

- [83] J. Kärger, D. M. Ruthven, *Diffusion in Zeolites and other Microporous Solids*, John Wiley & Sons **1992**.
- [84] A. Kapoor, R. T. Yang, C. Wong, Surface Diffusion, *Catal.Rev.-Sci.Eng.* **1989**, 31, 129–214.
- [85] R. Jackson, *Transport in Catalysis*, Elsevier Scientific Publication Company **1977**.
- [86] J. P. B. Mota, Adsorption and transport in nanoporous materials, in *Nanoporous Materials. Science and Engineering*.
- [87] C. N. Satterfield, *Mass Transfer in Heterogeneous Catalysis*, Robert E. Krieger Publishing **1981**.
- [88] J. M. Zalc, S. C. Reyes, E. Iglesia, Monte-Carlo simulation of surface and gas phase diffusion in complex porous structures, *Chemical Engineering Science* **2003**, 58, 4605–4617.
- [89] D. Luss, Diffusion-Reaction Interactions in Catalyst Pellets, in *Chemical Reaction and Reactor Engineering*, J. J. Carberry, ed., Dekker **1987**, p. 248.
- [90] S. C. Reyes, J. H. Sinfelt, G. J. DeMartin, Diffusion in Porous Solids: The Parallel Contribution of Gas and Surface Diffusion Processes in Pores Extending from the Mesoporous Region into the Microporous Region, *Journal of Physical Chemistry B* **2000**, 104, 5750–5761.
- [91] A. Argonul, L. Argonul, F. J. Keil, The Inconsistency in Modeling Surface Diffusion with Adsorption Equilibrium, *Journal of the University of Chemical Technology and Metallurgy* **2007**, 42, 181–186.
- [92] C. O. Bennett, J. E. Myers, *Momentum, Heat, and Mass Transfer*, McGraw-Hill, third ed. **1982**.
- [93] G. Dogu, Diffusion Limitations for Reactions in Porous Catalysis, in *Mass Transfer and Reactor Design*, N. P. Cheremisinoff, ed., *Handbook of Heat and Mass Transfer*, vol. 2, Gulf Publishing company **1986**, pp. 437–484.
- [94] A. Chambers, *Modern Vacuum Physics*, Chapman & Hall/CRC **2005**.
- [95] J. F. O’Hanlon, *A User’s Guide to Vacuum Technology*, John Wiley & Sons, third ed. **2003**.
- [96] R. G. Livesey, Flow of Gases through Tubes and Orifices, in *Foun-*

- dations of Vacuum Science and Technology*, J. M. Lafferty, ed., John Wiley & Sons **1998**, pp. 81–140.
- [97] W. Steckelmacher, Knudsen flow 75 years on: the current state of the art for flow of rarefied gases in tubes and systems, *Rep. Prog. Phys.* **1986**, 49, 1083–1107.
- [98] G. R. Youngquist, Diffusion and Flow of Gases in Porous Solids, *Industrial and Engineering Chemistry* **1970**, 62(8) August, 52–63.
- [99] F. Sharipov, V. Seleznev, Data on Internal Rarefied Gas Flows, *J. Phys. Chem. Ref. Data* **1998**, 27(3), 657–705.
- [100] W. Steckelmacher, H. Henning, Comments on 'The approximate calculation of transmission probabilities for the conductance of tubulations in the molecular flow regime, *Vacuum* **1979**, 29, 31.
- [101] P. Clausing, The Flow of Highly Rarefied Gases through Tubes of Arbitrary Length, *The Journal of Vacuum Science and Technology* **1971**, 8(5) November, 636–646.
- [102] R. Datta, R. G. Rinker, The Flow of Rarefied Gases Through Long Tubes of Circular Cross-Section, *The Canadian Journal of Chemical Engineering* **1981**, 59, 268–278.
- [103] P. Szwemin, M. Niewinski, Comparison of Transmission Probabilities Calculated by Monte Carlo Simulation Techniques and Analytical Methods, *Vacuum* **2002**, 67, 359–362.
- [104] J. Gomez-Goni, P. J. Lobo, Comparison between Monte Carlo and Analytical Calculation of the Conductance of Cylindrical and Conical Tubes, *J. Vac. Sci. Technol. A* **2003**, 21(4) Jul/Aug, 1452–1457.
- [105] G. Saksaganskii, *Molecular Flow in Complex Vacuum Systems*, Billing & Sons Ltd., translated by: V.A. Pleshakov **1988**.
- [106] W. Steckelmacher, The Effect of Cross-Sectional Shape on the Molecular Flow in Long Tubes, *Vacuum* **1978**, 28(6/7), 269–275.
- [107] B. B. Dayton, Gas Flow Patterns at Entrance and Exit of Cylindrical Tubes, in *National Symposium on Vacuum Technology Transactions*, S. Edmund, J. H. P. Durant, eds. **1956**.
- [108] J. Greenwood, The correct and incorrect generation of a cosine law distribution of scattered particles for Monte-Carlo modeling of vacuum

- systems, *Vacuum* **2002**, 67, 217–222.
- [109] M. Knudsen, *Kinetic Theory of Gases*, Methuen & Co. Ltd., John Wiley and Sons. Inc. **1952**.
- [110] M. Knudsen, *The cosine law in the kinetic theory of gases*, NASA technical translation F-486, Washington DC, translation of "das cosinusgesetz in der kinetischen gastheorie. (1915). annalen der physik, 48, 1113-1121" ed. **1967**.
- [111] H. Golub, C. V. Loan, *Matrix Computations*, The Johns Hopkins University Press, Baltimore, second ed. **1989**.
- [112] A. Argönül, F. J. Keil, An alternative procedure for modelling of Knudsen flow and surface diffusion, *Periodica Polytechnica Chemical Engineering* **2008**, 52, 37–55.
- [113] C. Davies, C. Lucas, The failure of theory to predict the density distribution of gas flowing through a tube under free molecular conditions., *Journal of Physics D: Applied Physics* **1983**, 16, 1–16.
- [114] Y. D. Chen, R. T. Yang, Surface and mesoporous diffusion with multilayer adsorption, *Carbon* **1998**, 36, 1525–1537.
- [115] E. R. Gilliland, R. F. Baddour, J. L. Russell, Rates of Flow Through Microporous Solids, *AIChE Journal* **1958**, 4, 90–96.
- [116] B. Poling, J. Prausnitz, J. O'Connell, *The Properties of Gases and Liquids*, Mc-Graw Hill, fifth ed. **2001**.

CURRICULUM VITAE

AYKUT ARGÖNÜL

BORN IN ANKARA/TURKEY, 09.05.1978

E-MAIL: ARGONULAYKUT@GMAIL.COM

Education

Dec. '02 – Oct. '08	Hamburg University of Technology (TUHH) <i>Inst. of Chemical Reaction Engineering (Ph.D.) "Measurement and Calculation of Multicomponent-Diffusion and Reaction in Catalyst Particles, Effect of the Catalyst Pore Structure"</i>	Hamburg/Germany
Oct. '00 – Nov. '02	Hamburg University of Technology (TUHH) <i>Process Engineering (Master of Science)</i>	Hamburg/Germany
Sep. '96 – Jun. '00	Bosphorus University (Boğaziçi Üniversitesi) <i>Chemical Engineering (Bachelor of Science)</i>	Istanbul/Turkey
Sep. '89 – Jun. '96	Kadıköy Anatolian High School (KAL)	Istanbul/Turkey

Publications

A. Argonul, L. Argonul, F. J. Keil, The inconsistency in modeling surface diffusion with adsorption equilibrium, *Journal of the University of Chemical Technology and Metallurgy* 2007, 42, 181–186.

A. Argonul, F. J. Keil, An alternative procedure for modeling of Knudsen flow and surface diffusion, *Periodica Polytechnica Chemical Engineering* 2008, 52, 37–55.

Academic Awards and Achievements

A scholarship awarded by Graduiertenkolleg (for conservation principles in the modeling and simulation of marine, atmospheric and technical systems), which is sponsored by Deutsche Forschungsgemeinschaft (German Research Foundation), for the first three years of the Ph.D. study.

Graduated from the Hamburg University of Technology process engineering master's program with an overall grade of "very good".

A joint scholarship awarded by DAAD (Deutscher Akademischer Austauschdienst) and TEV (Turkish Education Foundation) for the entire master education period.

Graduated at 2nd place (with Honors Certificate) from the Chemical Engineering Department-Bosphorus University.

A "Scholarship of Achievement" throughout the bachelor studies awarded by the Bosphorus University, for continuous successful academic performance.

